CO-CURED MANUFACTURING OF ADVANCED COMPOSITE MATERIALS USING VACUUM ASSISTED RESIN TRANSFER MOLDING

A THESIS SUBMITTED TO
THE GRADUATE SCHOOL OF NATURAL AND APPLIED SCIENCES
OF
MIDDLE EAST TECHNICAL UNIVERSITY

BY

MERT AKIN

IN PARTIAL FULFILLMENT OF THE REQUIREMENTS
FOR
THE DEGREE OF MASTER OF SCIENCE
IN
MECHANICAL ENGINEERING

MAY 2018

Approval of the thesis:

CO-CURED MANUFACTURING OF ADVANCED COMPOSITE MATERIALS USING VACUUM ASSISTED RESIN TRANSFER MOLDING

submitted by **MERT AKIN** in partial fulfillment of the requirements for the degree of **Master of Science in Mechanical Engineering Department, Middle East Technical University** by,

Prof. Dr. Halil Kalıpçılar _____
Dean, Graduate School of **Natural and Applied Sciences**

Prof. Dr. M. A. Sahir Arıkan _____
Head of Department, **Mechanical Engineering**

Assoc. Prof. Dr. Almıla Güvenç Yazıcıoğlu _____
Supervisor, **Mechanical Engineering Dept., METU**

Examining Committee Members:

Prof. Dr. Fevzi Suat Kadıoğlu _____
Mechanical Eng. Dept., METU

Assoc. Prof. Dr. Almıla Güvenç Yazıcıoğlu _____
Mechanical Eng. Dept., METU

Assoc. Prof. Dr. Merve Erdal _____
Mechanical Eng. Dept., METU

Prof. Dr. Altan Kayran _____
Aerospace Eng. Dept., METU

Prof. Dr. Can Çoğun _____
Mechatronics Eng. Dept., Çankaya Uni.

Date: 10.05.2018

I hereby declare that all information in this document has been obtained and presented in accordance with academic rules and ethical conduct. I also declare that, as required by these rules and conduct, I have fully cited and referenced all material and results that are not original to this work.

Name, Last Name: MERT AKIN

Signature:

ABSTRACT

CO-CURED MANUFACTURING OF ADVANCED COMPOSITE MATERIALS USING VACUUM ASSISTED RESIN TRANSFER MOLDING

Akın, Mert

M.S., Department of Mechanical Engineering

Supervisor: Assoc. Prof. Dr. Almıla Güvenç Yazıcıoğlu

May 2018, 191 pages

Sub-structures of aircraft structures mainly consist of stiffened shells such as fuselage frames, ribs, and multi-cell box beams. Conventionally, these stiffened shells are manufactured through a process wherein shells and stiffeners are fabricated separately and then are integrated either through mechanical fastening or adhesive bonding. Co-curing is an integral molding technique that can greatly reduce the part count and the final assembly costs for composite materials. In this study, a low-cost co-curing manufacturing technique for stiffened shells of aircraft structures, particularly multi-cell box beams, is developed. Foam material, foam strength, curing operation and foam coating are considered to be the process parameters and the process is improved by optimizing these parameters. The study also has a wider goal of aiding the simulation tools of composite material processing by providing a material data, including preform permeability, porosity, and resin viscosity model. For this purpose, the three-fold approach is followed. First, an extensive characterization of the preform and the resin properties is performed.

Then, resin impregnation simulations of the co-cured three-cell box beam are performed. In the final part, the co-curing manufacturing technique is developed and the co-curing process is compared with the conventional method, secondary bonding, from part bending strength, manufacturing and energy consumption perspectives. The four-point bending test results show that the co-cured part withstands 95% higher load and fails at 99% higher load compared to the secondary-bonded part. Additionally, it is found that almost 57% energy and 25% labor time savings can be achieved by using the co-curing technique.

Keywords: Co-curing, Vacuum Assisted Resin Transfer Molding (VARTM), Resin Flow, Analytical Modeling, Numerical Analysis

ÖZ

İLERİ KOMPOZİT MALZEMELERİN VAKUM DESTEKLİ REÇİNE KALIPLAMA KULLANILARAK EŞ ZAMANLI KÜRLENDİRME YÖNTEMİYLE ÜRETİMİ

Akın, Mert
Yüksek Lisans, Makina Mühendisliği Bölümü
Tez Yöneticisi: Doç. Dr. Almıla Güvenç Yazıcıoğlu

Mayıs 2018, 191 sayfa

Ana uçak yapıları çoğunlukla uçak gövdesi kaburgaları, ribler ve kutu kirişler gibi güçlendirilmiş kabuk yapılarından meydana gelmektedir. Geleneksel olarak bu güçlendirilmiş kabuk yapılar, kabuğun ve destek plakasının ayrı ayrı üretilip sonrasında mekanik bağlantı veya yapıştırıcı kullanılarak birleştirilmesi yöntemiyle üretilmektedir. Eş zamanlı kürlendirme yöntemi kompozit malzemelerde kullanılacak parça sayısının ve final montaj maliyetlerinin büyük oranda azaltılmasını sağlayan bütünleşik bir kalıplama tekniğidir. Bu çalışmada, özellikle çok gözlü kutu profiller gibi güçlendirilmiş kabuk yapıları için düşük maliyetli bir eş zamanlı kürlendirme yöntemi geliştirilmektedir. Köpük malzemesi, köpük dayanımı, kürlendirme ve köpük kaplama operasyonları proses parametreleri olarak belirlenmiş ve bu parametreler eniyileyerek proses geliştirilmiştir. Bu çalışma aynı zamanda simülasyon programlarına destek olması amacıyla preform geçirgenlik ve boşluk değerlerini ve reçine viskozite modellerini sağlayarak daha geniş bir hedefe sahip olmaktadır. Bu amaçla çalışma, üç bölümde oluşmaktadır.

İlk olarak, preform ve reçine malzemelerinin karakterizasyonu kapsamlı bir şekilde gerçekleştirilmiştir. Sonrasında, eş zamanlı kürlendirilmiş üç gözlü kutu profilin reçine akış simülasyonları gerçekleştirilmiştir. Son bölümde, yöntem geliştirilmiş ve eş zamanlı kürlendirme yöntemi ve geleneksel teknik kullanılarak üç gözlü kutu profiller üretilmiştir. Eş zamanlı kürlendirme yöntemi parça eğme dayanımı, üretim ve enerji tüketimleri açısından geleneksel teknik ile karşılaştırılmıştır. Dört nokta eğme sonuçları, eş zamanlı kürlendime ile üretilen parçanın %95 daha fazla yüke dayanabildiği ve %99 daha fazla yük altında kırıldığını göstermektedir. İlaveten, eş zamanlı kürlendirme yöntemi kullanılarak %57 enerji ve %25 işçilik zamanı tasarrufu elde edilebilmektedir.

Anahtar Kelimeler: Eş zamanlı kürlendirme, Vakum Destekli Reçine Transfer Kalıplama, Reçine Akışı, Analitik Modelleme, Numerik Analiz

To my family

ACKNOWLEDGEMENTS

Many people and institutions made contributions to this thesis study and I owe thanks to all. Firstly, I am heartily thankful to my supervisor Assoc. Prof. Dr. Merve Erdal for her guidance and support throughout of my graduate education.

Besides my supervisor, I would like to offer my special thanks to Assoc. Prof. Dr. Almıla Güvenç Yazıcıoğlu for her guidance and encouragement during my thesis study. I would like to express my sincere gratitude to Prof. Dr. Altan Kayran for his meaningful support on this study. I also want to thank the rest of my thesis committee: Prof. Dr. Can Çoğun and Prof. Dr. Fevzi Suat Kadıoğlu for their insightful and encouragement comments.

I would like to thank İZOREEL Composites for its assistance and help in the experimental study. Also, I wish to thank Prof. Dr. Metin Tanoğlu for his support in the mechanical tests.

Finally, I owe my deepest gratitude to my loving and supportive family: my grand mom Ayşe DEĞİRMENCİ, my mom Rukiye AKIN, my father Rahmi AKIN and my sister Beril AKIN.

TABLE OF CONTENTS

LIST OF TABLES

TABLES

LIST OF FIGURES

FIGURES

NOMENCLATURE

SYMBOLS		NAME	UNIT
LETTERS			
123	:	Principal Coordinate System	–
A_f	:	Sample area	m^2
B	:	Stiffening Index	–
B_μ	:	Exponent of time-dependent viscosity	–
C	:	Process Term in Permeability Term	s
C_2	:	Constant in Gebart Permeability Model	m^2
c_0	:	Castro-Macosko Model Parameter	–
c_1	:	Castro-Macosko Model Parameter	–
d_0	:	Lee & Han Model Parameter	–
d_1	:	Lee & Han Model Parameter	–
E_0	:	Arrhenius Model Emprical Constant	K
E_1	:	Arrhenius Model Emprical Constant	K
E_2	:	Arrhenius Model Emprical Constant	K
F_I	:	Material Term in Permeability Test	m^2/s
g	:	Gravity Vector	m^2/s
h	:	Laminate Thickness	m

$\bar{h}$	:	Average convection coefficient of a surface	W/m^2K
I	:	Guess value of $\frac{\partial P^*}{\partial x^*}$	Pa
K	:	Scalar Permeability	m^2
k_0	:	Constant in Carman-Kozeny Permeability Model	m^2
k'	:	Constant in Gutowski Permeability Model	m^2
k_{10}	:	Rate constant for non-catalysed reaction	$1/min$
k_{20}	:	Rate constant for auto-catalysed reaction	$1/min$
L	:	Characteristic Length	m
m_{kamal}	:	Kamal-Sourour Model Coefficient	$-$
N_I	:	Nominator of Materiam Term F_I in Permeability Test	m^2
N_{nodes}	:	Number of Nodes	$-$
N_{test}	:	Four-point Bending Test Speed	mm/min
$\overline{N_{u_L}}$	:	Nusselt Number for a surface of length L	$-$
n	:	Number of Layers	$-$
n_{kamal}	:	Kamal-Sourour Model Coefficient	$-$
P	:	Resin Pressure	Pa
P_{comp}	:	Preform Compaction Pressure	Pa
P_{atm}	:	Atmospheric Pressure	Pa
P_r	:	Prandtl Number	$-$
R	:	Ideal Gas Constant	$J/K.mol$
R^2	:	Curve Fit Parameter	$-$

R_a	:	Rayleigh Number	$-$
S	:	Surface	m^2
T	:	Temperature	$^{\circ}C$
T_g	:	Glass transition temperature	$^{\circ}C$
t_f	:	Instant Time of Flow Front	s
u	:	Superficial Velocity	m/s
u_f, v_f, w_f	:	Resin Velocity at Flow Front	m/s
v	:	Macroscopic Velocity	m/s
W_{sample}	:	Sample Weight	kg
W_{fabric}	:	Areal density of fabric	kg/m^2
x, y, z	:	Rectangular Coordinates in the xyz Coordinate System	m
x_f, y_f, z_f	:	Position of Flow Front	m

GREEK

Δp	:	Pressure difference	Pa
α	:	Degree of cure or Degree of Conversion	$-$
α_{gel}	:	Critical conversion at gelation	$-$
β	:	Volumetric Thermal Expansion	1/K
Γ^e	:	Boundary of the element	$-$
$\dot{\gamma}$	:	Shear rate	$1/s$
ε	:	Strain Rate	$-$
η	:	Dynamic Viscosity	$Pa.s$
κ	:	Thermal Diffusivity	m^2/s
λ	:	Thermal Conductivity	W/mK
μ	:	Viscosity	$Pa.s$
μ_0	:	Coefficient of time-dependent viscosity	$Pa.s$
$\nabla.$	:	Divergence Operator	$-$
ρ_{sup}	:	Superficial Density of Preform	kg/m^3
ρ_f	:	Density of Fiber	kg/m^3
ρ_{fabric}	:	Density of Fabric	kg/m^3
τ	:	Shear stress	Pa
v_f	:	Fiber Volume Fraction	$-$
v_{fo}	:	Fiber Volume Fraction at a $P_{comp} = 1\ Pa\ (-)$	$-$
v_{fa}	:	Theoretical Maximum Fiber Volume Fraction	$-$

$\emptyset$	:	Porosity	$-$
$\forall$	:	Volume	m^3
Ω^e	:	Element Domain	$-$

ACRYONMS

BC	:	Boundary Conditions
CIRTM	:	Co-injection Resin Transfer Molding
CTE	:	Coefficient of Thermal Expansion
CV	:	Control Volume
DP-RTM	:	Differential Pressure Resin Transfer Molding
EPS	:	Expanded Polystyrene
FEM	:	Finite Element Method
LCM	:	Liquid Composite Molding
NINR	:	Non-isothermal non-reactive
NIR	:	Non-isothermal reactive
ODE	:	Ordinary Differential Equation
OoA	:	Out of Autoclave
PDE	:	Partial Differential Equation
PS	:	Polystreyene
RFI	:	Resin Film Infusion
RTM	:	Resin Transfer Molding
SLI	:	Sinlge Line Injection
VARTM	:	Vacuum Assisted Resin Transfer Molding
VBO	:	Vacuum Bag Only
VERITY	:	Vacuum Enhanced Resin Infusion Technology

XPS : Extruded Polystyrene

2-D : Two Dimensional

3-D : Three Dimensional

CHAPTER 1

INTRODUCTION

1.1. COMPOSITE MATERIALS

Composite materials are materials that are comprised of two or more materials on a macroscopic scale to form a useful third material. The macroscopic examination is the key in the definition so that different materials can be combined on a microscopic scale, such as metal alloys, but the resulting composite material becomes macroscopically homogeneous. By definition, composite materials are formed for this purpose, meaning if they are well designed, they typically show better qualities than their components. Some of these characteristics are high strength, stiffness, good corrosion resistance, wear resistance, fatigue life, thermal insulation, thermal conductivity, temperature-dependent behavior and low weight.

Even though they seem to be modern, composites have been used since antiquity. For instance, plywood once was used by ancient Egyptians to achieve superior strength and thermal resistance. Straw and cob are other examples that were very common in the past [1].

Currently, the term “advanced composite materials” refers to composites that have high strength reinforcement material and weaker, but tough matrix material, which binds the reinforcement and gives the material shape.

Advanced composites show desirable physical and chemical properties along with high stiffness and strength so that they replace a metal component in many applications, including space, aerospace and military applications. The “advanced composite materials” is also known for its use of expensive reinforcement and resin systems, however, there has been a tendency to reduce the production expenses in the last decade. The motivation of this study is to propose a low-cost technique to produce advanced composites.

1.1.1. Reinforcements

The prime role of the fibers is to provide strength and stiffness in the composite structure. In advanced composites, fibers occupy the largest volume of fraction and typically 70-90% of load is carried by fibers. Nevertheless, fibers particularly in the class of high strength, are inherently brittle and exhibit linear stress-strain characteristic with little or no evidence of yielding. Table 1 shows a summary of the properties of the major fiber reinforcements. Additionally, fibers provide the thermal and electrical characteristic of composites. For example, in the case of electrical conductivity, carbon fiber can be preferable, whereas, for the insulation purpose, E-Glass can be used.

Glass fibers are the most common reinforcement owing to their moderate mechanical properties and low cost. Among fiber glasses, such as E-Glass, S-Glass, and R-Glass, E-Glass is extensively used in commercial products. E-Glass, also known as electrical glass, is a good combination of low cost, moderate strength, and stiffness along with good corrosion resistance. S-Glass, on the other hand, is a high strength glass fiber that was developed for structural applications, including pressure vessels and solid motor casings.

Aramid fiber is the low density and highly tough organic fiber. Even though it shows excellent tensile strength, its compressive strength is very poor. Aramid fiber absorbs moisture and moreover is susceptible to ultraviolet light.

Carbon fibers have an excellent combination of mechanical properties with their high strength and low density. It also has outstanding fatigue behavior, which makes it highly preferable for structural applications. One of the significant characteristics of carbon fiber is its electrical conductivity. If in contacts with active metals, such as aluminum, it causes galvanic corrosion. Additionally, carbon fibers have a low coefficient of thermal expansion (CTE).

Table 1. Properties of Commonly Used Reinforcements [2]

Fiber	Manufacturer	Density (g/cm^3)	Tensile Strength (MPa)	Elastic Modulus (GPa)
E-Glass	Corning	2.54	3450	72.5
S-Glass	Corning	2.49	4480	85.6
Carbon – AS4	Hercules	1.81	3730	235
Carbon – T300	Union Carbide	1.76	2760-3450	228
Carbon – IM-7	Hercules	1.80	5170	290
Kevlar(Aramid)	DuPont	1.45	3800	131

1.1.2. Matrix Materials

The roles of a matrix in fiber-reinforced composites are to bind the fiber together, share the load between fibers, provide a good surface finish and protect the surface to protect fibers from chemical and mechanical attacks.

Three types of matrix materials are available: (1) polymeric matrix, (2) metallic matrix and (3) mineral matrix.

Polymeric matrices are either thermoplastic resins or thermoset resins. Typical thermoset resins in composites are commonly polyester, phenolic, silicone, and epoxy. Common thermoplastic resins are polypropylene, polyphenylene sulfone, polyamide, polyether ether ketone. Table 2 presents the major properties of common resins.

Table 2. Properties of Commonly Used Resins [3]

Resins	Density (g/cm^3)	Tensile Strength (MPa)	Elastic Modulus (GPa)	Coefficient of Thermal Expansion ($^{\circ}C^{-1}$)
Epoxy	1.2	130	4.5	$11x10^{-5}$
Phenolic	1.3	70	3	$1x10^{-5}$
Polyester	1.2	80	4	$8x10^{-5}$
Vinylester	1.15	75	3.3	$5x10^{-5}$
Polypropylene	0.9	30	1.2	$9x10^{-5}$
Polyamide	1.1	70	2	$8x10^{-5}$
Polyether ether ketone (PEEK)	1.3	90	4	$5x10^{-5}$

1.1.3. Fabrics

In polymer matrix composites, a fabric is defined as a manufactured assembly of long fibers of carbon, glass, aramid or a combination of these, to form one or more layers of fibers. Two mechanisms are used to hold layers together: (1) interlocking fibers mechanically (2) using a secondary material to bound fibers. There are two main types of fabrics: woven fabrics and nonwoven (noncrimp) fabrics.

1.1.3.1. Woven Fabrics

In woven fabrics, warp (0˚) and weft (90˚) interlace are interlaced in a regular pattern or weave style and the integrity of fabric is determined by the mechanical interlocking of fibers.

The weave style determines the ability of a fabric to conform a surface, also known as draping, surface smoothness, and stability of a fabric. For example, plain weave has a symmetry and exhibits good fabric stability, whereas satin weave has an excellent draping property. Figure 1 shows examples of different woven styles.

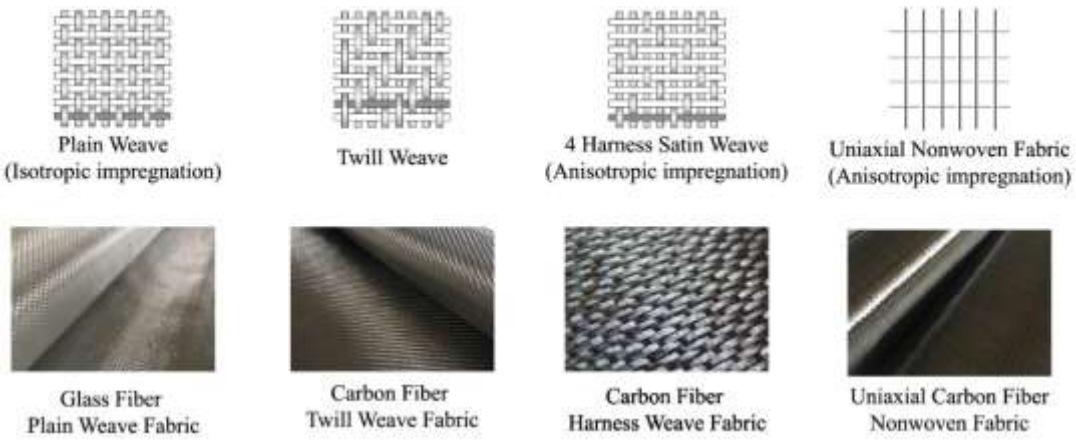

Figure 1. Examples of Woven and Nonwoven Fabrics

1.1.3.2. Nonwoven Fabrics

In nonwoven fabrics, also known as noncrimp fabrics, fiber yarns are placed parallel to each other and then stitched together using polyester thread. Noncrimp fabrics can be uniaxial, biaxial or multiaxial arrangements. Uniaxial carbon fiber nonwoven fabric is shown in Figure 1.

1.1.4. Preforms

Preforms are pre-shaped fabric reinforcements in the form of two- or three-dimensional fiber architecture. They are basically feedstock for liquid molding processes, particularly for resin transfer molding (RTM) and vacuum assisted resin transfer molding (VARTM), which use to produce complex shaped parts. The prime motivation of preforms is to cost down manufacturing expenses by reducing fabric preparation time. Preforms also provide a homogeneous distribution of matrix and reinforcement, which in turn improves the mechanical properties [4]. Preforms can be made by weaving, braiding, knitting shapes, stitching continuous fiber materials; or combination of these techniques.

1.1.5. Prepregs

Prepregs are continuous unidirectional fibers that are partially impregnated with the uncured resin. Prepregs can be of fabric, fiber or mat forms. Reinforcement in prepregs can be glass, carbon, or aramid, while resin system can be either thermoset or thermoplastic. Prepregs provide consistent mechanical properties and ease in manufacturing so that eliminates the need for resin mixing. But on the downside, prepregs are highly expensive compared to dry reinforcements and thermoset prepregs have limited shelf-life. Figure 2 presents the various types of prepregs.

1.1.6. Core Materials

Core materials are placed between the composite skins in order to improve the second moment of area thereby increasing the bending stiffness. There are common four types of core materials: (1) honeycomb cores (2) wood cores (3) syntactic cores (4) foam cores. Among core materials, foams are the most common and can be made from various polymers including polystyrene (PS), polyurethane, polyvinyl chloride, and polymethacrylimide.

Core materials are often preferred to manufacture sandwich structures, however, in this study, they are used as removable mandrels to produce hollow structures. Two typical soluble cores have been studied so far in the literature that are water-soluble cores and solvent-soluble foams. Water soluble-cores are originally used to produce high pressure die castings. Jiang et al. presented a water-soluble core comprised of polyvinyl glycol, mica powder, sodium chloride and polyethylene [5]. Xiao et al. developed a water-soluble core material using sodium chloride for manufacturing hollow composite parts [6].

Polystyrene (PS) foams are solvent-soluble and are either in open cell or closed cell forms. Typically, closed cell foams have lower permeability, higher strength, and better acoustic insulation properties. Two common types of polystyrene foams are available - Expanded Polystyrene (EPS) and Extruded Polystyrene (XPS). Expanded Polystyrene has high permeability, whereas Extruded Polystyrene has higher stiffness, better surface finish and is easy to solute.

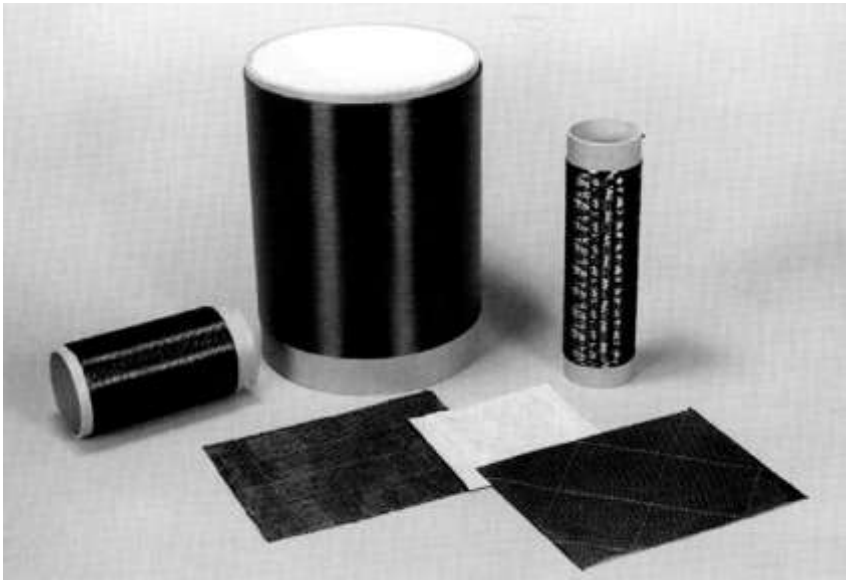

Figure 2. Examples of Prepregs [7]

1.2. MANUFACTURING OF ADVANCED COMPOSITES

Polymer Matrix Composite manufacturing techniques can be basically divided into two categories based on the matrix material: thermoset composites manufacturing and thermoplastic composites manufacturing. Thermoset composites, which constitute the 75% of the market, dominate the composite industry.

As thermoset composites are prevalent, their manufacturing processes are much more mature than that of thermoplastic composites. The first use of thermoset composites appears in the early 1940s, whilst the use of thermoplastic composites occurred much later [7].

Thermoset composites have a variety of manufacturing techniques, including resin transfer molding (RTM), vacuum bagging/autoclave forming and vacuum assisted resin transfer molding (VARTM). Each process has its own advantages and disadvantages and therefore a designer should select the process based on performance, production rate, cost, product size, and product shape. The interest in this study is vacuum assisted resin transfer molding (VARTM).

1.2.1. Resin Transfer Molding (RTM)

Resin Transfer Molding (RTM) is a liquid molding process for thermoset composites that is a closed mold technique and well-suited to fabricate complex structures. In RTM, a dry preform is placed in a matched mold and subsequently, the mold is clamped. Then, thermoset resin system, which is mixed with resin, catalyst, or any other filler material, is pressurized to the mold through a single port or multiple ports until the mold is fully filled with resin. After the impregnation, the part is subjected to curing process depending on the cure kinetics of the resin system. Typically, relative short cure cycles, such as 6 to 30min are preferred for RTM [7].

RTM offers to produce structural parts with very tight tolerances and good surface finish on both sides of the part. Additionally, it a highly cost-effective process to fabricate parts in medium-volume quantities. Figure 3 presents a typical RTM process.

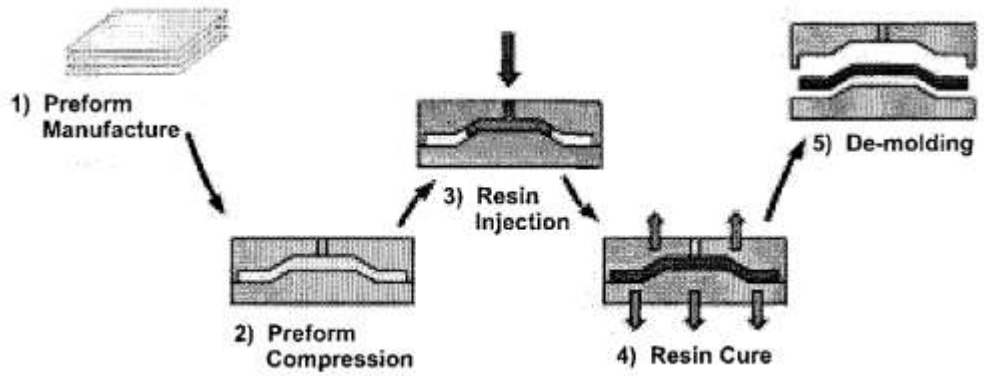

Figure 3. Schematic of RTM process [8]

1.2.2. Vacuum Bagging / Autoclave Forming

Vacuum bagging / autoclave forming is the traditional method to produce advanced composite parts. The process begins with the cutting of prepregs and hand laminating on a one-sided mold. Then, the workpiece is sealed by vacuum bag and excess resin is squeezed out by vacuuming the part. The vacuum bagged part is next transferred to an autoclave where curing process takes place at elevated temperatures under external pressure. Figure 4 presents the schematic of the vacuum bagging / autoclave forming process. Although vacuum bagging / autoclave forming process is majorly used to produce advanced composites, especially for the aircraft industry, it requires high capital investment in the form of an autoclave. Vacuum bagging / autoclave forming is the most energy-intensive among the thermoset composite manufacturing processes; it exhausts almost two times the energy vacuum assisted resin transfer molding process (VARTM) does (Figure 5).

The need for affordable manufacturing techniques has been recognized by researchers, thus there has been growing interest in low-cost techniques such as VARTM to produce advanced composite products.

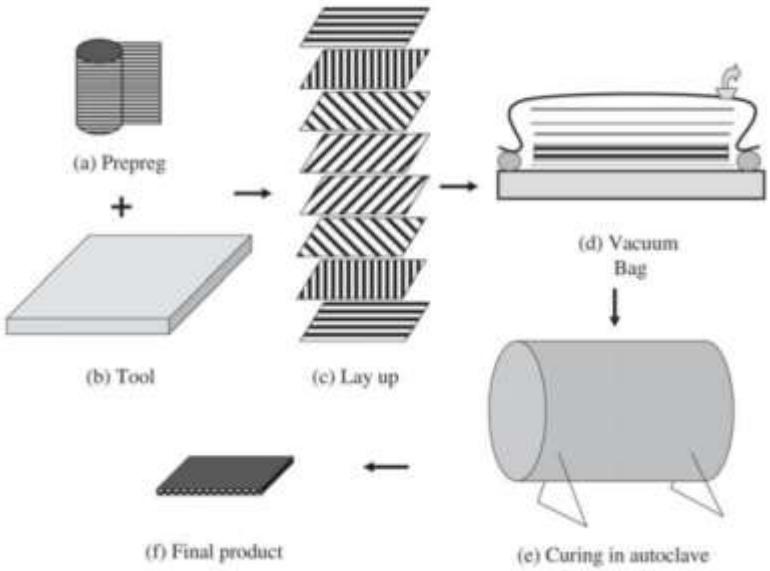

Figure 4. Vacuum bagging / autoclave forming process [9]

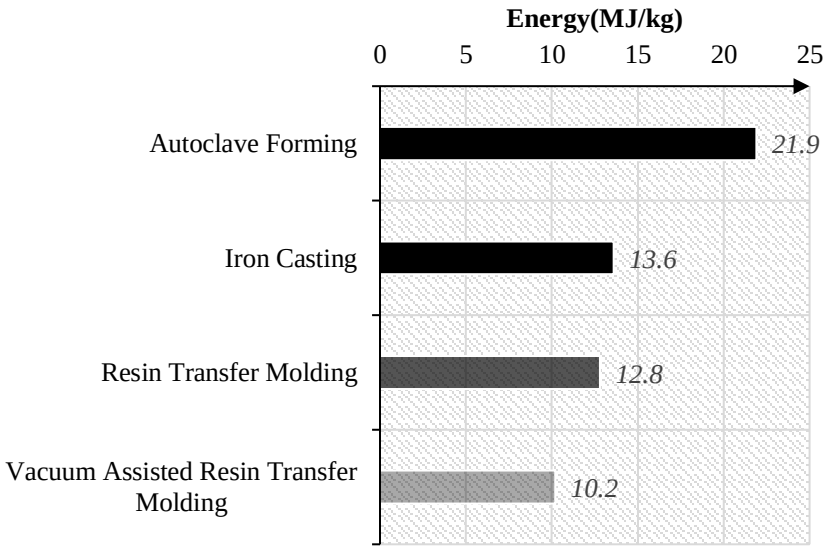

Figure 5. Energy intensities of manufacturing processes (data retrieved from [10])

1.2.3. Vacuum Assisted Resin Transfer Molding (VARTM)

Vacuum assisted resin transfer molding (VARTM) is an alternative to traditional vacuum bagging/autoclave forming process, which is also called as the out-of-autoclave manufacturing technique. VARTM is basically a liquid molding process and a variant of RTM process with its distinguishing characteristic of involving one-sided mold instead of two and using of vacuum to assist in resin flow. Similar to the other liquid molding processes, dry fabric reinforcements are used in VARTM. A typical VARTM process shown in Figure 6. The process involves one-sided tooling with a vacuum bag and distribution media that facilitate resin flow across the fabric preform and then saturation through the fabric preform.

VARTM offers the great advantage to create very large parts using inexpensive tooling. Figure 5 presents the energy intensities of various composite manufacturing processes and it is obviously seen that VARTM is highly cost-effective technique. Additionally, these values in Figure 5 do not include the energy associated with raw materials. Since VARTM employs dry reinforcement, not prepreg, energy consumption included with raw materials of VARTM is unprecedented among other processes.

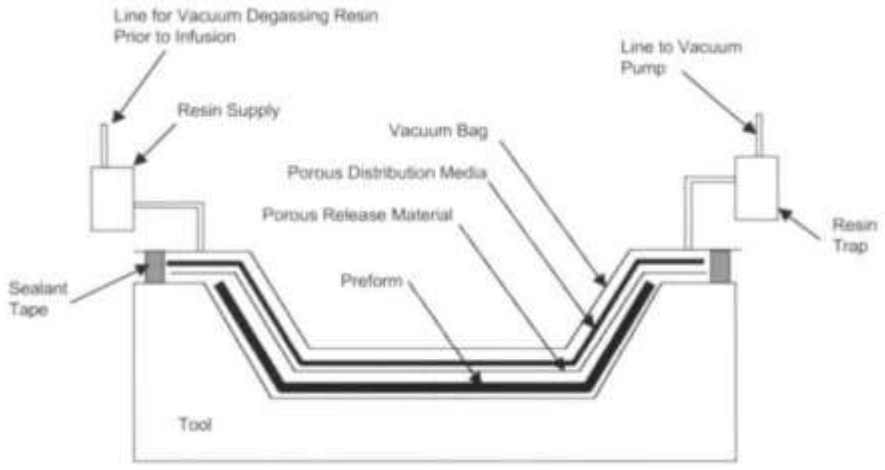

Figure 6. Schematic of a typical VARTM process

1.3. JOINING OF COMPOSITE MATERIALS

As a rule of thumb, joints should be avoided in product design. As joints are typically weak points in the design, most failures emanate from them. Mainly, joining in composites have following disadvantages [7]:

- A joint is a source of stress concentration, which is highly critical considering the fact that fiber reinforced composites possess brittle characteristic.
- Joining of composites is a labor-intensive process wherein special care should be taken.
- Joints increase manufacturing time and cost

Fiber-reinforced composites provide the opportunity to produce large and complicated parts in a single operation while reducing the part count. There are two types of joining method in composites, which are mechanical fastening and adhesive bonding and can be seen in Figure 7.

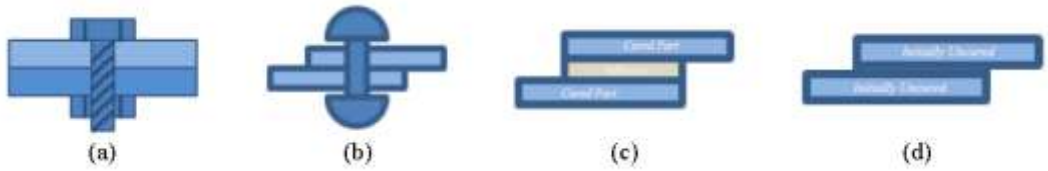

Figure 7. Joining Types of Composites: a) Bolted Joint b) Riveted Joint c) Secondary Bonding d) Co-curing

1.3.1. Mechanical Fastening

Similar to the joints of metal materials, composite materials are also joined using bolts, pins, and screws. In bolted joints, nuts, bolts, and washers are used to create the joint, whereas, in riveted joints, metal rivets are employed.

There are few advantages of mechanical fastening. One of them is that mechanical fastening enables repeated assembling and disassembling. Mechanical joints also offer easy inspection and require little or no surface preparation.

On the other hand, mechanical joints add weight to the structure thereby minimizing the weight-saving potential of the composite structure. Additionally, they cause stress concentration owing to the presence of holes, which is highly critical for composite structures. They have also galvanic corrosion potential in the presence of active metals. Moreover, mechanical fastening creates fiber discontinuity at the location where a hole is drilled, which consequently gets fiber open to environmental attacks.

1.3.2. Adhesive Bonding

Adhesive bonding is the most common joint type of composite materials. Conventionally in this type of joining, two separately manufactured parts are integrated by using adhesives, which is also called as Secondary Bonding. However, another technique called co-curing involves joining uncured composite parts by simultaneously curing and bonding. Co-curing is thoroughly discussed in Section 1.4.

Composite adhesives can be divided into three categories: (1) two-component mix adhesives, (2) two-component, no mix adhesives, and (3) one-component no-mix adhesives. Two-component mix adhesives need mixing prior to the application. They have a good shelf life and typically exhibit good mechanical performance. When using two-component, no mix adhesives, the adhesive is applied on one surface and an activator is applied to the other surface. Curing of adhesive takes place when these two surfaces come together. The adhesive in a one-component category does not require mixing. According to physical forms, adhesives can also be categorized as paste, liquid, and film adhesives.

Adhesive bonding has significant advantages over mechanical fastening. First, the load at the joint interface distributes over an area rather than a concentrated point, which results in uniform stress distribution. As a result of uniform stress distribution, the joint becomes more resistant to mechanical loads, particularly repeated loadings. Furthermore, the additional weight comes from adhesive is negligible compared to that from mechanical fastening. Adhesives not only bond the two surfaces but also seals the joint. Because of this characteristic, adhesive can also prevent galvanic corrosion between carbon fiber composites and metals. Plus, adhesives adapt complex surfaces very well and create negligible small change in part dimensions.

1.4. LITERATURE REVIEW

1.4.1. What is co-curing?

The production cost of composite materials is typically high compared to metallic structures. The motivation of reducing costs of composite fabrication necessitates researchers to investigate on integral molding processes, such as co-curing.

Co-curing is an integral molding technique and another bonding approach in which composite subcomponents are produced in a single shot manufacturing. In other words, co-curing is a process wherein uncured composite parts are cured and bonded simultaneously during the same cure cycle. By integrally co-curing structures, one can greatly reduce the part count and eliminate both metal fasteners and extra processing steps, which in turn cut down the final assembly costs. The motivation of co-curing technique is explained in further detail in Section 1.4.2.

Co-curing is commonly used in aircraft applications, where a large amount of small parts is integrated to form a large structure thereby making assembling process highly challenging and expensive. By unifying small parts into large structures simultaneously, co-curing is a process that promises to cut down both assembling time and cost. Figure 8 shows a typical process of co-curing.

Since it is widely used in aircraft industry, autoclave prepreg molding is often preferred to perform co-curing, which requires high capital investment. However, there are a variety of co-curing techniques as it is discussed in Section 1.4.2 and one of the goals of this study is to provide a low-cost technique for the co-curing process.

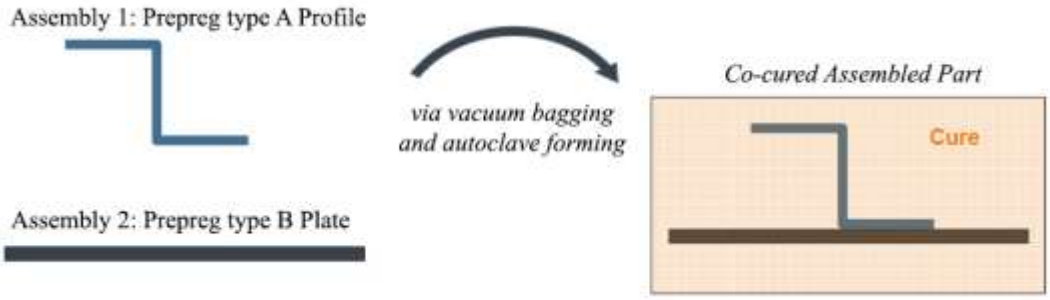

Figure 8. Schematic of a typical co-curing process

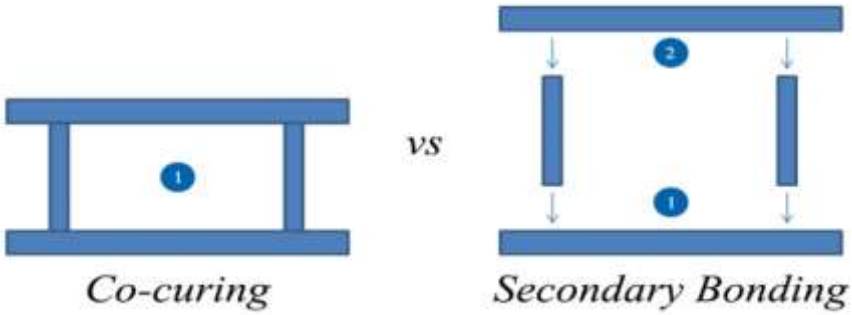

Figure 9. Illustration of Co-curing and Secondary Bonding

1.4.2. Motivation for Co-curing in Aircraft Industry

Sub-structures of aircraft structures mainly consist of stiffened shells such as fuselage frames, ribs, and multi-cell box beams. Conventionally, these stiffened shells are manufactured through a process wherein shells and stiffeners are fabricated separately and then are integrated either through mechanical fastening and secondary bonding.

The main motivation of co-curing is to reduce assembly costs. Three cost-down mechanisms exist for co-curing: (1) eliminating extra processing step, (2) lowering processing time, (3) reducing metal fasteners count.

Using secondary bonding to produce stiffened shells, such as skin-stiffener or skin-web connections, skins and stiffening members or spars are separately fabricated and another curing operation to assemble the skins with stiffeners or spars is required. This additional curing operation is eliminated in the co-curing process, which is illustrated in Figure 9.

It is a trade-off in the case of decreasing processing time. Since lay-up work – placing resin mixtures on a mold at desired angles and places - is complicated in co-curing process, it requires additional lay-up time. Therefore, the advantage of skipping additional curing operations must be weighed against the additional lay-up time. This gets co-curing more feasible in manufacturing large and complex assemblies.

Co-curing provides an opportunity to lower the number of metal fasteners. In McDonnell Douglas AV-8B Strike Fighter Aircraft wing co-curing technique was employed in vertical stabilizer and nearly 60% of fasteners were eliminated [11].

One of the significant advantages of co-curing is the reduction in the part count. In McDonnell Douglas AV-8B Strike Fighter Aircraft wing 62% of part count reduction was achieved [11].

In both mechanical fastening and secondary bonding, materials should be in contact with each other properly and intimately, which is hard to achieve for complex structures. As a consequence of improper contact, undesirable assembly stresses would be introduced in the structure, which is challenging to account in the design. The assembly stresses are deleterious for composite structures and affect the life of structure severely, particularly carbon epoxy composites by virtue of its brittle nature. By co-curing composite substructures, these assembly stresses can be eliminated.

Moreover, structural adhesives that have higher density compared to resins is typically used to adhere sub-structures in secondary bonding. Hence, additional weight in assembly can be presented, which may cause weight penalty in such applications. Plus, high amount of structural adhesive is used in practice compared to that of resin system in a co-cured integration, which also adds more weight to the assembly.

Metal fastening integration generates galvanic corrosion risks for carbon fiber composites. Carbon fiber composites are electrochemically very noble and electrically conductive. Hence, when a metal in contact with a carbon fiber composite, galvanic corrosion takes place. This issue becomes even more serious when a large surface of carbon fiber composites is coupled to small metallic parts, such as metal fasteners. In co-curing integration, resin does not only bond two surfaces but also seals them and consequently lessens the risk of galvanic corrosion for carbon fiber composites.

1.4.3. Co-curing Applications

Co-curing and its tooling technology proprietary in nature and details are mostly not open publicly. The very first application of this technology in the literature is McDonnell Douglas AV-8B Strike Fighter Aircraft wing in the late 1970s [12]. In AV-8B, the major structural elements of the wing and forward fuselage are of composite materials. The forward fuselage is a single-seat structure with the multi-frame and stringer construction. Figure 11 presents the co-cured stiffeners of the AV-8B forward fuselage. Subcomponents in the forward fuselage were co-cured and as a result, 62% of parts were reduced and nearly 60% of fasteners were eliminated according to [12]. Another example is the vertical stabilizer of Lockheed L-1011 [11]. The skin of the stabilizer was co-cured with stiffeners and the spars were designed as a unified body with ribs and webs. By doing so, hundreds of fasteners were eliminated and 50% weight reduction was achieved according to [11].

Figure 10 shows the co-cured vertical stabilizer and front spar of the stabilizer. During the late 1990s, Japanese developed a co-cured wing for XF-2 fighter aircraft in which wing, spars, and ribs were co-cured with the bottom skin [13].

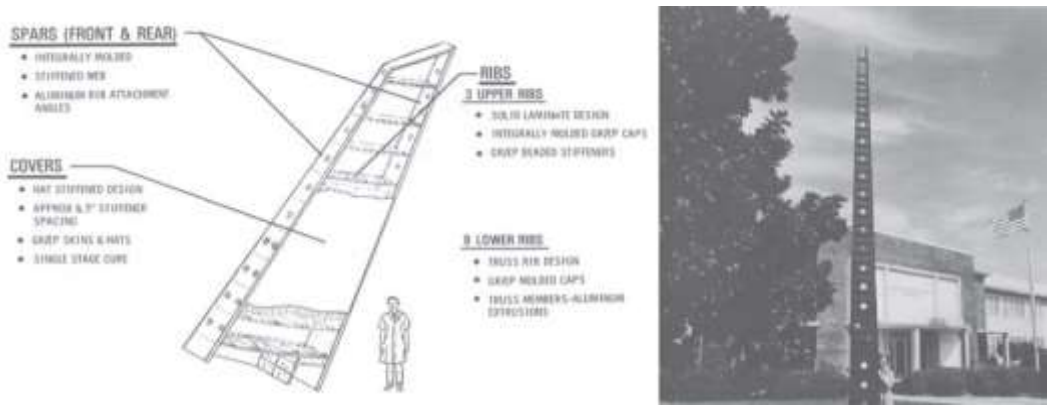

Figure 10. Lockheed L-1011 Tristar Co-cured Composite Vertical Stabilizer and Front Spar [11]

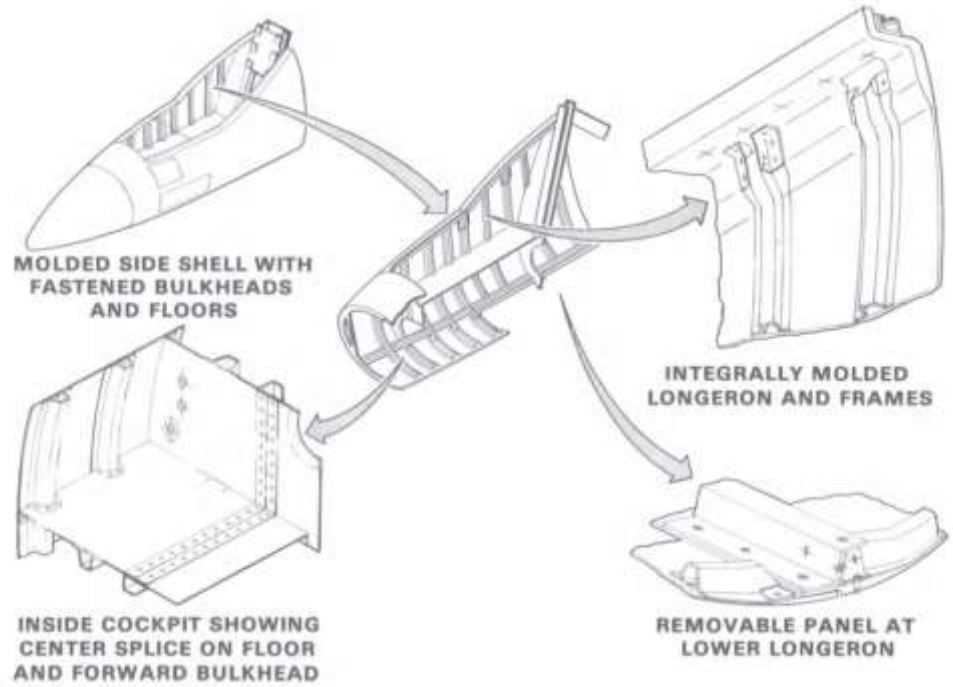

Figure 11. McDonnell Douglas AV-8B Fuselage Co-cured Stiffeners [12]

1.4.4. Co-curing Techniques

So far, a variety of manufacturing techniques have been employed in co-curing technology. Co-curing processes can be categorized according to manufacturing techniques as in Figure 12.

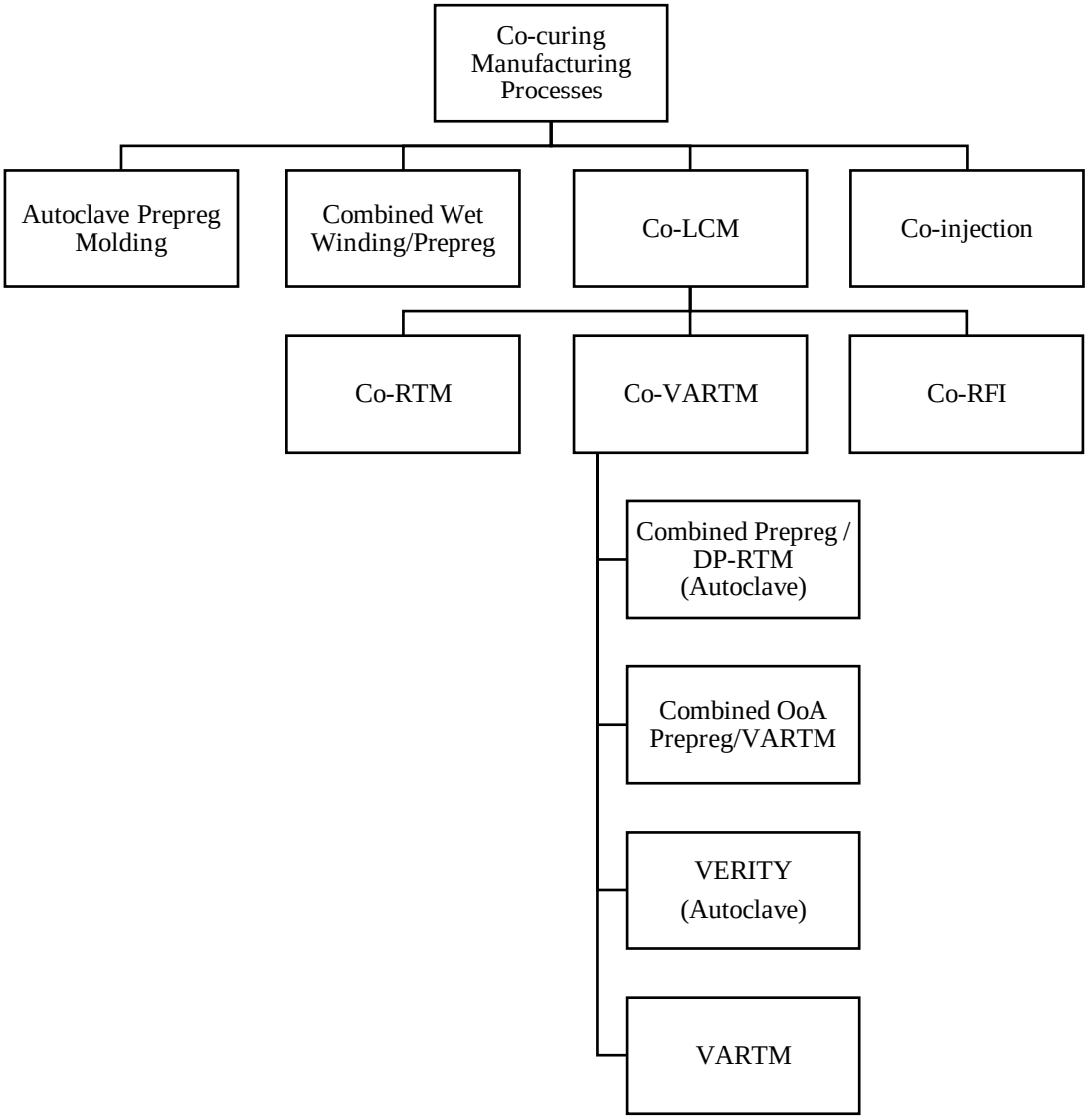

Figure 12. Co-curing Manufacturing Processes

1.4.4.1. Autoclave Prepreg Molding

Autoclave prepreg molding has been the conventional process to manufacture advanced composite aircraft structures. So, this technique was firstly reported in the initial applications of co-curing technology.

Rohr Inc. has developed a pre-shaped hollow mandrel made by pre-preg to create cavities in composite wings, i.e. shown in Figure 13 [14]. The author proposed to utilize this hollow mandrel so that it applies pressure to side walls, bottom, and top skins and creates cavities during vacuum bagging prepreg. In technique the firm proposed, side and top jig tools were also used to apply extra pressure during autoclave curing.

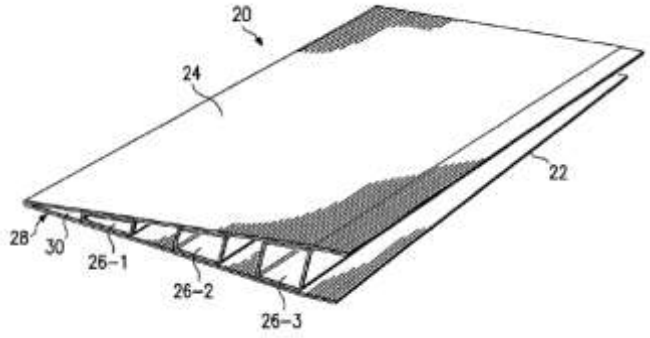

Figure 13. Proposed Co-Cured Composite Wing Structure [14]

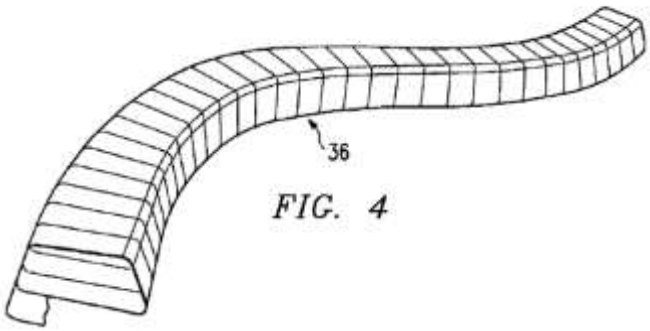

Figure 14. Pre-shaped hollow mandrel made by prepreg [14]

In another technique developed by Rock Mountain Composites Inc. [15], a single piece co-cured composite wing can be fabricated through a co-curing process. The author proposed to use inflatable foam mandrel(core) wrapped by elastic release film. A foam mandrel was inflated by exerting pressure between 30 to 50psi. Reportedly, using such an inflatable foam mandrel could allow a degree of tolerance in assembling and could reduce the void content in a composite structure.

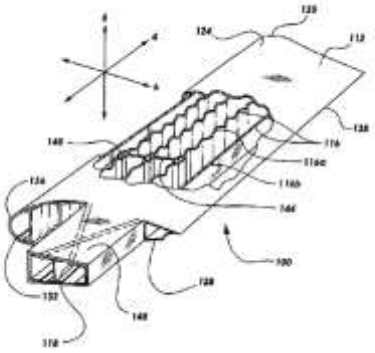

Figure 15. A single Piece Co-Cured Composite Wing [15]

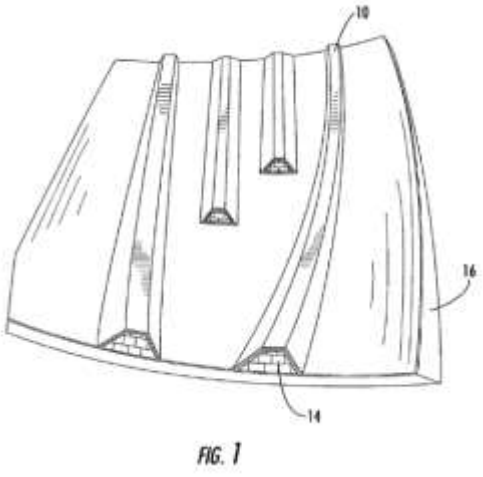

Figure 16. Polymeric, Reusable Mandrel Patented by Boeing Co. [16]

The Boeing Company developed a polymeric, reusable mandrel for co-cured skin stringer production [16]. In the Boeing's invention, small strips were placed in preformed stringer part to apply internal pressure during the curing process, i.e. seen in Figure 16.

1.4.4.2. VARTM

VARTM is an affordable technique for co-curing so that it requires neither autoclave nor prepreg. Co-curing using VARTM was first proposed by Mahruz et al. [17] to fabricate skin-stringers. In the technique, rigid soluble foam mandrels were utilized to create cavities. Molds were also used as tools on which dry fibers are draped. Following the lay-up process, conventional VARTM procedure was carried out and the whole skin-stringer structure was made in one curing cycle. After curing, foam mandrels were dissolved using acetone.

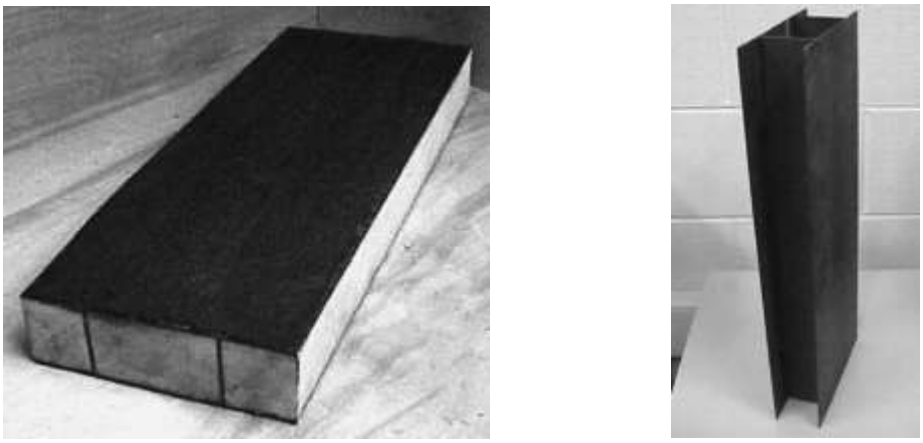

(a) (b)

Figure 17. Photographs of Co-cured Skin Stringer Assembly (a) before foam removal (b) after foam removal [17]

Another example of co-curing using VARTM in the literature is by Japan Aerospace Exploration Agency (JAXA). JAXA manufactured skin stringer assembly in the research program to reduce the manufacturing cost of aircraft structures. They employed a silicon rubber mandrel and VARTM technique to co-cure stringer parts. During curing operation, so-called caul plates, which are curing tool for applying external pressure, were used. Effect of caul plate was additionally investigated in the article and considerable increase in tensile strength was reported [18].

Lockheed Martin also investigated on the capability of co-curing using VARTM process. The company demonstrated the feasibility of process by producing the equipment of the Trident II D5 missile system. It was reported that labor, time and overall costs were reduced and overall 75% cost savings were achieved and 376 fasteners were eliminated by unifying a 61-part assembly [19].

There has been increasing interest in the low-cost co-curing manufacturing processes to produce stiffened shells of aircraft structures. For this purpose, co-curing using VARTM process is used in the present study. The method proposed by Mahruz et al. is followed; however, the application in the current study is a multi-cell box beam, as opposed to skin-stringer presented by the author.

Mahruz et al. experimentally investigated the stability of the skin-stringers fabricated using the co-curing and secondary bonding techniques. However, a thorough comparison of the two techniques were not presented. In the present study, it is intended to present a more detailed comparison study including final part mechanical strength, energy consumption and labor time.

1.5. OBJECTIVE OF THE THESIS

The main objective of this thesis is to develop a low-cost co-cured manufacturing technique using VARTM process for stiffened shells of aircraft structures, particularly multi-cell box beams. Resin impregnation models are constructed to better understand the process and numerical simulations are performed to estimate the resin fill-time. In the co-curing using VARTM process, foam material, foam strength, curing operation and foam coating are considered to be the critical process parameters. These parameters are studied and the co-curing process is developed by selecting the optimum process parameters. In the last part, the co-curing process is compared with the conventional technique, secondary bonding.

The extensive characterization study of composite components is needed to perform accurate resin impregnation simulations. This study also has a wider goal of aiding the simulation tools of composite materials by providing a material data, including preform permeability, porosity, and resin viscosity model. For this purpose, the three-fold approach is followed in this study.

1. To characterize preform and resin properties extensively to improve the simulation accuracy
2. To construct resin impregnation models and perform numerical simulations of the co-curing manufacturing process
3. To fabricate parts that are manufactured via co-curing and secondary bonding and compare two techniques from both manufacturing and final part mechanical properties perspectives.

1.6. THESIS OUTLINE

In the current chapter, the description of the co-curing, its applications and manufacturing processes have been presented along with the motivation leading to its usage in the aircraft industry.

Chapter 2 presents the characterization of composite material components (fiber preform and resin) and generates material data that is used in the subsequent numerical simulations of the process.

In Chapter 3, an analytical modeling of resin impregnation for the VARTM process is presented. Derived formulations, which consider the change in pressure and thickness profile in VARTM process, are then solved numerically. The fill-time solutions are used in Chapter 4 to verify the RTM-Worx solutions.

In Chapter 4, the mathematical background of RTM-Worx, resin flow simulation software for RTM process, is presented. Various simulation models including isothermal, non-isothermal non-reactive, non-isothermal reactive, are generated. RTM-Worx solutions are compared with that found in Chapter 3 to investigate the effects of varying thickness and pressure profile in VARTM. Additionally, validation experiment is carried out and the RTM-Worx results are compared with the experimental results. The best simulation model is found as a consequence of this study.

Chapter 5 presents the experimental investigation of the co-curing process. The co-curing process is improved by studying on the critical process parameters, foam material, foam strength, curing operation and foam coating. The manufacturing procedure of the co-curing and conventional secondary bonding processes for the three-cell composite box beam are given in detail.

In Chapter 6, a comparison of RTM-Worx resin impregnation simulations for the co-cured three-cell box beam and the experiment is made. In the second section, mechanical properties of parts that are manufactured through co-curing and secondary bonding processes are compared. To do so, four-point bending tests are carried out and the test procedure is given in detail. Failure mechanisms, maximum and failure load results are discussed in Chapter 6. In the end of this chapter, a comparison of energy consumption and labor time between two manufacturing techniques is made for the three-cell box beam application.

Chapter 7 presents the conclusions that are drawn highlighting the current study's contributions to the literature.

CHAPTER 2

CHARACTERIZATION OF PREFORM AND RESIN

In this chapter, characterization tests of composite material components, fiber preform and resin, are carried out. The aim of this study is to provide a material data of composite material components to use in resin impregnation simulations. As previously mentioned in Chapter 1, the accuracy of numerical simulations is strongly dependent on the accuracy of material characterization results. Therefore, extensive tests to characterize the preform permeability, preform porosity and resin viscosity are carried out in this chapter.

2.1. MEASUREMENT THEORY

2.1.1. Porosity

The term porosity of dry reinforcement material refers the amount of space in reinforcement that can be filled with resin. Porosity is often calculated as

$$\emptyset = 1 - V_f \tag{1}$$

Basically, the fiber volume fraction is a fraction of the amount of fiber to the total volume and can be calculated as [20],

$$V_f = \frac{nW_f}{h\rho_{fabric}} \tag{2}$$

where n is the number layers, W_f is an areal density of fabric in kg/m^2, h is the sample thickness, ρ_{fabric} is the density of fabric in kg/m^3. Fabric weight per unit can also be calculated as,

$$W_f = \frac{W_{sample}}{hA_f} \tag{3}$$

Eventually, the fiber volume fraction of reinforcement material is,

$$V_f = \frac{W_{sample}}{hA_f\rho_{fabric}} \tag{4}$$

where W_{sample} is the sample weight in kg, A_f is the sample area in m^2. For the carbon fiber, density is taken as 1780 kg/m^3. The porosity of reinforcement materials will be determined experimentally and will be discussed in Section 2.3.

2.1.2. Permeability

Permeability characterizes the easiness of a fluid that flows through a porous medium. In liquid composite manufacturing processes, a resin material is infused into a fiber preform and the motion of the resin is typically modeled as flow through a porous medium. The Darcy's Law governs the flow of resin through the fiber network. One dimensional Darcy's Law can be written as follows,

$$u = -\frac{K}{\mu}\frac{\partial p}{\partial x} \tag{5}$$

In this equation, fluid velocity u is related to permeability K and gradient of the pressure p and viscosity μ. The importance of this equation comes from its simplicity to describe the relationship between pressure drop and the flow rate. If one wanted to use the momentum equations to find such relation, one would have to describe the geometry of every fiber channel, which is almost impossible to solve.

The 1D channel flow method is used to determine the permeability of fiber preform in one direction, where the resin is injected along one edge and the vacuum is applied along the opposite edge [21]. Important to note that assumption of constant thickness and uniform pressure profile is made in this method. The set-up is shown in Figure 18.

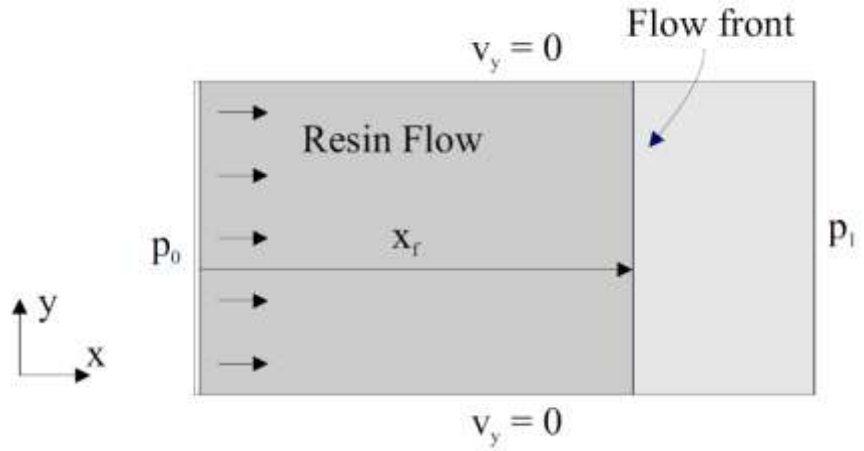

Figure 18. 1D Channel Flow Method [22]

The continuity equation yields the following equation,

$$\frac{d}{dx}\left(\frac{K}{\mu}\frac{dp}{dx}\right) = 0 \tag{6}$$

Assuming that permeability and resin viscosity remain constant the equation becomes a second order ODE,

$$\frac{K}{\mu}\frac{d^2P}{dx^2} = 0 \tag{7}$$

We can solve this equation by applying the following boundary conditions,

$$p(x = x_f) = p_1$$
$$p(x = 0) = p_0 \tag{8}$$

Integrating Equation (7) two times and using the boundary conditions yield a linear pressure distribution during the flow. The pressure difference between inlet and flow front is constant throughout the process, i.e. seen in Equation (9).

$$p(x) = \Delta p \left(1 - \frac{x}{x_f}\right) + p_1 \tag{9}$$

Substituting the pressure distribution into Equation (6), the macroscopic fluid velocity is,

$$u_f = \frac{dx_f}{dt} = \frac{K\Delta p}{\mu \emptyset x_f} \tag{10}$$

where $\emptyset$ is the preform porosity. Taking the integral of Equation (10),

$$\int_{x_f=0}^{x_f} \frac{\emptyset x_f}{K\Delta p} \partial x_f = \int_{t=0}^{t=t_f} \frac{\partial t}{\mu} \tag{11}$$

Eventually, permeability becomes as such,

$$K = \frac{\mu \emptyset}{2\Delta p} \frac{x_f^2}{t_f} \tag{12}$$

The procedure to determine the 1D permeability in channel flow method was demonstrated by Weitzenböck [23]. In the method, Equation (12) is rewritten as follows.

$$K_I = F_I C \tag{13}$$

where F_I and C denote material term and process term respectively and are given as

$$F_I = \frac{N_I}{t_f} \tag{14}$$

$$C = \frac{\mu \emptyset}{2\Delta p} \tag{15}$$

and N_I for the 1D channel flow is,

$$N_I = x_f^2 \tag{16}$$

The method of Weitzenböck [23] is applicable for both isotropic and orthotropic materials and here, I notation denotes the effective permeability. The process term C is constant, whereas N_I changes with respect to time. In the method, the plot of N_I versus t_f is drawn by using experimental data and the slope of curve-fit of that equation gives the average F_I. Eventually, the average permeability can be calculated by using (12).

2.1.3. Viscosity

Viscosity characterizes the resistance of fluid against to flow or deform. The term is more simply defined as a friction between the fluid molecules. Resin viscosity has great importance in composite manufacturing.

In general, the viscosity is a function of temperature, pressure, degree of cure and shear rate and is expressed as follows.

$$\eta = \zeta(p)\psi(T)\zeta(\alpha)\lambda(\dot{\gamma}) \tag{17}$$

where $\zeta(p)$, $\psi(T)$, $\zeta(\alpha)$ and $\lambda(\dot{\gamma})$ are functions of pressure, temperature, degree of cure and shear rate respectively.

The effect of pressure is highly negligible for VARTM process. Typically, it is taken into consideration for high-pressure injection molding and resin transfer molding [24].

Fluids can be categorized as Newtonian or non-Newtonian based on shear rate dependence. For a Newtonian fluid, the viscosity is a constant and can be expressed as,

$$\begin{aligned} \boldsymbol{\tau} &= \eta\dot{\boldsymbol{\gamma}} \\ \eta &= \mu \end{aligned} \tag{18}$$

Resin behaves almost like a Newtonian fluid and is assumed to be independent of the shear rate [22]. Eventually, resin viscosity in this study depends on temperature and degree of cure, i.e. expressed as follows. The rheology measurement is carried out and the viscosity-shear rate dependence is investigated in Section 2.2.2.

$$\mu = \psi(T)\zeta(\alpha) \tag{19}$$

2.2. RESIN

2.2.1. Measurement of Resin Viscosity

The rheometer is an instrument that can measures viscosity and viscoelastic properties of fluids, semi-solids, and solids. There are two main types of rheometers: (1) Shear rheometers that control the applied shear stress or shear strain (2) Extensional rheometers that apply extensional stress or strain. Shear rheometers also differentiate based on the loading conditions and most commons are concentric cylinders, cone and plate and parallel plate type rheometers. Each type is suitable for distinct applications, for instance, cup and cone type rheometers are suitable at low shear rates, whereas capillary rheometers at high shear rates. In the case of resin viscosity measurement, particularly for temperature dependence measurement of thermoset resins, parallel plate rheometers are highly preferable.

Rheological measurements for resin are conducted by using TA, AR2000 rheometer, which is a parallel plate type shear rheometer. Parallel circular plates having a diameter of 25mm with the maximum gap of 1mm under the flow mode are chosen in this study. Figure 19 shows the rheometer used in measurements and Figure 20 presents the parallel plate apparatus. The resin system used in this study is Huntsman XB 3585 Epoxy Resin and Huntsman Hardener XB 3486 [25].

Figure 19. TA Instruments, AR2000 Rheometer

Figure 20. Rheometer parallel circular plates

2.2.2. Effect of Shear Rate

The flow sweep test was first carried out due to several reasons. As discussed in Section 2.1.3, thermoset resin was assumed as a Newtonian fluid by different authors, this study aims to provide experimental results to validate this assumption. Additionally, if the assumption would not be validated, shear rate effect should be taken into account in the whole rheological measurements. For these reasons, flow sweep test in which shear rate is taken as an independent variable was conducted. Neat resin was sampled in this measurement and the test was taken at 40˚C, which is the process temperature.

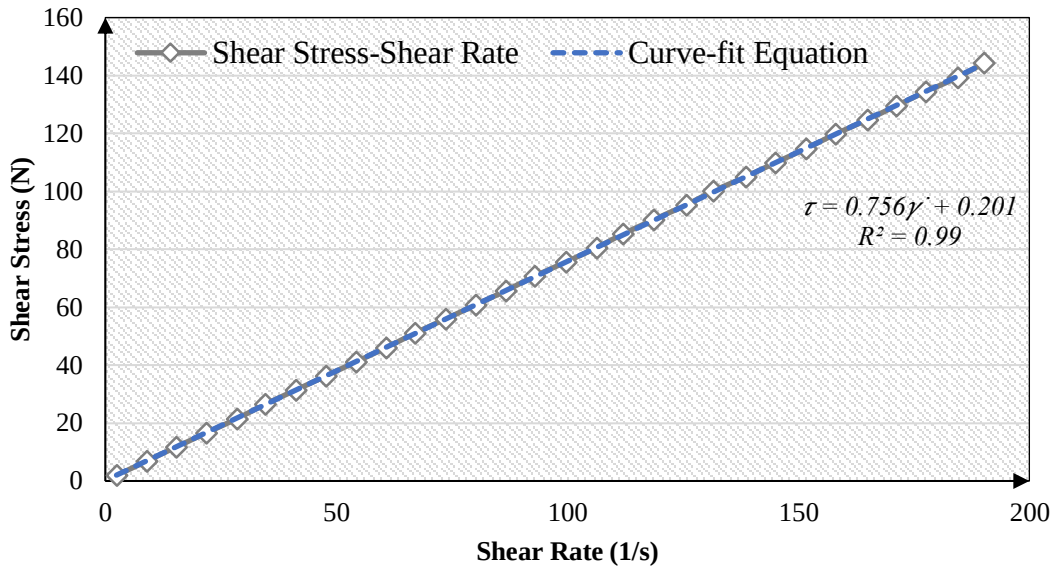

Figure 21. Resin without catalyst shear stress as a function of shear rate

Figure 21 presents the relationship between shear stress and shear rate. Equation (18) states that the slope of this curve presents the viscosity of a Newtonian fluid and the curve-fit equation is given in Equation (20).

$$\tau = 0.756\dot{\gamma} + 0.201, R^2 = 0.99 \quad (20)$$

Curve-fit equation conforms very well with the curve with a fit parameter, R^2, of 0.99. Hence, one can conclude that the resin exhibits Newtonian fluid characteristic due to the fact that the curve fits with a linear trendline. This finding confirms results in the literature [22].

2.2.3. Effect of Temperature

Having analyzed the effect of shear rate, the temperature effect on viscosity was investigated and the temperature sweep test was conducted. Since the resin viscosity is independent of shear rate, the shear rate was selected as 50Hz, which was thought to be a convenient speed for the rheometer. Only the epoxy resin was measured in the test. The temperature was increased from 30˚C to 120˚C and the temperature ramp rate was selected as 5 ˚C/min.

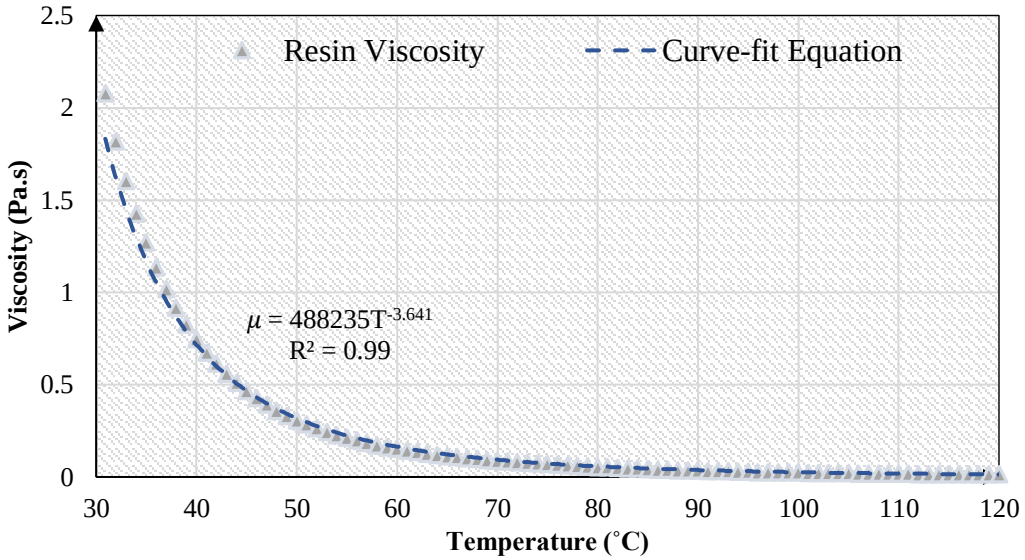

Figure 22. Resin viscosity as a function of temperature

Figure 22 shows the result of temperature sweep test. The curve fit is acquired from the result, i.e. given in Equation (21). The equation perfectly fits with the curve and therefore, one yields a conclusion that the resin viscosity decreases as temperature increases.

$$\mu = 488235T^{-3.641}, R^2 = 0.99 \quad (21)$$

The viscosity is highly dependent on temperature and even small changes in temperature can yield a radical decrease in the viscosity. By taking a reference value at 30˚C, the percentage of viscosity change is plotted in Figure 23 as a function of temperature. It is seen from the figure that even 5 ˚C increase in temperature causes a 40% decrease in resin viscosity. In the light of these results, one needs to be very careful of making constant viscosity assumption in composite process modeling

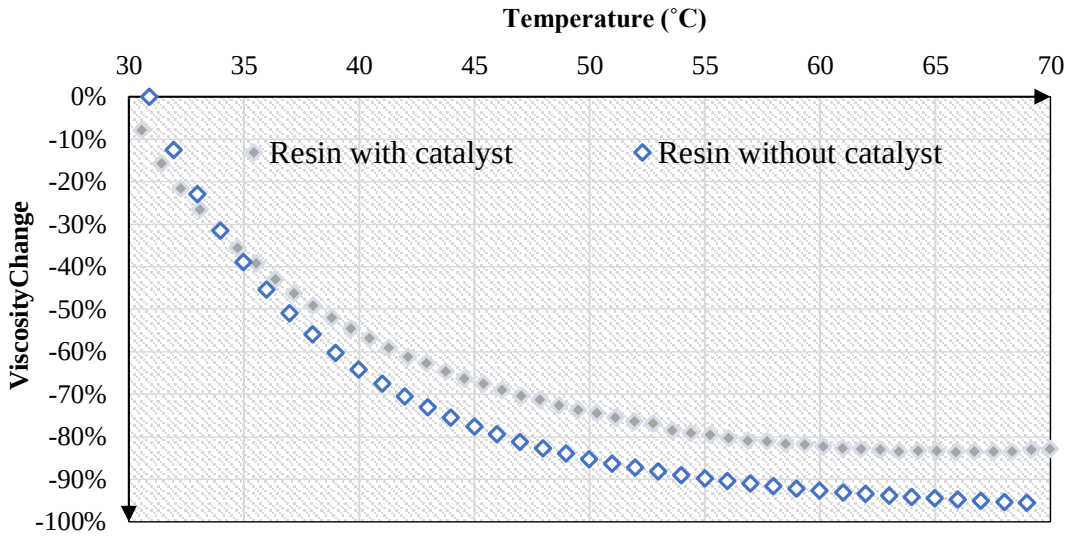

Figure 23. Change in viscosity with respect to 30˚C as reference

2.2.4. Effect of Curing

Since chemical reaction sets in, the resin starts the cross-binding process whereby its viscosity increases. The term, chemorheology, is used to define the viscoelastic behavior of chemically reacting system such as resin system. As described earlier, the viscosity is a function of temperature and degree of cure and can be expressed follows.

$$\mu = \psi(T)\zeta(\alpha) \tag{22}$$

Initially, the temperature effect on resin system during curing was investigated. Temperature dependence of the resin-catalyst mixture was evaluated and plotted in Figure 23. Additionally, results of the resin-catalyst mixture were compared with that of neat resin to better understand the effect of temperature during curing. It is observed from Figure 26 that the resin-catalyst mixture is highly susceptible to temperature change similar to the neat resin.

Figure 26 presents the comparison of resin with and without the catalyst. The curve fit equation was achieved and given in Equation (23). Again, the calculated equation highly matches with the curve and the viscosity declines as temperature rises.

$$\mu = 819.34T^{-2.191}, R^2 = 0.98 \quad (23)$$

The exponential model is frequently used to predict the temperature dependence of liquid viscosities. Hence, an exponential curve-fit equation is also acquired from Figure 25, i.e. given below.

$$\mu = 1.5549e^{-0.045T}, R^2 = 0.93 \quad (24)$$

Arrhenius Model is also often preferred to model the temperature relation of resin viscosity. The model has following equation.

$$\mu = \mu_0 e^{\frac{E_0}{RT}} \quad (25)$$

here μ_0 and E_0 are empirical constants and R is the ideal gas constant, i.e. 8.314 J/k.mol. To fit the Arrhenius model, the temperature is converted to Kelvin. Then, ln μ is plotted versus the inverse of temperature, which is shown in Figure 24. In Figure 24, the slope of the straight curve-fit line gives $\frac{E_0}{R}$, while the intercept is $\ln\mu_0$. R^2 presents the goodness of fit of the curve-fit line and reaches its maximum value, 1, when the curve-fit line matches perfectly with data.

The Arrhenius Model fit the experiment results is found as follows.

$$ln\mu = ln\mu_0 + \frac{E_0}{R}\left(\frac{1}{T}\right) \tag{26}$$

$$ln\mu = 4731.8\left(\frac{1}{T}\right) - 16.415, \quad R^2 = 0.95 \tag{27}$$

And the Arrhenius curve-fit equation is calculated as below.

$$\mu = 7.431x10^{-8}e^{4731.8\left(\frac{1}{T}\right)} \tag{28}$$

where $\mu_0 = 7.431x10^{-8}\ Pa.s$ and $E_0 = 39310\ \frac{J}{mol}$.

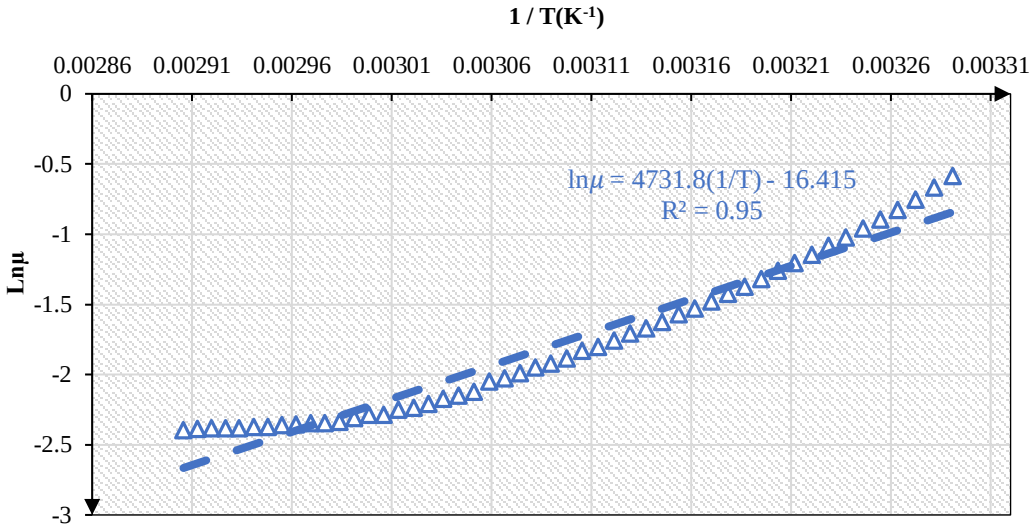

Figure 24. Arrhenius model plot: ln(μ) vs 1/T(K)

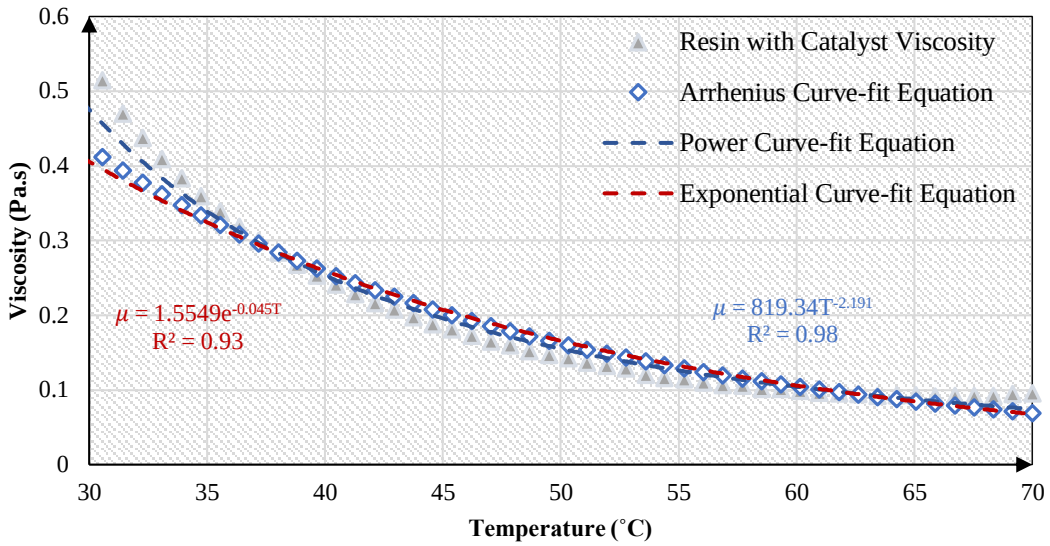

Figure 25. Resin with catalyst viscosity as a function of temperature

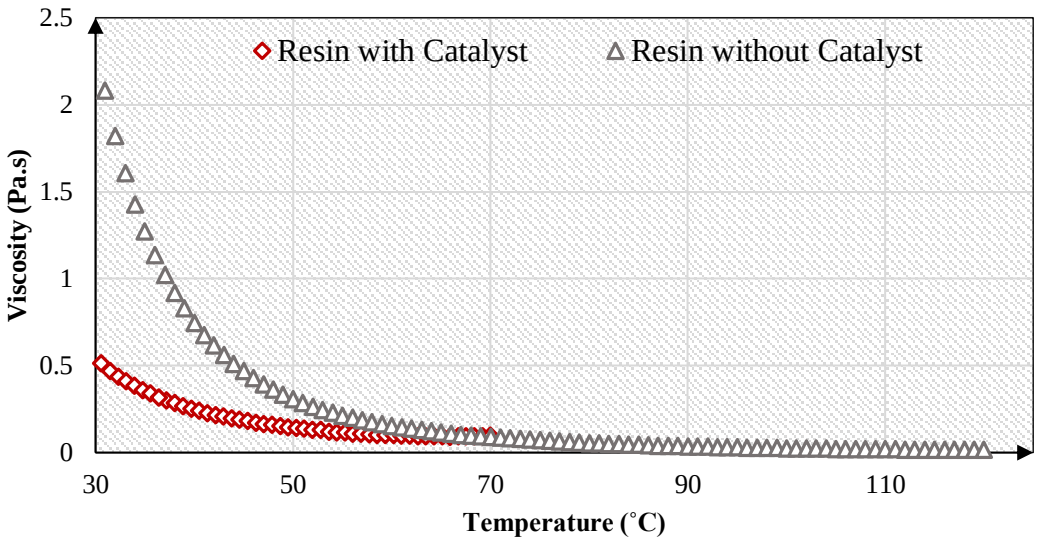

Figure 26. Resin with and without catalyst viscosities as a function of temperature

Many chemorheology models have been developed so far to describe the chemical reaction effect on viscosity. Among them, Castro-Macosko model is very popular to characterize the pre-gel stage of the resin system. Castro-Macosko Model is shown below [26].

$$\mu = \mu_0 \, e^{\frac{E_0}{RT}} \left(\frac{\alpha_{gel}}{\alpha_{gel} - \alpha} \right)^{c_0 + c_1 \alpha} \tag{29}$$

Here α_{gel} is the critical conversion at gelation and is determined by DSC measurements. For similar epoxy resin system, the critical conversion was taken as 0.894 by [27] and the same value was selected in this study. Another significant model was proposed by Lee and Han [28], which has the following form.

$$\mu = \mu_0 \, e^{\frac{E_0}{RT}} \, e^{(d_0 + \frac{d_1}{T})\alpha} \tag{30}$$

The isothermal time hold test was conducted. Since the temperature dependence of viscosity is coupled with degree of cure, the isothermal test was carried out to analyze the chemical reaction effect. The test was carried at 40˚C, which is the process temperature. In the test, the shear rate was adjusted as 50 Hz as in previous tests. The gel time is stated as 80minutes at 40˚C [25] and thus the fraction of gel time was calculated by using that value. Figure 27 shows the viscosity change of resin-catalyst mixture with respect to the fraction of gel time. Resin viscosity gets high as curing reaction advances. Eventually, the viscosity reaches to infinity when the reaction is complete. Exponential characteristic was obtained from the result of time hold test, i.e seen in Figure 27, and the curve fit equation is given in Equation (31).

$$\mu = 0.1669 e^{1.6102\alpha}, R^2 = 0.999 \tag{31}$$

$$\alpha = \frac{t}{t_{gel}} \tag{32}$$

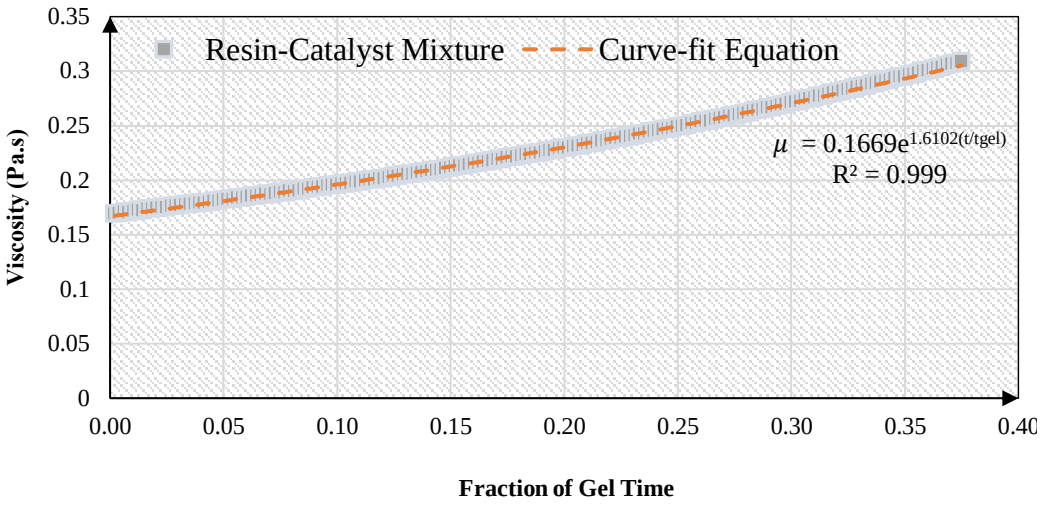

Figure 27. Resin with catalyst viscosity with respect to the fraction of gel time

Castro-Macosko Model parameters were evaluated by using experimental data. At least two experimental data were required to calculate the parameters A and B. The evaluated equation is as follows.

$$\mu = 7.431x10^{-8}e^{4731.8\left(\frac{1}{T}\right)}\left(\frac{\alpha_{gel}}{\alpha_{gel}-\alpha}\right)^{-11.133+83.648\alpha} \quad (33)$$

Similarly, Lee-Han Model fitted the results and the model parameters were evaluated by using two experimental data. Lee-Han Model is found as such.

$$\mu = 7.431x10^{-8}e^{4731.8\left(\frac{1}{T}\right)}e^{\left(-0.479+\frac{1.432}{T}\right)\alpha} \quad (34)$$

2.3. PREFORM

2.3.1. Porosity Testing of Preform

Constant porosity assumption is often made in flow simulations, which is also the case in RTM-Worx Flow Simulation Software. Porosity, indeed, is a function of compaction pressure. But also, it might be influenced by the stacking sequence. Thus, the porosity of carbon fiber preforms in the different number of layers and under different vacuum pressures was investigated to understand the influence of compaction pressure and a number of layers. If the constant porosity assumption remains valid, the permeability of reinforcements can also be assumed to be unchanged during the process.

In addition to the aforementioned tests, porosity values of reinforcements have to be determined to implement in numerical simulations. Each reinforcement material including distribution media and peel ply was tested in this study.

The porosity test procedure begins with cutting the small piece of reinforcement material as a test specimen. The specimen is weighed carefully by using a precise digital scale. Then the physical measurement of a specimen including thickness and surface area are made. It is highly important to measure physical properties accurately, as they greatly influence the calculated porosity value.

Having completed the physical measurements, the specified number of reinforcement material is draped on the mold plate and small piece of peel ply is placed on an edge of the material. The purpose of using peel ply is to provide vacuum continuity on the part.

Next, spiral tubes are position and a vacuum bag is placed on the reinforcement material. The workpiece is then sealed off by using sealant tape. To measure the thickness change under vacuum pressure a dial gauge is employed as in Figure 28. At this point, it is highly essential to be sure about preloading the dial gauge. Since the dial gauge should be in contact with the part seamlessly during the test, a small amount of preload is applied prior to the test. To do so, a small washer is placed under the tip of the dial gauge. Another important point is that as the surface of reinforcement material is rough, slight local differences in thickness change might occur. Placing a washer under the gauge tip, as in Figure 28, is highly beneficial to average the thickness change and alleviate this effect. Thickness change is recorded during the test by the video camera and the porosity is calculated by using Equation (1) and Equation (4). Figure 28 presents the illustration of porosity test set-up.

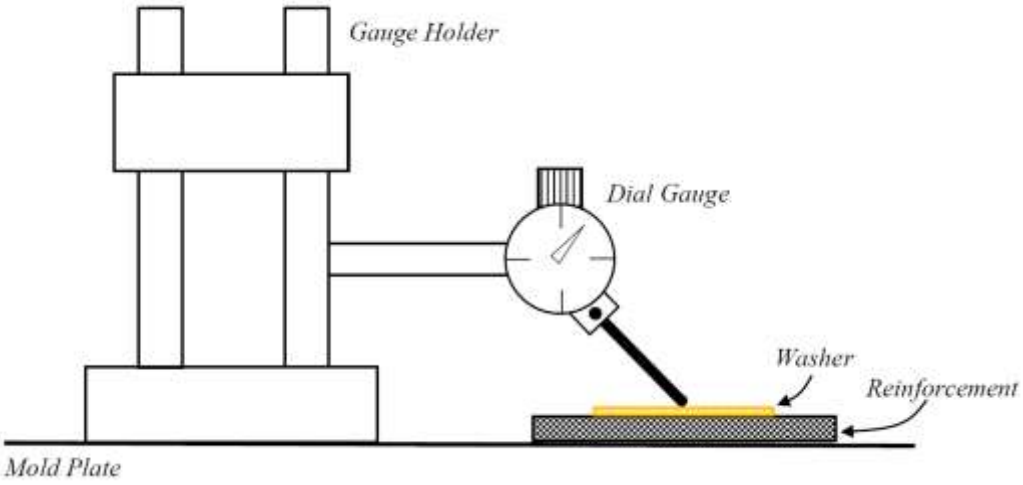

Figure 28. Illustration of porosity test set-up

2.3.1.1. Distribution Media

Distribution media is an extruded plastic material that is composed of polyamide and polyethylene. Distribution media is a highly permeable material that is used to accelerate the resin flow in VARTM process and is provided by Metyx (Turkey). It is comparatively stiffer and denser among other reinforcements, therefore, a relatively small thickness change under vacuum pressure is expected.

Figure 29 shows the porosity test of distribution media. The porosity was measured under vacuum pressures from 100mmHg to 700mmHg and the results are given in Figure 37. Expectedly almost no change was observed, as the vacuum pressure raises. This can be explained by considering the fact that distribution media is a solid-like structure and is stiffer compared to other reinforcement materials. The test results also show that distribution media has the highest porosity, which makes sense by considering its perforated structure.

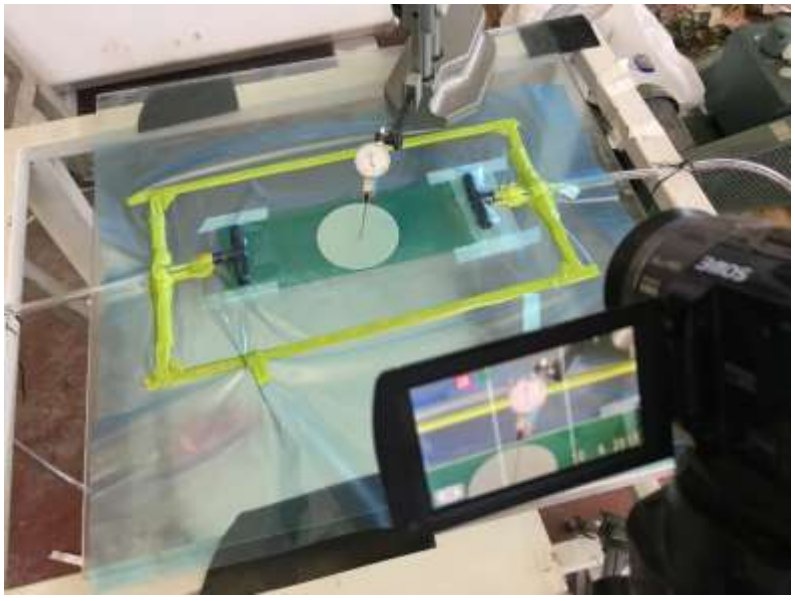

Figure 29. Photography of distribution media porosity test

2.3.1.2. Peel Ply

Peel ply, also called as release fabric, is a disposable cloth that aids the removal of the cured part. Peel ply is basically a woven polyamide fabric coated with a release agent. The peel ply material is provided by Metyx (Turkey). It has a texture that creates porous finish on the part, which is desirable for subsequent adhesive bonding. Peel ply used in this study has 80 g/m^2 areal density and plain weave.

Figure 30 presents the porosity test of peel ply. Similar to distribution media tests, the vacuum pressure was changed from 100mmHg to 700mmHg to understand the pressure effect on porosity. The test results are shown in Figure 37. It is obvious from the results that peel ply has the lowest porosity value and this is the result of its polyamide and tight weave nature.

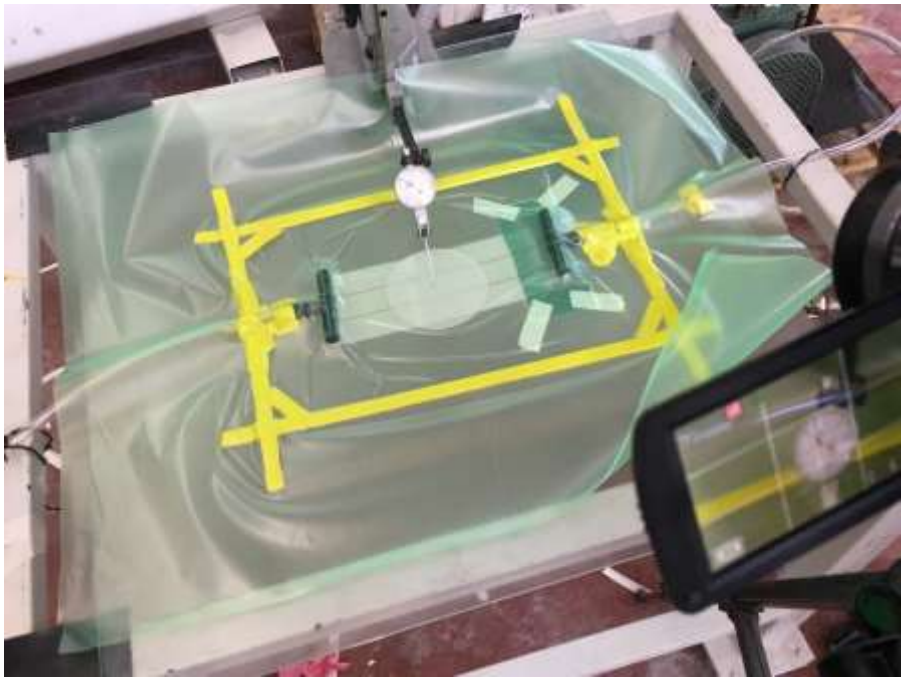

Figure 30. Photography of peel ply porosity test

2.3.1.3. Carbon Fiber Preform

Carbon fiber preform is plain weave fabric woven that has 200 g/ m^2 areal density. Carbon fabric, supplied by Spinteks (Turkey), is wounded by using 3K tows - meaning 3,000 filaments are used in a tow. To measure the porosity, first physical measurement of fabric was made. All fabrics were cut in 300mm x 400mm dimensions and each was weighted as 24 grams. The thickness of fabric was 0.3mm. Figure 31 presents the test set-up of porosity test of carbon fiber preform. The test results show that carbon fiber preform has around 0.50 porosity value, i.e. higher than that of peel ply.

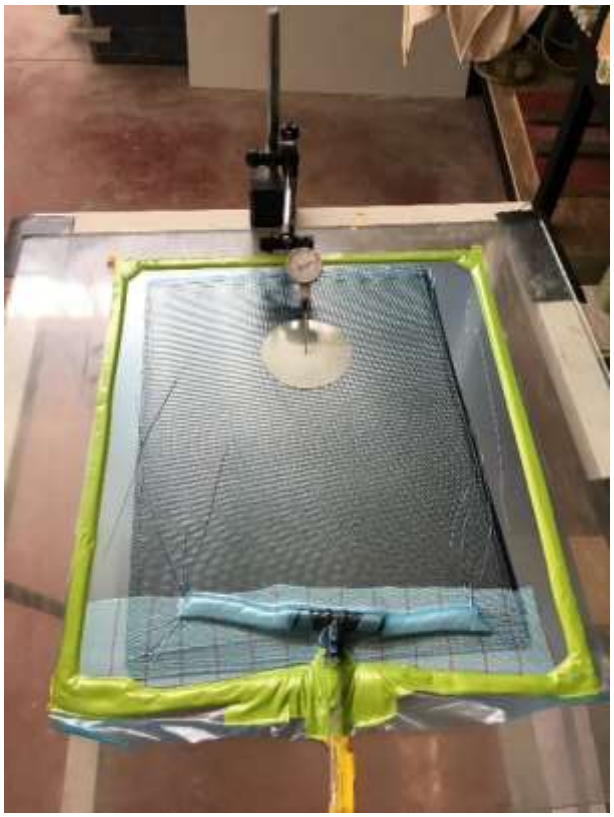

Figure 31. Photography of carbon fiber preform porosity test

2.3.2. Effect of Stacking the Preform on Porosity

The effect of the number of preforms on porosity was investigated using two, five, seven and ten layers of 1x1 plain, 200g/m^2 carbon fiber preforms. Initially, physical measurement of fabric was made. Again, all fabrics were cut in 300mm x 400mm dimensions and each was weighted as 24 grams.

Having obtained the physical properties, change in preform thickness was measured precisely in a set-up shown in Figure 32and Figure 33. Preforms were stacked on a glass plate and were sealed off using sealing tape. A layer of peel ply was placed along the preform and the spiral tube was positioned on the top of peel ply. The vacuum was applied through a layer of peel ply to 10mbar level. The thickness was measured using a dial gauge, shown in Figure 32and Figure 33. The dial gauge needed to press the preform continuously, thus a small preload was applied on the tip of the gauge. Since dial gauge made a point contact with the preform, a small shim was put under the tip in order to average the collapse of the preform. In each test, the thickness was measured before and after vacuum. To stabilize the vacuum pressure, the vacuum was applied minimum 10 minutes and the last measurement was taken after the dwell time.

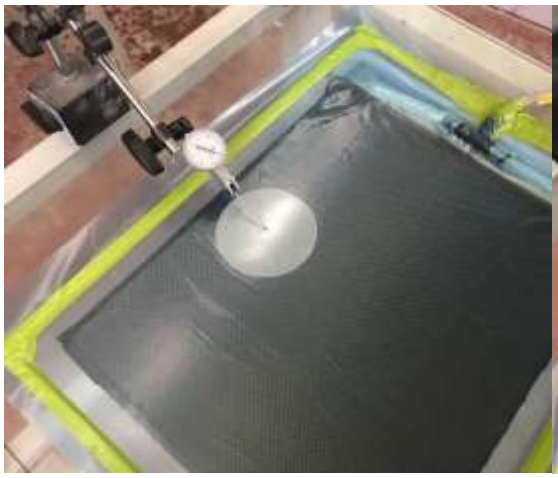

Figure 32. Picture of Porosity Test Set-up

Figure 33. Picture of Porosity Test Set-up

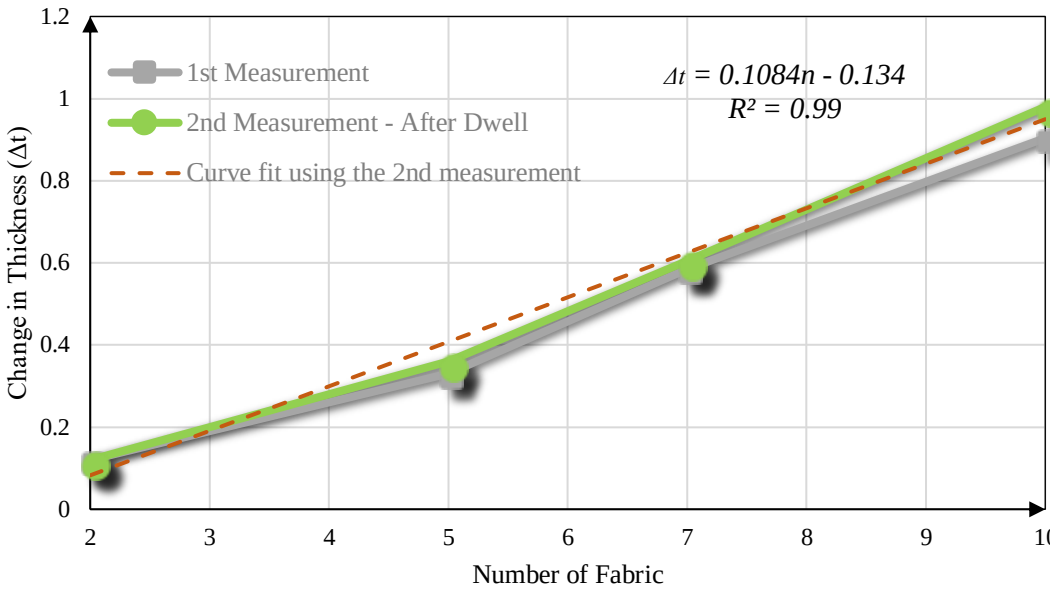

Figure 34. Change in Thickness vs Fabric Count

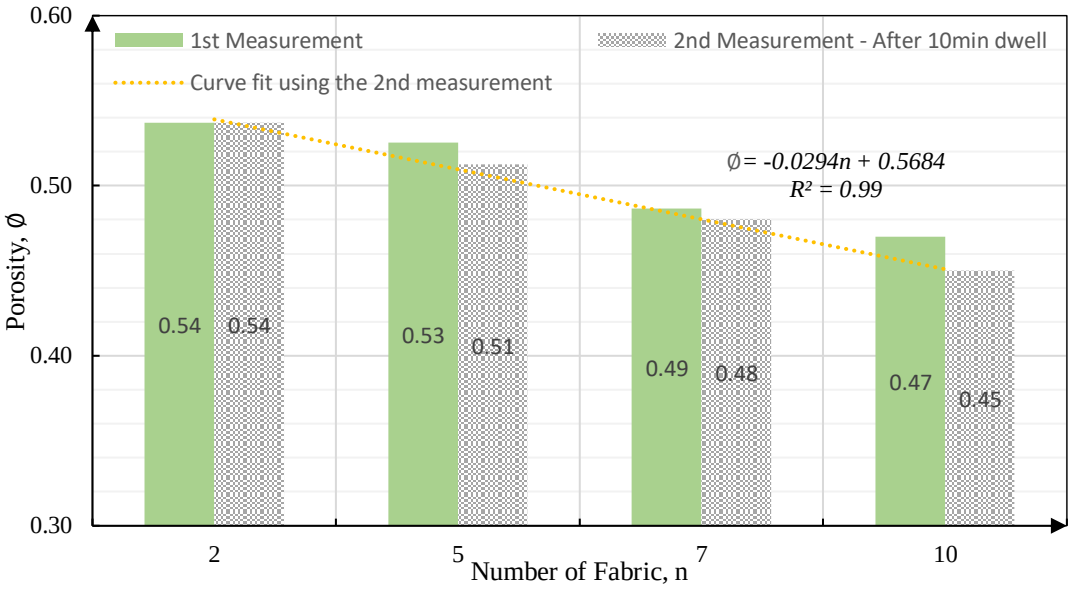

Figure 35. The porosity of carbon fiber fabric with respect to the number of layer count

The change in thickness with the different number of fabric layers is seen in Figure 34. The results show a linear relationship between the collapse of preform and number of layers, which is expected. Even though the rough surface of preform could be effective on the thickness measurement, the results highly fit with a linear trendline having fit parameter R^2 of 0.99.

The porosity of uncompressed carbon fiber preform was calculated as 0.63. The measurement was taken when the preform was initially compressed and after 10 minutes' dwell. As it is seen in Figure 35, there is no considerable difference between two measurement points. Hence, it is concluded that holding preform under vacuum – maximum 10 minutes - has no significant effect on preform porosity.

Another significant conclusion is a tendency to decrease in porosity as the preform count gets high. By considering Figure 2, it is seen that at almost all vacuum levels, porosity values are lower in the higher number of preform. This effect is more obvious in the lower vacuum levels. For instance, the porosity values are 0.58, 0.57, 0.56 and 0.54 at 100mmHg vacuum for 2 layers to 10 layers. The same conclusion was made by Saunders et al. [29] for the number of fabric between 1 and 5. Nevertheless, Saunders found that this effect gets less dominant for the number of fabric greater than five.

2.3.3. Effect of Vacuum Level on Porosity

Having analyzed the effect of the preform count, the effect of the vacuum level on preform porosity was investigated by changing the vacuum level from 100mmHg to 700mmHg. Again, 1x1 plain weave, 200gr/cm^2 carbon fiber preforms, which are reinforcement materials for our fabrication, were studied. Porosity test was made with two, five, seven and ten layers of fabrics under the vacuum level changing from 100mmHg to 700mmHg.

Physical measurement of preforms was required to calculate the porosity, therefore, preforms were weighted and measured prior to the porosity test. All fabrics had a size of 300mm x 400mm x 0.3mm and each was 24 grams.

Having done the physical measurement, preforms were stacked on a glass plate and sealed off with the sealant tape. A layer of peel ply that provided the vacuum continuity was placed locally on preforms. The thickness measurement was again made through a dial gauge that is shown in Figure 36 and a piece of the washer was again put under the gauge tip. Tests were conducted with preform numbers changing from 2 to 10 and in each test the vacuum level was adjusted from 100mmHg to 700mmHg with 100mmHg vacuum pressure increment.

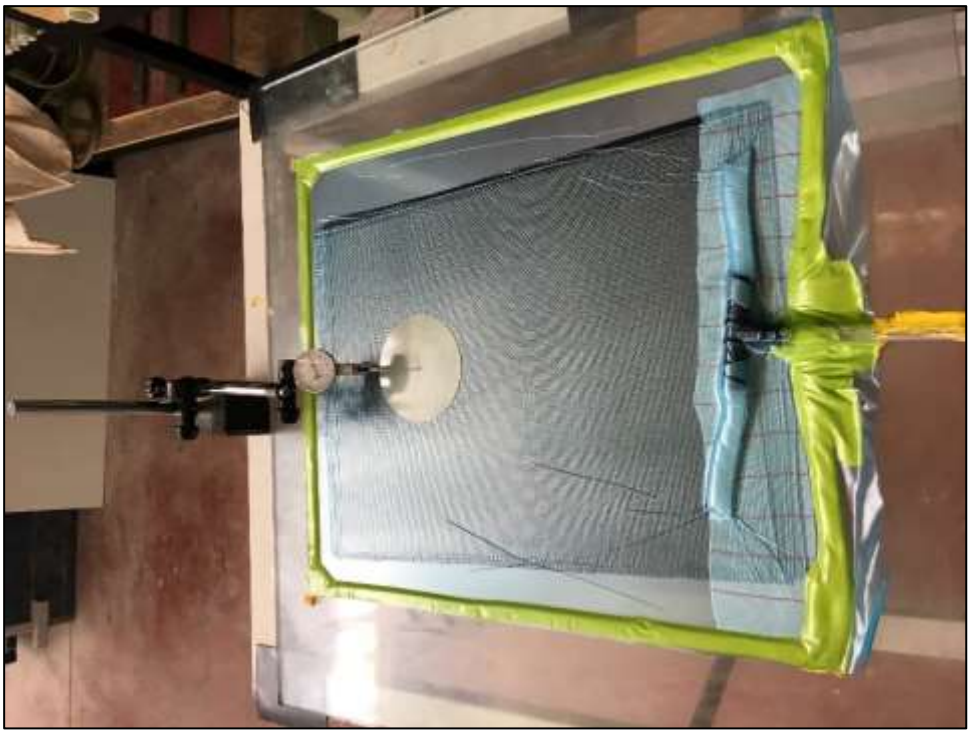

Figure 36. Picture of Porosity Test

In the light of test results, it can be concluded that as the vacuum level increases porosity decreases. For instance, in the 2 layers experiment porosity values change from 0.58 to 0.52 when the vacuum level increases from 100mmHg to 700mmHg. This tendency is the case for other experiments too. In the 5 layers experiment, change of porosity is from 0.57 to 0.51, whereas the porosity decreases from 0.56 and 0.54 to 0.50 in 7 layers and 10 layers respectively. Also need to mention that the uncompressed porosity of the preform was calculated as 0.63, which is the highest value for all case.

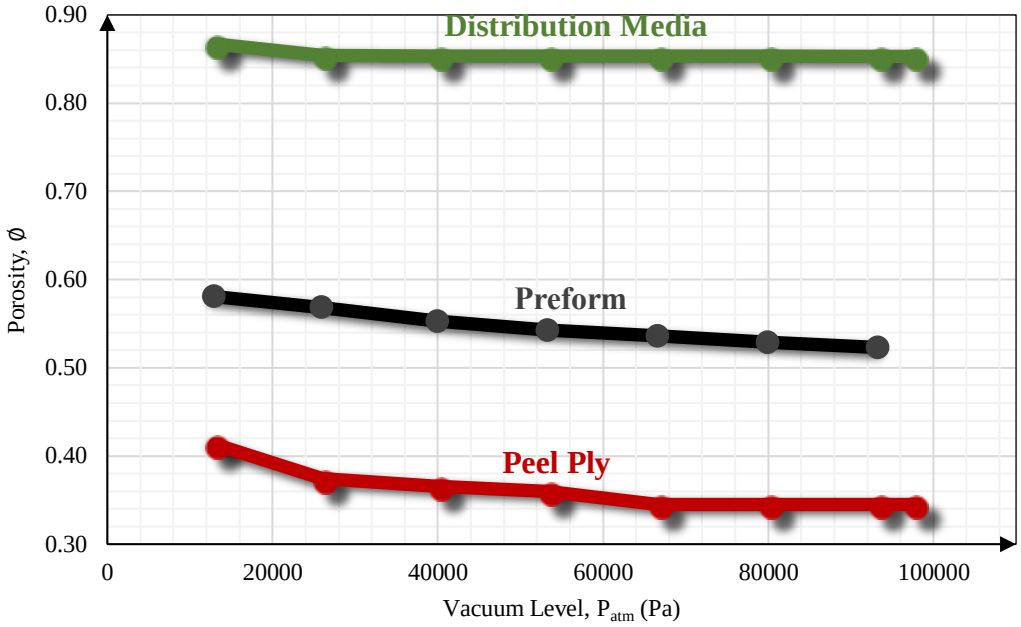

Figure 37. The porosity of layers with respect to the vacuum level

Another observation is that reinforcements have lower porosity under vacuum compared to the uncompressed state. This was investigated by Saunders et al. [29] and was concluded that increase in compaction pressure results in higher fiber volume ratio. In the light of test results, the same conclusion can be made.

2.3.4. Permeability Testing of Preform

Permeability test of fabric reinforcement can be made using 1D channel flow, 2D radial flow or 3D radial flow methods. In this study 1D channel flow method is preferred due to its easy test execution and simple results processing. For the sake of simplicity, isotropic reinforcement materials, which have the equal permeability in the warp and fill directions, are employed.

In numerical simulations, a so-called $2\frac{1}{2}$D modeling technique, which solves the resin flow equations of 3D shell-like structures in 2D, is used and the resin flow in the transverse direction is neglected. Therefore, permeability in the transverse direction is neglected and only one test is conducted per a reinforcement material.

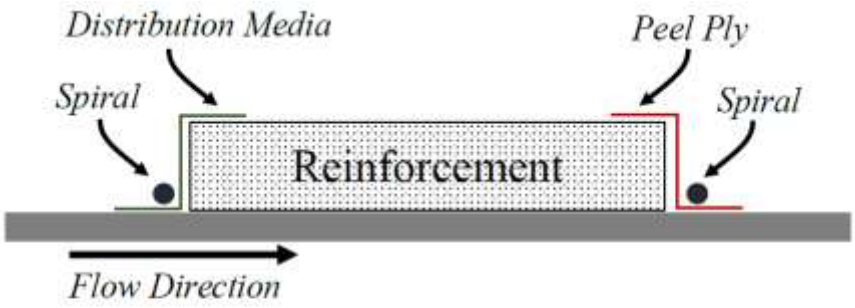

a) Side view of permeability test setup

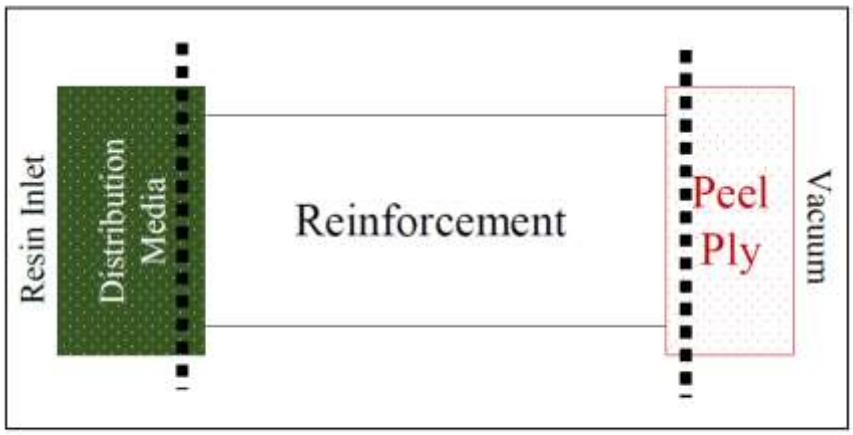

b) Top view of permeability test setup

Figure 38. Permeability Test Set-up a)Side view b) Top view

The test procedure of permeability test starts with preparing the sample reinforcement material. The sample is cut into rectangular pieces and placed on the mold plate. A piece of peel ply is positioned along one edge and a piece of high permeable distribution media is placed on the opposite side. The spiral tubes and resin connectors are positioned. The workpiece is covered by a piece of the vacuum bag and then is sealed off by using sealant tape. Once the vacuum is applied and the air inside is sucked away, the position lines are carefully marked. The test is recorded by a video camera in order to track the flow front. Vacuum pressure is also recorded during the test. Figure 38 presents permeability test set-up, which is identical to that illustrated in Figure 18. The formulation of 1D channel permeability test is stated in Section 2.1.2 and given in Equation (12). Once resin viscosity and reinforcement porosity values are known, permeability can be calculated as a function of time by tracking the flow front. To calculate the average permeability the procedure described in Section 2.1.2 is followed.

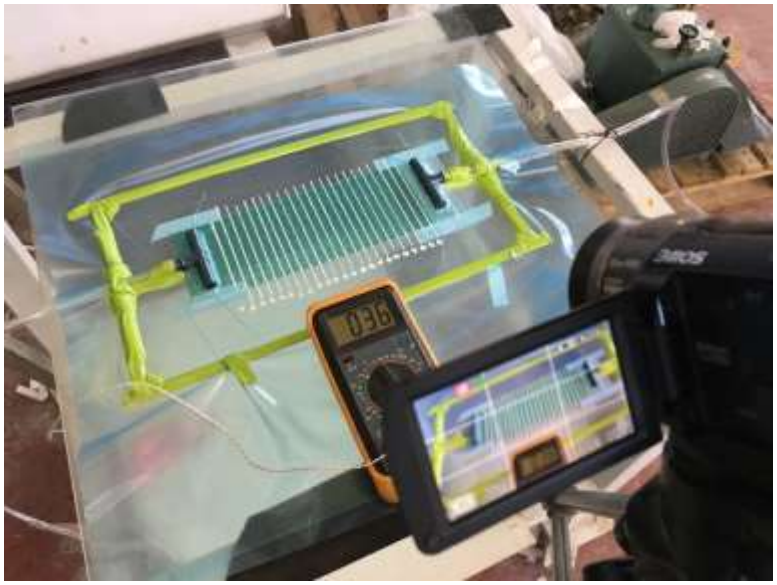

Figure 39. Photography of distribution media permeability test

2.3.4.1. Distribution Media

Distribution media permeability test set-up is shown in Figure 39 and the test properties are given in Table 3.

Table 3. Distribution Media Permeability Test Properties

Test Properties	Value
Resin Temperature (˚C)	36-37
Vacuum Pressure (Pa)	99325
Resin Viscosity (Pa.s)	0.31
Porosity	0.85

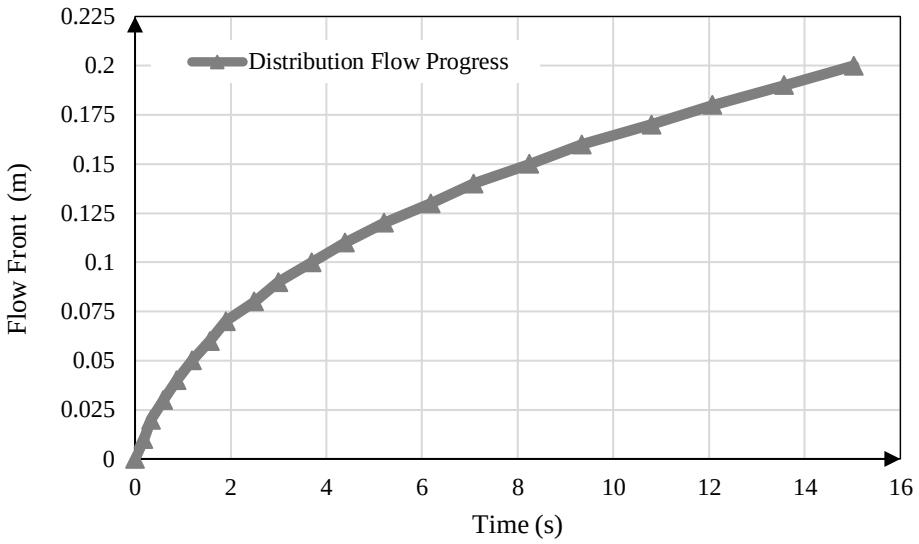

Figure 40. Flow progress in distribution media permeability test

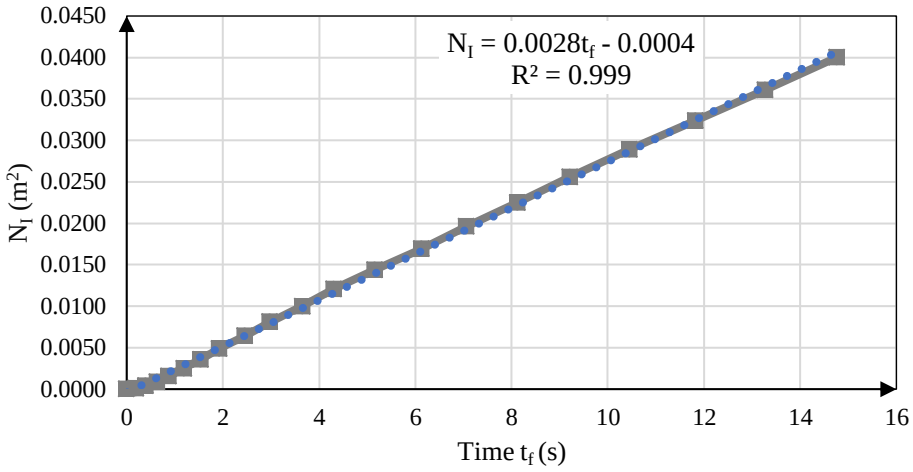

Figure 41. Plot of N_I versus Time

Figure 40 shows the flow progress captured by video camera and the graph of N_I versus time was plotted using these data, i.e. shown in Figure 41. The curve fit equation of N_I vs t_f is given in Equation (35).

$$N_I = 0.0028t_f - 0.0004\,, R^2 = 0.99 \tag{35}$$

Here, the slope of Equation (62) gives the material term, F_I.

$$F_I = 0.0028 \tag{36}$$

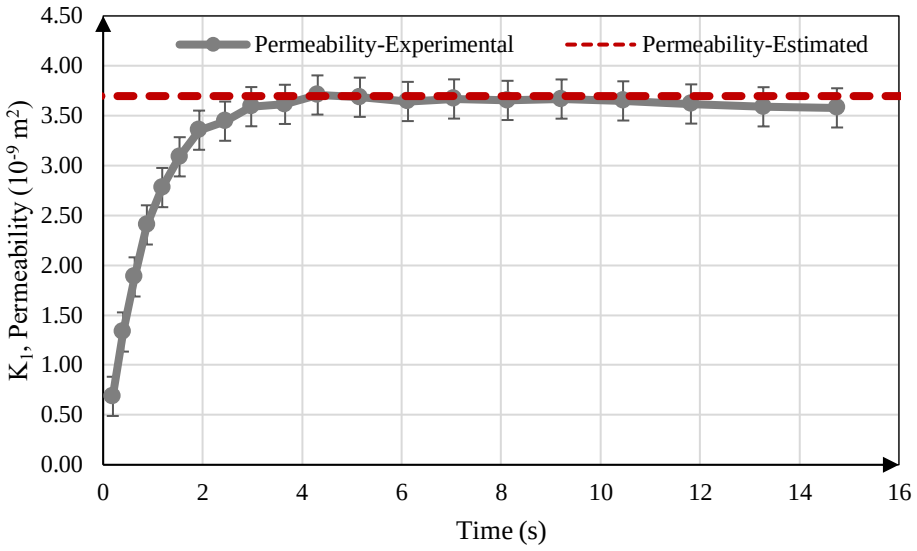

Figure 42. Permeability of distribution media as a function of flow front position

The process term was then evaluated using the experimental data from Table 3.

$$C = \frac{\mu \emptyset}{2\Delta p} = 1.32x10^{-6} \tag{37}$$

Eventually, the permeability for distribution media was calculated as follows.

$$K_I = F_I C = 3.7x10^{-9}\ m^2 \tag{38}$$

2.3.4.2. Peel Ply

The permeability of peel ply was next measured with the test properties given in Table 4.

Table 4. Peel Ply Permeability Test Properties

Test Properties	Value
Resin Temperature (˚C)	54-55
Vacuum Pressure (Pa)	97325
Resin Viscosity (Pa.s)	0.12
Porosity	0.35

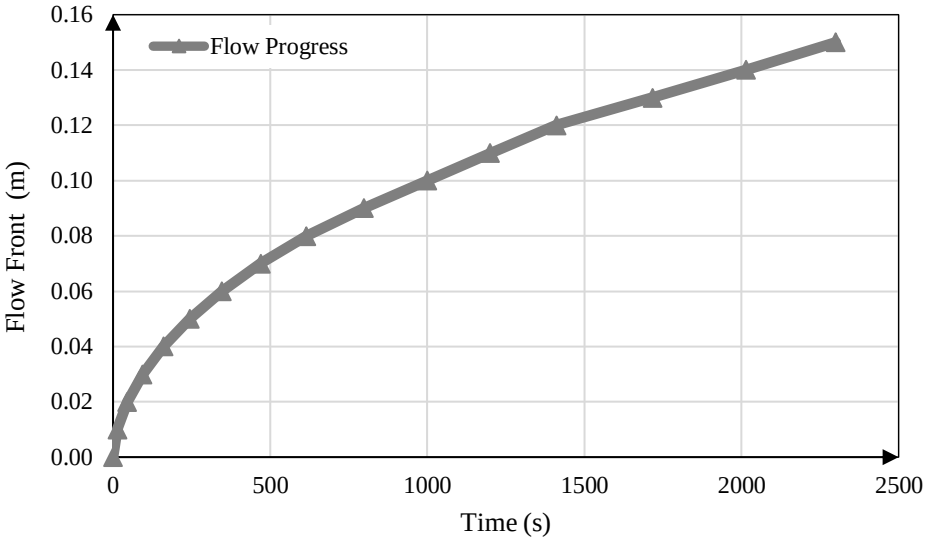

Figure 43. Flow progress in peel ply permeability test

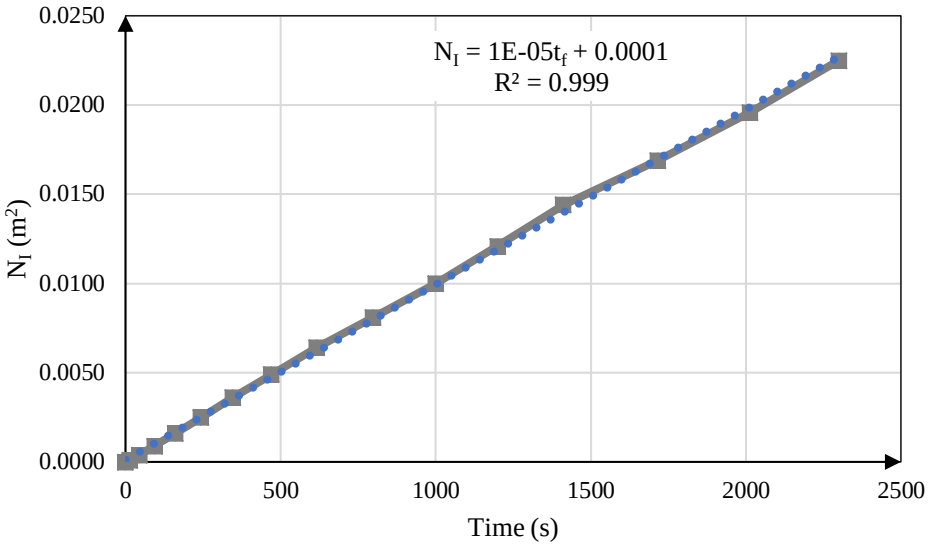

Figure 44. Plot of N_I versus Time

The curve fit equation, which has R^2 value of 0.99, was acquired from Figure 44.

$$N_I = 1x10^{-5}t_f + 0.0001\,, R^2 = 0.99 \tag{39}$$

The material term, F_I was obviously found as such.

$$F_I = 1x10^{-5} \tag{40}$$

Next, the process term was evaluated using the properties in Table 4.

$$C = \frac{\mu \emptyset}{2\Delta p} = 2.16x10^{-7} \tag{41}$$

The permeability of peel ply was eventually calculated as such.

$$K_I = F_I C = 2.16x10^{-12}\ m^2 \tag{42}$$

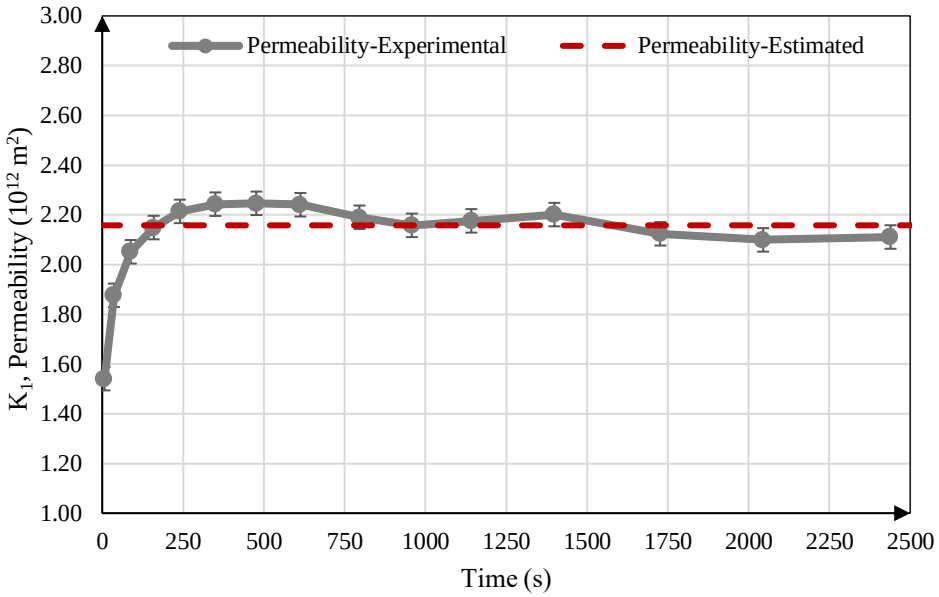

Figure 45. Permeability of distribution media as a function of flow front position

2.3.4.3. Preform

The same procedure was followed for carbon fiber preform permeability test. Test properties are given in Table 5.

Table 5. Carbon Fiber Preform Permeability Test Properties

Test Properties	Value
Resin Temperature (˚C)	36-38
Vacuum Pressure (Pa)	97325
Resin Viscosity (Pa.s)	0.30
Porosity	0.54

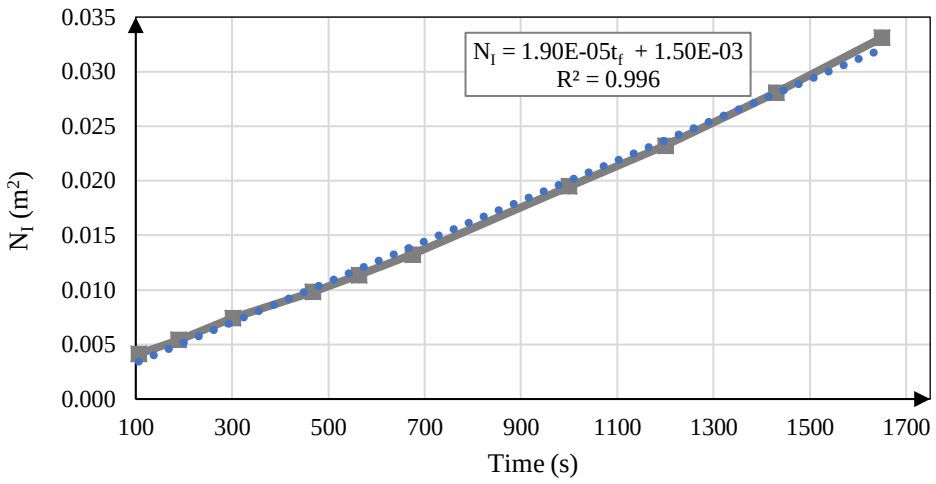

Figure 46. Plot of N_I versus Time

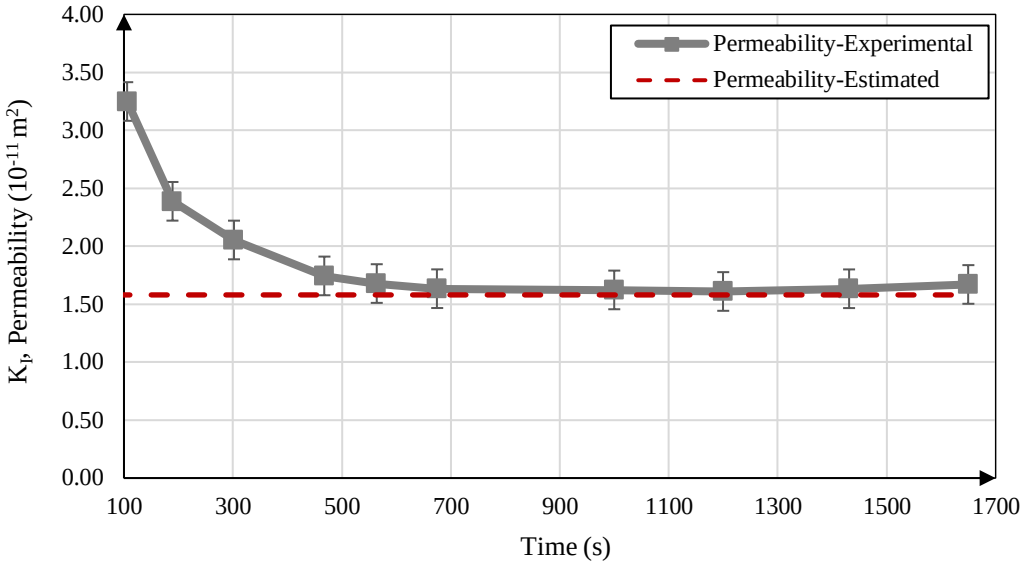

Figure 47. Permeability of carbon fiber preform as a function of flow front position

As shown in Figure 41, the curve fit equation having R^2 value of 0.99 perfectly fits with the curve.

$$N_I = 1.9x10^{-5}t_f + 1.5x10^{-3}\,, R^2 = 0.99 \tag{43}$$

The material term, F_I can be found by taking the derivative of N_I with respect to t_f.

$$F_I = 1.9x10^{-5} \tag{44}$$

Next, the process term was evaluated using the properties in Table 5.

$$C = \frac{\mu\emptyset}{2\Delta p} = 8.32x10^{-7} \tag{45}$$

Finally, the permeability of carbon fiber preform was evaluated as such.

$$K_I = F_I C = 1.58x10^{-11}\ m^2 \tag{46}$$

2.3.4.4. Uncertainty analysis of permeability

The procedure followed for uncertainty analysis is ISO/IEC Guide 98-3:2008 [30], which is a guide to express uncertainty in measurement.

The permeability is a function of five variables, i.e. stated in (62).

$$K\ (\mu, \emptyset, \Delta p, x_f\ , t_f) = \frac{\mu \emptyset}{2\Delta p} \frac{x_f^2}{t_f} \tag{47}$$

The combined standard uncertainty u_c is,

$$u_c = \sqrt{u_r^2 + \sum u_i^2} \tag{48}$$

where u_r is the sum of strongly positive correlated components, i.e. zero in this case and u_i is the standard uncertainty of uncorrelated (independent) contributor i.

$$u_c = \sqrt{\sum \left(\frac{\partial K}{\partial X_i} u_{X_i}\right)^2} \tag{49}$$

More explicitly,

$$u_c = \sqrt{\left(\frac{\partial K}{\partial X_1} u_{X_1}\right)^2 + \left(\frac{\partial K}{\partial X_2} u_{X_2}\right)^2 + \cdots + \left(\frac{\partial K}{\partial X_n} u_{X_n}\right)^2} \tag{50}$$

The measurement uncertainty for the 95% confidence level is calculated as,

$$U_{95\%} = \pm 2\, u_c \tag{51}$$

The uncertainty for permeability can be expressed using (50) as follows.

$$\frac{u_K}{K} = \sqrt{\left(\frac{\partial K}{\partial \mu}\frac{u_\mu}{K}\right)^2 + \left(\frac{\partial K}{\partial \emptyset}\frac{u_\emptyset}{K}\right)^2 + \left(\frac{\partial K}{\partial \Delta p}\frac{u_{\Delta p}}{K}\right)^2 + \left(\frac{\partial K}{\partial\, t_f}\frac{u_{t_f}}{K}\right)^2 + \left(\frac{\partial K}{\partial\, x_f}2\frac{u_{x_f}}{K}\right)^2} \tag{52}$$

Alternatively, Equation (52) can be stated as

$$\left(\frac{u_K}{K}\right)^2 = \left(\frac{u_\mu}{\mu}\right)^2 + \left(\frac{u_\emptyset}{\emptyset}\right)^2 + \left(\frac{u_{\Delta p}}{\Delta p}\right)^2 + \left(\frac{u_{t_f}}{t_f}\right)^2 + \left(2\frac{u_{x_f}}{x_f}\right)^2 \tag{53}$$

Let's investigate the uncertainty components term by term and start with viscosity. There are three sources of uncertainty in viscosity measurement: (1) Uncertainty due to rheometer (2) Uncertainty due to the measurement of resin temperature (3) Temperature change during the process. Uncertainty from rheometer devise is negligible, since the device is periodically calibrated. On the other hand, viscosity depends significantly on temperature and the temperature change is highly effective. For the worst scenario, the temperature change of 2˚C is taken, which was the case in preform permeability test. Equation (23) describes the temperature dependence of viscosity and the parameters for the preform permeability test is used to determine the uncertainty of viscosity. The measurement of resin temperature is made by a calibrated thermocouple that has the uncertainty of ±0.1˚C. Additionally, the uncertainty of temperature measurement is taken into account.

$$\frac{u_\mu}{\mu} = \frac{0.036\ (Pa.s)}{0.30\ (Pa.s)} + \frac{0.003\ (Pa.s)}{0.30\ (Pa.s)} = 13.0\% \tag{54}$$

Next, porosity is investigated, which has the following formulation.

$$\emptyset = 1 - V_f = \frac{W_{sample}}{hA_f\rho_{fabric}} \tag{55}$$

The uncertainty of carbon fiber is assumed to be negligible compared to other uncertainty sources. There are four sources for the uncertainty of porosity: (1) mass measurement (2) width measurement, (3) length measurement and (4) thickness measurement. Precise digital scale, vernier and dial gauge are employed in the physical measurements, which have the uncertainty of ±0.001mg, ±0.1mm and ±0.05 respectively. The error is worst for the distribution media test where the sample is cut into a smaller piece. Thus, the permeability of distribution media is considered.

$$\frac{u_\emptyset}{\emptyset} = \frac{0.001\ (g)}{1.2\ (g)} + \frac{0.1\ (mm)}{100\ (mm)} + \frac{0.1\ (mm)}{500\ (mm)} + \frac{0.05\ (mm)}{1.35\ (mm)} = 3.9\% \tag{56}$$

For the pressure measurement, manometer having uncertainty value of 10mmHg is employed. This yields the following uncertainty for the pressure change.

$$\frac{u_{\Delta p}}{\Delta p} = \frac{10\ (mmHg)}{730\ (mmHg)} = 1.4\% \tag{57}$$

The flow progress is recorded by video camera. The uncertainty of video camera is estimated approximately as 0.5s. Again, the test for distribution media is considered, since its duration time is the smallest (15s).

$$\frac{u_{t_f}}{t_f} = \frac{0.5\ (s)}{15\ (s)} = 3.3\% \tag{58}$$

Last, the uncertainty due to flow front is evaluated. The main source of error in flow front measurement is the thickness of mark line, which is 2mm. The minimum specimen length in permeability test is 500mm, which yields the following uncertainty.

$$\frac{u_{x_f}}{x_f} = \frac{2\ (mm)}{500\ (mm)} = 0.4\% \tag{59}$$

Total uncertainty is then evaluated by substituting the estimated components into Equation(52).

$$\frac{u_K}{K} = \sqrt{(13\%)^2 + (3.9)^2 + (1.4)^2 + (3.3)^2 + (2\ .\ 0.4\%)^2} = 14.1\% \tag{60}$$

Eventually, the uncertainty for 95% confidence level is calculated from Equation (51).

$$U_{95\%} = \pm 2\ u_c = 28.2\% \tag{61}$$

In the light of above analysis, it is concluded that the real permeability values lie with 28.2% of the estimated value because of the measurement uncertainty. It is obvious that the highest contribution comes from the viscosity term. Viscosity is extremely dependent on temperature and even 1˚C temperature change can make a significant difference in viscosity. In the carbon fiber preform test, 2 ˚C temperature difference took place, which was higher compared with the other tests. This raised up the uncertainty value so that if the other measurement was considered, the uncertainty value would be decreased by almost 50%. Therefore, if one aims to reduce the uncertainty of the aforementioned permeability test method, the temperature should be precisely controlled during the test.

2.4. CHARACTERIZATION TEST RESULTS

In this study both resin and preform characterization tests are performed and the results are stated in Table 6 and Table 7.

Table 6. Resin characterization test results

	Test Name	Equation
Neat Resin	Shear Rate Dependence	$\tau = 0.756\dot{\gamma} + 0.201$
	Temperature Dependence	$\mu = 488235T^{-3.641}$
Resin with catalyst (Effect of curing)	Non-isothermal Model (Power Law)	$\mu = 819.34T^{-2.191}$
	Non-isothermal Model (Exponential Model)	$\mu = 1.5549e^{-0.045T}$
	Non-isothermal Model (Arrhenius Model)	$\mu = 7.431x10^{-8}e^{4731.8\left(\frac{1}{T}\right)}$
	Isothermal Cure-dependent Model (Exponential Model)	$\mu = 0.1669e^{1.6102\alpha}$
	Non-isothermal Cure-dependent Model (Castro-Macosko Model)	$\mu = 7.431x10^{-8}e^{4731.8\left(\frac{1}{T}\right)}\left(\frac{\alpha_{gel}}{\alpha_{gel}-\alpha}\right)^{-11.133+83.648\alpha}$
	Non-isothermal Cure-dependent Model (Lee-Han Model)	$\mu = 7.431x10^{-8}e^{4731.8\left(\frac{1}{T}\right)}e^{(-0.479+\frac{1.432}{T})\alpha}$

Table 7. Preform characterization test results

	Property	Distribution Media	Peel Ply	Carbon Fiber Preform
	Fabric Thickness (mm)	1.35	0.2	0.3
	Fabric Warp Direction (˚)	0˚	0˚	0˚
Porosity	Uncompressed porosity	0.88	0.65	0.63
	Porosity under full vacuum	0.85	0.35	0.54
Permeability	Mean value of results	3.24×10^{-9}	2.14×10^{-12}	1.80×10^{-11}
	Estimated Permeability, K_{11}, K_{22} (m^2)	3.70×10^{-9}	2.16×10^{-12}	1.58×10^{-11}
	Coefficient of determination, R^2	0.99	0.99	0.99
	Deviation (%)	12%	0.9%	12%

CHAPTER 3

ANALYTICAL MODELING OF THE VARTM PROCESS

In this chapter, 1D resin impregnation model of the VARTM process is presented. The purpose of the current study is to investigate the effects of varying thickness and pressure profile in VARTM on fill-time solutions, which are not considered in the RTM-Worx simulations. Compacting models, permeability models and the laminate thickness relation are introduced in the first section. Then, the coupled compaction pressure and resin flow model is constructed. Having established the coupled pressure formulation, the fill-time formulations are derived. In the end of the chapter, fill-time formulations are solved numerically and the effect of nonuniformity in thickness and pressure is discussed based on the numerical results.

3.1. INTRODUCTION

3.1.1. Compaction Modelling

Few models for the compaction of fiber preforms have been developed so far. Chen et al., [31], [32] studied on analytical models by considering single and multiple layers of woven fabrics. The models claimed by Gutowski et al., [33], [34] are nevertheless easier to work in parametric studies.

In another approach Robitaille, [35], [36], [37] , used an empirical law fit to relate compaction pressure to fiber volume fraction, which is as follows.

$$\nu_f = \nu_{fo} P_{comp}^{B} \tag{62}$$

where ν_{fo} is the fiber volume fraction under no compaction and B is a stiffening index, which depends on fiber architecture. We prefer the Power Law in this study, since it is a simple model and easy to implement to experimental data.

3.1.2. Laminate Thickness Prediction

The relation between the laminate thickness and compaction pressure can be obtained from Equation (62).

$$h(P_{comp}) = \frac{\rho_{sup}}{\rho}\frac{1}{\nu_f} = \frac{\rho_{sup}}{\rho}\frac{1}{\nu_{fo} P_{comp}^{B}} \tag{63}$$

Pressure derivative of the laminate thickness is as such.

$$\frac{\partial h}{\partial P_{comp}} = \frac{-\rho_{sup}}{\rho}\frac{B}{\nu_{fo}} P_{comp}^{-(B+1)} \tag{64}$$

3.1.3. Permeability Modelling

Josef Kozeny was originally proposed the permeability model for flow through an array of channels having varying cross-sections in 1927. The model was later modified by Philip C. Carman and reached its final form, which is also known as Carmon-Kozeny Model, in 1956, which is shown as follows [38].

$$K = k_0 \frac{(1-\nu_f)^3}{{\nu_f}^2} \tag{65}$$

where k is a constant. The main drawback of this model is that it finds transverse permeability greater than zero at fiber volume fraction that hinders transverse flow for unidirectional reinforcements. Gutowski et al. [34] proposed a modified model i.e. seen below.

$$K = k' \frac{\left(\sqrt{\frac{\nu_{fa}}{\nu_f}} - 1\right)^3}{\left(\sqrt{\frac{\nu_{fa}}{\nu_f}} + 1\right)} \tag{66}$$

Here k' is a constant and ν_{fa} is a theoretical maximum fiber volume fraction, which is different than 1 at lower values. Gebart presented a model by considering the dependence of permeability on the orientation [39].

$$K_1 = k_0 \frac{(1-\nu_f)^3}{{\nu_f}^2} \quad and \quad K_2 = C_2 \left(\sqrt{\frac{\nu_{fa}}{\nu_f}} - 1\right)^{\frac{5}{2}} \tag{67}$$

Since Carman-Kozeny Model is a very simple owing to its one-dimensional nature, it is extensively used, though many other models have been developed over time. It is important to note that permeability is a function of fiber volume fraction.

3.2. COUPLED COMPACTION PRESSURE AND RESIN FLOW MODELLING IN VARTM

As discussed in Chapter 1, VARTM process employs one-sided rigid mold and flexible tooling instead of two-sided rigid mold used in RTM. The use of flexible tooling, vacuum bag, results in the varying pressure profile inside the mold cavity, which in turn causes varying part thickness. The schematic of the part thickness variation is shown in Figure 48. Thus, the compaction behavior of fiber preform needs to be taken into account in the resin flow (impregnation) model of VARTM process.

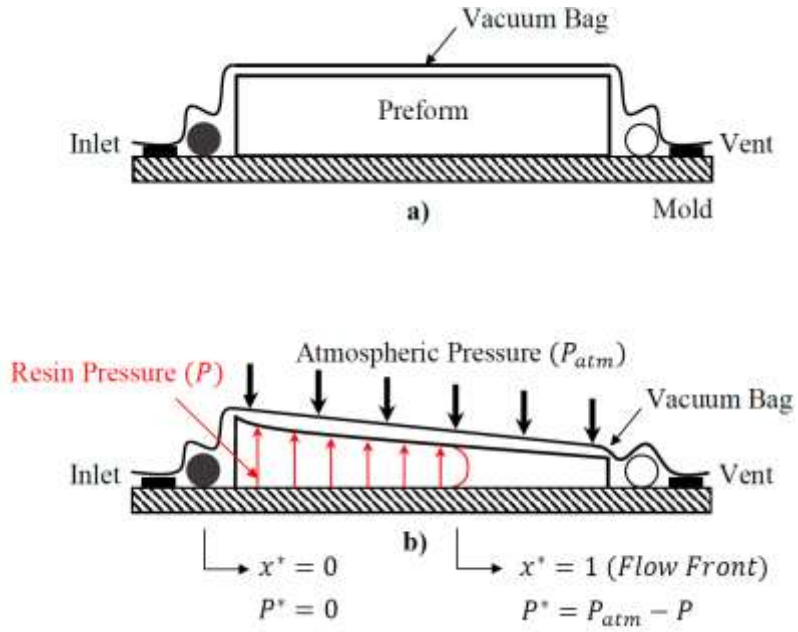

Figure 48. Variation of part thickness and pressure profile in the VARTM process a) before resin injection and b) during resin injection

Hammami and Gebart [40] modified the continuity equation to take into consideration the variation in thickness in VARTM process. Figure 49 illustrates the 1D resin flow along x direction where control volume that is defined over thickness h. The modified continuity equation derived by Hammami and Gebart is as follows.

$$\frac{\partial h}{\partial t} = -\frac{\partial (u.h)}{\partial x} \tag{68}$$

Equation (68) was also derived by Gutowski et al. [34].

Superficial velocity is given by Darcy Law,

$$u = -\frac{K}{\mu}\frac{\partial P}{\partial x} \tag{69}$$

Substitute the Darcy law (Equation (69)) into the governing equation (Equation (68)),

$$\frac{\partial h}{\partial t} = -\frac{\partial}{\partial x}\left[-\frac{hK}{\mu}\frac{\partial P}{\partial x}\right] \tag{70}$$

Since permeability and viscosity are taken as constant,

$$\frac{\partial h}{\partial t} = \frac{K}{\mu}\frac{\partial}{\partial x}\left[h\frac{\partial P}{\partial x}\right] \tag{71}$$

Further the solution by taking the derivative,

$$\frac{\partial h}{\partial t} = \frac{K}{\mu}\frac{\partial}{\partial x}\left[\frac{\partial h}{\partial x}\frac{\partial P}{\partial x} + h\frac{\partial^2 h}{\partial x^2}\right] \tag{72}$$

Simplifying the equation,

$$\frac{\partial h}{\partial t} = \frac{K}{\mu}\left[h\frac{\partial^2 P}{\partial x^2} + \frac{\partial h}{\partial x}\frac{\partial P}{\partial x}\right] \tag{73}$$

In VARTM process, the compaction pressure is not constant, instead, it changes locally with respect to the resin pressure. The compaction pressure is thus as follows.

$$P_{comp} = P_{atm} - P \tag{74}$$

At this point, it would be clarifying to normalize x and P and with $x^*$and P^*.

$$P^* = P_{comp} = P_{atm} - P \tag{75}$$

$$\frac{\partial P^*}{\partial P} = -1 \tag{76}$$

$$x^* = \frac{x}{x_f}\ ;\ \frac{\partial x^*}{\partial x} = \frac{1}{x_f}\ ;\ \frac{\partial x^*}{\partial x_f} = -\frac{x}{{x_f}^2} = -\frac{x^*}{x_f} \tag{77}$$

Note that $x^* = 0$ refers the inlet position, whereas $x^* = 1$ designates the flow front position.

Also,

$$\frac{\partial P}{\partial x} = -\frac{\partial P^*}{\partial x} = -\frac{\partial P^*}{\partial x^*}\frac{\partial x^*}{\partial x} = -\frac{1}{x_f}\frac{\partial P^*}{\partial x^*}; \tag{78}$$

and,

$$\frac{\partial h}{\partial x} = \frac{\partial h}{\partial P^*}\frac{\partial P^*}{\partial x^*}\frac{\partial x^*}{\partial x} = \frac{1}{x_f}\frac{\partial h}{\partial P^*}\frac{\partial P^*}{\partial x^*}; \tag{79}$$

Let's investigate the LHS term $\frac{\partial h}{\partial t}$, which is also called as Expansion rate differential first. Expansion rate differential, $h\,(x^*(x_f(t)))$, is a composite function of x^*, x_f, and t.

$$\frac{\partial h}{\partial t} = \frac{\partial h}{\partial x^*}\frac{\partial x^*}{\partial x_f}\frac{\partial x_f}{\partial t} = -\frac{x^*}{x_f}\frac{\partial h}{\partial x^*}\frac{\partial x_f}{\partial t} \tag{80}$$

Here we need to find the term $\frac{\partial x_f}{\partial t}$ to further the derivation. Correia et al. [41] assumed that the flow rate remains constant in the VARTM process. However, Modi et al. [42] argued that flow rate changes dynamically due to the dynamically changing preform thickness. Thus, the assumption of constant flow rate is not valid for VARTM, even though it is applicable to RTM. This is illustrated in Figure 49.

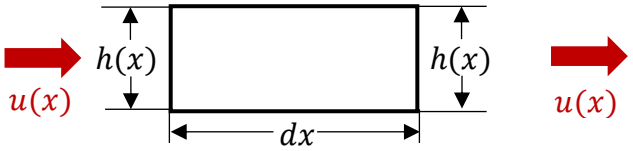

Constant Thickness
Constant Flow Rate

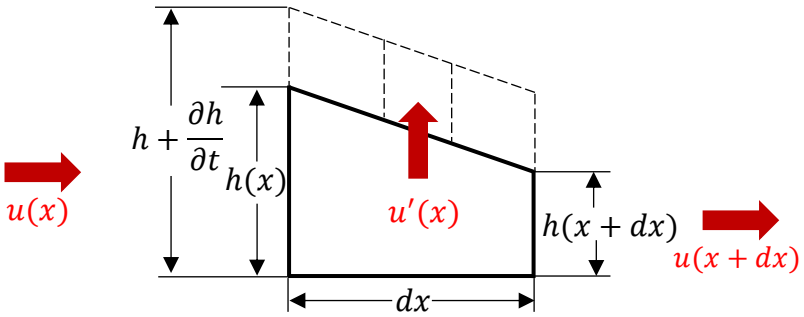

Varying Thickness
Varying Flow Rate

Figure 49. Conservation of Mass in the RTM and VARTM

Writing the Darcy's Law for Flow front velocity,

$$u_f = \frac{\partial x_f}{\partial t} = -\frac{K}{\mu \emptyset}\frac{\partial P}{\partial x_f} \tag{81}$$

Substitute Equation (75) and Equation (77) into Equation (81),

$$u_f = \frac{\partial x_f}{\partial t} = -\frac{K}{\mu \emptyset}\frac{\partial P}{\partial x^*}\frac{\partial x^*}{\partial x_f} = \frac{-Kx^*}{\mu \emptyset x_f}\frac{\partial P^*}{\partial x^*} \tag{82}$$

Thus, substitute Equation (82) into Equation (80) in order to write the LHS or expansion rate differential.

$$\frac{\partial h}{\partial t} = \frac{Kx^{*2}}{\mu \emptyset {x_f}^2}\frac{\partial P^*}{\partial x^*}\frac{\partial h}{\partial x^*} \tag{83}$$

Hence, the term $\frac{\partial h}{\partial t}$ becomes as follows, which is the LHS of (73).

$$\frac{\partial h}{\partial t} = \frac{Kx^{*2}}{\mu \emptyset {x_f}^2}\frac{\partial h}{\partial P^*}\left(\frac{\partial P^*}{\partial x^*}\right)^2 \tag{84}$$

Now consider the RHS of Equation (73), normalize the terms x and P

$$\frac{Kh}{\mu}\left[\frac{\partial^2 P}{\partial x^2} + \frac{1}{h}\frac{\partial h}{\partial x}\frac{\partial P}{\partial x}\right] = \frac{-Kh}{\mu}\left[\frac{1}{{x_f}^2}\frac{\partial^2 P^*}{\partial {x^*}^2} + \frac{1}{h}\frac{1}{x_f}\frac{\partial h}{\partial P^*}\frac{\partial P^*}{\partial x^*}\left(\frac{1}{x_f}\frac{\partial P^*}{\partial x}\right)\right] \tag{85}$$

By substituting Equation (84) and Equation (85) into Equation (73), we can eventually convert the Equation (73) to Equation (86).

$$\frac{d^2 P^*}{d x^{*2}} + \left(\frac{\emptyset + x^{*2}}{h\emptyset}\right)\frac{d h}{d P^*}\left(\frac{dP^*}{dx^*}\right)^2 = 0 \tag{86}$$

This is a 2nd order Ordinary Differential Equation with an independent variable of x^*, which was first developed by Modi et al. [42]. Here laminate thickness h and $\frac{\partial h}{\partial P^*}$ are functions of P^*, therefore we are able to obtain the pressure field by solving these equations. Note that, the beauty of Equation (86) is that Equation (73), i.e is a PDE, is transformed into a non-linear 2nd order ODE.

Eventually, the following equation set is obtained:

Table 8. Coupled Equation Set

Name	Equation	
Compaction Model	$v_f = v_{fo} P_{comp}^B$	(62)
Laminate Thickness	$h(P_{comp}) = \frac{\rho_{sup}}{\rho}\frac{1}{v_f} = \frac{\rho_{sup}}{\rho}\frac{1}{v_{fo} P_{comp}^B}$	(63)
Pressure Derivative of Thickness	$\frac{\partial h}{\partial P_{comp}} = \frac{-\rho_{sup}}{\rho}\frac{B}{v_{fo}} P_{comp}^{-(B+1)}$	(64)
Pressure Formulation	$\frac{d^2 P^*}{d x^{*2}} + \left(\frac{\emptyset + x^{*2}}{h\emptyset}\right)\frac{d h}{d P^*}\left(\frac{dP^*}{dx^*}\right)^2 = 0$	(86)

3.3. FILL-TIME FORMULATION

3.3.1. Uncoupled Formulation

As presented in Figure 49, thickness and flow rate are assumed to be constant in the uncoupled formulation, which yields pressure field that is a linear function of position. In Section 2.1.2, the uncoupled formulation was derived for the 1D channel permeability test and was given in Equation (11).

$$\int_{x_f=0}^{x_f} \frac{\emptyset x_f}{K\Delta p}\partial x_f = \int_{t=0}^{t=t_f} \frac{\partial t}{\mu} \tag{11}$$

For a constant viscosity, uncoupled fill-time formulation is as follows.

$$t_f = \frac{\mu\emptyset L^2}{2K\Delta p} \tag{87}$$

If the isothermal time-dependent model is used and the viscosity is a function of time, right-hand side of Equation (11) yields,

$$\mu = \mu_0 e^{B_\mu t} \tag{88}$$

$$\int_{t=0}^{t=t_f} \frac{\partial t}{\mu_0 e^{B_\mu t}} = \frac{1}{\mu_0 B_\mu} - \frac{1}{\mu_0 B_\mu e^{B_\mu t}} \tag{89}$$

Uncoupled fill time formulation is then found as such.

$$t_f = \frac{1}{B_\mu} ln\left\{\frac{1}{1 - \frac{\mu_0 B_\mu \emptyset L^2}{2K\Delta p}}\right\} \tag{90}$$

3.3.2. Coupled Formulation

Darcy's Law for flow front velocity is written as,

$$u_f = \frac{\partial x_f}{\partial t} = -\left[\frac{K}{\mu \emptyset x_f}\frac{\partial P}{\partial x^*}\right]_{x^*=1} = \left[\frac{K}{\mu \emptyset x_f}\frac{\partial P^*}{\partial x^*}\right]_{x^*=1} \tag{91}$$

Assuming that the permeability remains unchanged, flow front velocity can be rewritten as in Equation (92).

$$u_f = \frac{\partial x_f}{\partial t} = K\left[\frac{1}{\mu \emptyset}\frac{\partial P^*}{\partial x^*}\right]_{x^*=1} \tag{92}$$

For a isothermal time-dependent viscosity model, the equation becomes as follows.

$$u_f = \frac{\partial x_f}{\partial t} = \frac{K}{\mu(t)}\left[\frac{1}{\emptyset}\frac{\partial P^*}{\partial x^*}\right]_{x^*=1} \tag{93}$$

Integrating Equation (93) yields the fill-time,

$$\int_{x_f=0}^{x_f=L} \frac{x_f \partial x_f}{K\left[\frac{1}{\emptyset}\frac{\partial P^*}{\partial x^*}\right]_{x^*=1}} = \int_{t=0}^{t=t_f} \frac{\partial t}{\mu(t)} \tag{94}$$

If the viscosity is constant, fill-time is found as follows.

$$t_f = \frac{\mu L^2}{2K}\frac{1}{\left[\frac{1}{\emptyset}\frac{\partial P^*}{\partial x^*}\right]_{x^*=1}} \tag{95}$$

If the isothermal time-dependent model is employed, i.e. in Equation (88), right-hand side of Equation (94) becomes as such.

$$\int_{t=0}^{t=t_f} \frac{\partial t}{\mu_0 e^{B_\mu t}} = \frac{1}{\mu_0 B_\mu} - \frac{1}{\mu_0 B_\mu e^{B_\mu t}} \tag{96}$$

Eventually, coupled solution of fill time is evaluated as follows.

$$t_f = \frac{1}{B_\mu} ln \left\{ \frac{1}{1 - \frac{\mu_0 B_\mu L^2}{2K \left[\frac{1}{\emptyset} \frac{\partial P^*}{\partial x^*}\right]_{x^*=1}}} \right\} \tag{97}$$

3.3.3. Summary of Fill-Time Formulations

A summary of coupled and uncoupled fill-time formulations is stated in Table 9.

Table 9. Summary of Fill-time Formulations

Viscosity Model	Uncoupled Formulation	Coupled Formulation
Constant	$t_f = \frac{\mu \emptyset L^2}{2K\Delta p}$	$t_f = \frac{\mu L^2}{2K} \frac{1}{\left[\frac{1}{\emptyset} \frac{\partial P^*}{\partial x^*}\right]_{x^*=1}}$
Isothermal Time-dependent	$t_f = \frac{1}{B_\mu} ln \left\{ \frac{1}{1 - \frac{\mu_0 B_\mu \emptyset L^2}{2K\Delta p}} \right\}$	$t_f = \frac{1}{B_\mu} ln \left\{ \frac{1}{1 - \frac{\mu_0 B_\mu L^2}{2K \left[\frac{1}{\emptyset} \frac{\partial P^*}{\partial x^*}\right]_{x^*=1}}} \right\}$

3.4. NUMERICAL SOLUTION PROCEDURE

The derived pressure formulation, Equation (86) is a 2nd order ODE and basically a non-linear boundary value problem. The solution of such non-linear boundary value problem can be found using finite difference method utilizing Newton's linearization method, as in [41].

One can also solve this problem by using the shooting method, which transforms a boundary value problem into two initial value problems.

The derived pressure formulation is,

$$\frac{\partial^2 P^*}{\partial x^{*2}} + \left(\frac{\emptyset + x^{*2}}{h\emptyset}\right)\frac{\partial h}{\partial P^*}\left(\frac{\partial P^*}{\partial x^*}\right)^2 = 0 \tag{88}$$

This can be converted into two initial value problems by using the shooting method.

$$\frac{\partial \mathrm{I}}{\partial x^*} + \left(\frac{\emptyset + x^{*2}}{h\emptyset}\right)\frac{\partial h}{\partial P^*}(\mathrm{I})^2 = 0 \tag{98}$$

$$\frac{\partial P^*}{\partial x^*} = I \tag{99}$$

In [42], first-order Euler Method and fourth-order Runge-Kutta Methods are employed to solve Equation (98) and Equation (99) and a comparison between two methods is made. No significant difference was reported between two methods and thus first-order Euler Method is used in this study.

Equation (98) and Equation (99) are discretized by using first-order Euler Method. The physical domain is discretized into m number of nodes.

$$\frac{I_i - I_{i-1}}{x^*_i - x^*_{i-1}} + \left[\left(\frac{\emptyset + x^{*2}}{h\emptyset}\right)\frac{\partial h}{\partial P^*}\right]_{i-1} (\mathrm{I}^2)_{i-1} = 0; \quad i = 2, 3, \dots, m \tag{100}$$

$$P^*_i = P^*_{i-1} + I_{i-1}(x^*_i - x^*_{i-1}); \quad i = 2, 3, \dots, m \tag{101}$$

The domain is divided into equally spaced nodes within the interval and the initial values are imposed. In this case, the pressure in injection gate, i.e. the first node, is imposed to be injection pressure. Also, pressure gradient at the first node is guessed. The initial guess value determines the speed of convergence. The coupled equations, Equation (62), (63), (64), and (86), are then solved simultaneously for all other nodes within the domain to find the pressure field at the last node. At this point, the convergence criterion is to make resin pressure at the last node equal to the vacuum pressure, which is zero in this case. If this is not satisfied, the iterative procedure is repeated to achieve this requirement.

A root finding method is required to implement for optimizing guessed values. The bisection method is employed in [42], which repeatedly bisects an interval and pics a subinterval to find the root value. The bisection method is a simple and robust method; however, it is a highly slow technique and typically uses for rough approximations. Another technique is Newton's Method, also known as Newton-Raphson Method. Newton's Method is a costly technique due to the presence of the derivative term in its formulation. One can also use the Secant Method to better guess these values. The advantage of Secant Method is that it replaces the derivative term with a finite difference. Thus, Secant Method needs lower computational load compared to Newton's Method. Secant Method is preferred in this study. An Octave code is given in Appendix A to evaluate the fill time solutions of all formulations stated in Table 9.

The algorithm of the numerical solution is as follows:

Step 1. Divide the physical domain into equally spaced nodes.

$$dx^* = \frac{1}{\mathrm{N}_{nodes}} \tag{102}$$

Step 2. Set the initial and guess values. Make two guesses for the first node of $\frac{\partial P^*}{\partial x^*}$.

$$P^*_{i=1} = P_{atm} \tag{103}$$

$$\left(\frac{\partial P^*}{\partial x^*}\right)_{i=1} = I_A \tag{104}$$

$$\left(\frac{\partial P^*}{\partial x^*}\right)_{i=1} = I_B \tag{105}$$

Step 3. Solve $\frac{\partial P^*}{\partial x^*}$ two times: One uses the initial guess value of I_A and the other I_B.

$$\left(\frac{\partial P^*}{\partial x^*}\right)_i = \left(\frac{\partial P^*}{\partial x^*}\right)_{i-1} - dx^* \left[\left(\frac{\emptyset + x^{*2}}{h\emptyset}\right)\frac{\partial\, h}{\partial\, P^*}\right]_{i-1} \left(\frac{\partial P^{*2}}{\partial x^*}\right)_{i-1};\ \ i = 2,3,\dots,m \tag{107}$$

$$x^*_i = (i-1)\, dx^*;\ \ i = 2,3,\dots,m \tag{106}$$

Step 4. Compute P^* two times for I_A and I_B cases.

$$P^*_i = P^*_{i-1} + \left(\frac{\partial P^*}{\partial x^*}\right)_{i-1} (x^*_i - x^*_{i-1});\quad i = 2,3,\dots,m \tag{107}$$

Step 5. Check the convergence criterion. If the requirement is satisfied, stop the iteration.

$$I_I = I_B - (P_m^*)_B \frac{I_B - I_A}{(P_m^*)_B - (P_m^*)_A} \tag{108}$$

$$\frac{|I_I - I_B|}{I_B} < tolerance \tag{109}$$

Step 6. If convergence is not satisfied, change the guessed values as below and repeat Steps 2-5.

$$I_A = I_B \tag{110}$$

$$I_B = I_I \tag{111}$$

Step 7. Evaluate fill-time using Equation (97).

$$t_f = \frac{1}{B_\mu} ln \left\{ \frac{1}{1 - \frac{\mu_0 B_\mu L^2}{2K \left[\frac{1}{\emptyset} \frac{\partial P^*}{\partial x^*} \right]_{i^*=m}}} \right\} \tag{104}$$

3.5. FILL-TIME SOLUTION RESULTS

In this Section, comparison among fill-time formulations is made for the experiment stated in Section 4.3.2. The derived equations are given in Table 9 and the numerical solution procedure is explained in Section 3.4. GNU Octave is an open-source programming language for scientific computation and is a free alternative to MATLAB. Hence, GNU Octave is preferred to solve this problem. The code is given in Appendix A.

Table 10. Fill-time simulation parameters

Resin Inlet Temperature	35 ˚C
Resin Viscosity (at 35 ˚C)	0.34 Pa.s
Isothermal time-dependent resin viscosity (at 35 ˚C)	$\mu = 0.34e^{0.00034t}$
Pressure Difference	97325 Pa

The numerical solution parameters are given in Table 10. As the resin temperature in the experiment is averaged as 35 ˚C and the related viscosity is evaluated from the constructed viscosity model Equation (23). The time hold test was not conducted at 35 ˚C. Thus, the viscosity constant of the isothermal model μ_0 is set equal to the isothermal value and exponent constant B_μ, is acquired from Equation (31).

Figure 59 shows the fill-time results of numerical solutions. The actual fill-time was measured 1056s in the experiment and the fill-time errors are calculated by using this value.

The first conclusion is that uncoupled models give just 3% more fill-time error compared to coupled models. This is a significant outcome since the algorithm of RTM-Worx is based on the uncoupled formulation. Hence, it is concluded that RTM-Worx does not make substantial fill-time error by implementing the uncoupled formulation and it can be used in the three-cell box beam simulations.

Another conclusion is that selecting the proper resin viscosity model is more effective on the accuracy of fill-time solution than implementing a coupled formulation. Resin viscosity models are dominant in the accuracy of fill-time results. Therefore, more attention needs to be paid to find the suitable resin viscosity model in resin impregnation simulations.

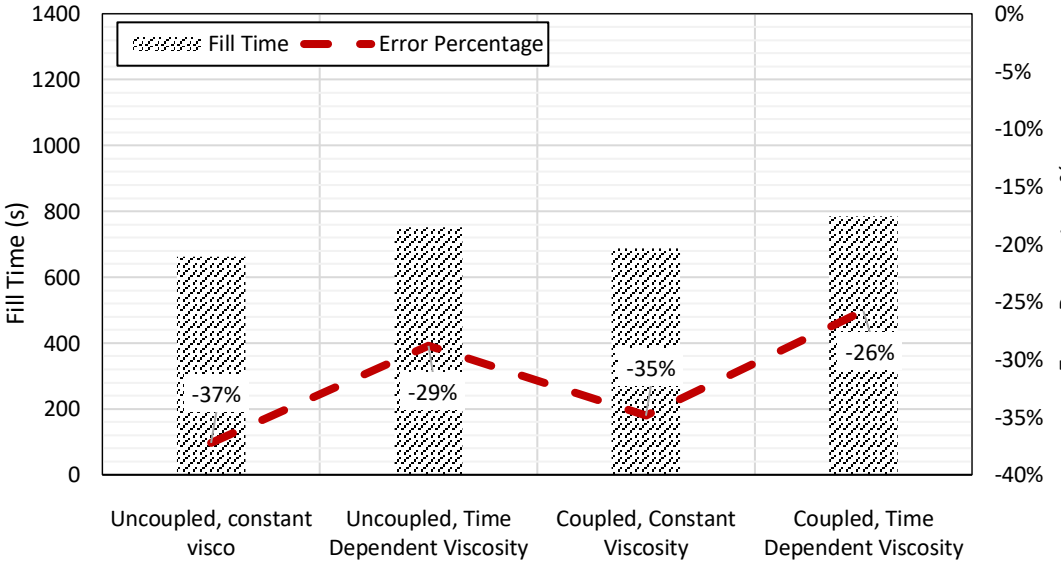

Figure 50. Comparison of fill-time formulations

CHAPTER 4

SIMULATION OF THE VARTM PROCESS USING RTM-WORX

The effect of thickness and pressure nonuniformity on fill-time is discussed in Chapter 3. Having concluded in the previous chapter that RTM-Worx is suitable to use, resin impregnation simulations of the VARTM process are performed using RTM-Worx in this chapter. The aim of this chapter is to find the most accurate resin viscosity and simulation models. In the first section of the chapter, mathematical background of RTM-Worx flow simulation software is introduced. RTM-Worx is originally intended to solve resin impregnation in RTM process. Therefore, the software makes the following assumptions that are valid for RTM, but not for VARTM:

- Neglects the variation in the part thickness
- Ignores the change in the pressure profile throughout the body
- Neglects the porosity change due to the non-uniform pressure distribution

Second section in this chapter presents the procedure of constructing the finite element model in RTM-Worx Software. In the last section, RTM-Worx simulations are performed using different simulation models. Actual VARTM experiment is carried out to validate the simulation result. The experimental and numerical results are compared to find the most accurate simulation model. Additionally, RTM-Worx solutions are compared with that found in Chapter 3 to investigate the effects of varying thickness and pressure profile in VARTM.

4.1. MATHEMATICAL BACKGROUND

The general form of Darcy Law is,

$$\boldsymbol{u} = -\frac{\boldsymbol{K}}{\mu}(\nabla \boldsymbol{P} - \rho \boldsymbol{g}) \tag{69}$$

Where u is superficial velocity vector, K is permeability tensor, P is resin pressure vector, μ is the resin viscosity and $\boldsymbol{g}$ is the gravity vector.

The continuity equation in generalized form is as below.

$$\nabla . \boldsymbol{u} = 0 \tag{112}$$

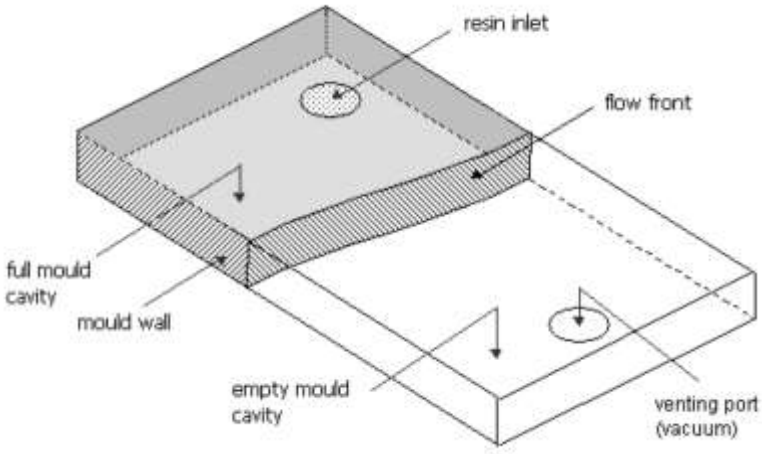

Figure 51. Mold cavity as resin propagates [43]

Inserting Darcy's Law into the continuity equation, the new equation becomes as such,

$$\nabla . \left(\frac{\boldsymbol{K}}{\mu}(\nabla \boldsymbol{P} - \rho \boldsymbol{g}) \right) = 0 \tag{113}$$

Equation (113) is a 2nd order partial differential equation with the unknown of pressure. So, one needs to have proper boundary conditions to solve this equation. Assuming a mold configuration where the pressure is constant and a single injection and venting scheme is implemented, different regions form in the mold cavity, i.e. stated in Figure 51.

The boundary conditions of the related mold configuration can be written as below.

1. Constant pressure at the resin inlet, $P = 0$
2. Constant pressure at the flow front, $P = P_{atm}$ (114)
3. No flow through mold walls, $\boldsymbol{v}.\boldsymbol{n} = 0$, where $\boldsymbol{n}$ is the normal vector to the mold wall. (115)

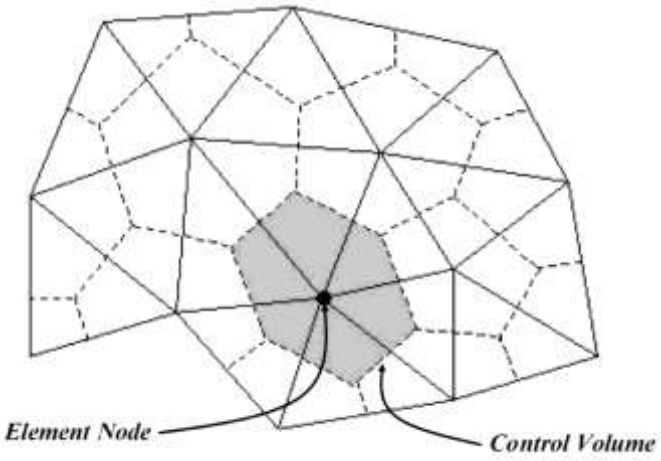

Figure 52. Discretization of physical domain in RTM-Worx using triangular elements [43]

RTM-Worx employs Finite Element formulation using linear elements to solve the Equation (113). The software uses three types of linear elements: (1)3D tetrahedron (2)2D triangle (shell elements with constant thickness) (3)1D beam. Figure 52 represents the discretization of the physical domain by using 2D triangular elements.

The resin flow or mold filling process is a transient problem so that unwetted regions exist as resin propagates. To distinguish the unwetted and wetted regions and define the filling state, a control volume is formed all around all nodes. Basically, there are three states of control volumes: (1) empty, (2) partly filled and (3) fully filled.

Fill factor can be stated as below.

$$Fill\ factor\ f = \begin{cases} 0, & if\ the\ node\ is\ empty \\ 0 < f < 1, & if\ the\ node\ is\ partly\ filled \\ 1, & if\ the\ node\ is\ filled \end{cases} \tag{116}$$

The pressure of element is calculated as a linear combination of the basis function.

$$P^e = \sum_{i=1}^{N} w_i P_i \tag{117}$$

Here w_i linear weighting functions and P_i is the pressure values of a node. Many approximations exist for weighting function, but one common method is Galerkin approximation, which is used in the algorithm of RTM-Worx.

By applying Galerkin Finite Element formulation, Equation (117) becomes as such,

$$A^e P^e = f^e + b^e \tag{118}$$

Where

$$A^e = \int_{\Omega^e} \nabla w . \frac{\boldsymbol{K}}{\mu} \nabla w \, d\Omega \tag{119}$$

$$f^e = \int_{\Omega^e} \nabla w . \frac{\boldsymbol{K}}{\mu} \rho \boldsymbol{g} \, d\Omega \tag{120}$$

$$b^e = \int_{\Gamma^e} \nabla w \, \boldsymbol{u} . \boldsymbol{n} \, d\Gamma \tag{121}$$

Here Ω^e is the element domain, Γ^e is the boundary of the element, w is the linear weighting functions vector and $\boldsymbol{n}$ is a normal vector to the Γ^e boundary domain. Both A^e and f^e terms can be calculated separately for each element and then assembled into the system matrix. When the gravitational effect is neglected, the term f^e turns to be zero. The term b^e is zero where the boundary is closed, and thus it is only non-zero at injection points, venting points, and flow front where the pressure is defined or injection points where the flow rate is specified.

CV/FEM simulation is an explicit time integration method that can solve mold filling process, i.e. a transient problem. The calculation basically consists of two stages. First, the pressure distribution in the mold is computed by using Galerkin Finite Element Method (FEM) approximation. Here, the pressure is set to be zero at the nodes that are empty and these empty elements are eliminated in order to reduce computational load.

In the second stage, Control Volume (CV) method is implemented to eventually advance the resin flow. Having known the pressure field, the velocity field is calculated from Darcy's Law. Then the time step is determined so that the largest time increment is selected to fill exactly one control volume. Once the time step is known, flow front can be advanced and the other parameters, such as fill factors, nodal fill times, can be updated for a next iteration. If additional time adjusted operation is set, for example, pressure or flow rate may change or injection/venting gates open and close at specified times, boundary conditions are adjusted for a next iteration. This cycle is continued until the mold is completely filled.

In the software, Galerkin Finite Element Method and linear elements are preferred for discretization in order to take the advantage of equivalence of the finite element and control volume discretization. Finite element discretization for a linear element and control volume formulation in which the net flow into a nodal volume is computed by taking the integral along the boundary of the control volume are equal [44]. Hence, mass is conserved equally in each element and each node, while the pressure field is approximated for each iteration. As a consequence, the solution can converge to the exact solution if proper mesh size is used.

4.2. CONSTRUCTING THE FINITE ELEMENT MODEL

In RTM-Worx flow simulation Software, a so-called $2\frac{1}{2}$D modeling technique is implemented by which the resin flow equation is solved in 2D, while the geometry is in 3D space. As the through-thickness resin flow in shell-like structures is negligible, this assumption yields highly accurate solutions for many thin composite structures with a reduced computational load.

The models in the software can be created by using the geometry editor that is basically a 3D surface modeler, where parts are assumed to be thin-walled. Key points are first generated to define vertices of a mid-plane of surface and then they are connected to form edges. Surfaces are defined by enclosing the consecutive curves. The software, furthermore, is capable of importing dxf or stl file formats for generating complicated geometries.

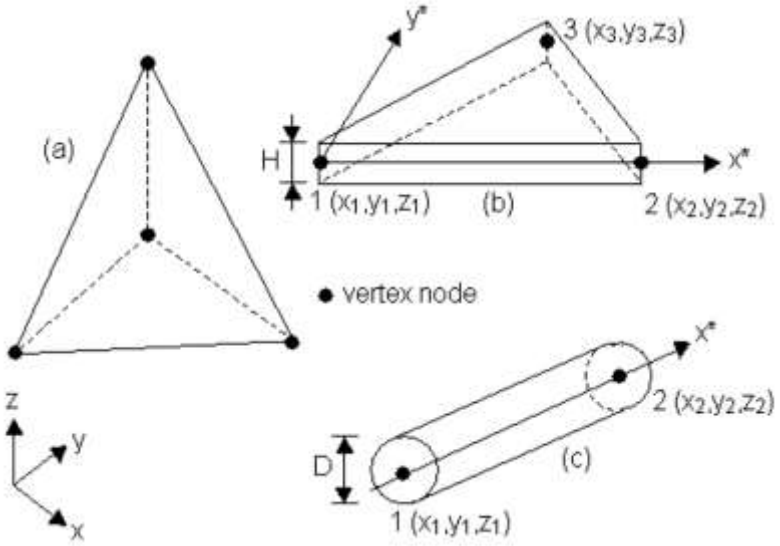

Figure 53. Element types in RTM-Worx [43], (a)3D linear tetrahedron, (b)2D Linear triangular shell (c)1D linear runner

RTM-Worx uses linear elements to discretize the physical domain as mentioned earlier. Figure 53 shows the element types used in the software. Runners are discretized as 1D line elements, whereas reinforcements are divided into either 2D triangular shell or 3D tetrahedron elements. The injection and venting gates, on the other hand, are assigned at key points. The model is meshed automatically based on the distance between key points, which is also known as the graded mesh. By adjusting the minimum and maximum allowable element size, one can change the discretization. The algorithm, additionally, allows to create quasi-uniform mesh along with easy refinement or coarsening the model.

Having created the model, the injection strategy needs to be specified. RTM-Worx has a wide variety of material properties for VARTM, which allows specifying almost all materials in the process. Aforementioned runners can be specified as an isothermal runner or RTM runner, which is filled with a reinforcement material. For an isothermal runner, only a diameter is required to specified, whereas permeability, porosity along with the cross-sectional area are required to be determined for RTM runner. A venting gate is identified by the opening/closing time, while pressure or flow rate information along with the opening/closing time is necessary to specify an injection gate.

Finally, the resin viscosity property and effect of gravity are defined prior to run resin flow simulation. Furthermore, the increment of fill time at which the results are saved and relative precision parameter in iterations can be adjusted. Once these parameters are specified, the simulation is ready to run.

4.3. VALIDATION OF RTM-WORX MODEL

4.3.1. Structure of Validation Model

The purpose of this section is to successfully verify the actual VARTM results with the constructed model. The validation of experimental results has two aims: (1) choosing the appropriate resin viscosity model (2) verifying the accuracy of RTM-Worx flow model for use in VARTM analysis.

4.3.2. Experimental Setup

An infusion was performed to verify the constructed numerical model. For the sake of simplicity, two plies of plain weave carbon fiber preform were used. Resin temperature, mold temperature, and top surface (vacuum bag) temperature were continuously recorded by thermocouples during the process. Vacuum pressures at the beginning and the end of the process were also reported. Figure 54 presents the experiment set-up.

4.3.3. Validation Test Results

Figure 55 shows the temperature history during the infusion process. It is seen that resin temperature was initially 36.5 ˚C and eventually reacted to 33.7 ˚C by constantly decreasing throughout the process. The similar trend was observed for both mold and top surface temperatures. At the beginning of the process, mold and top surface temperature were recorded as 25.3 ˚C and 25 ˚C respectively, whereas they were measured as 19.2 ˚C and 20.3 ˚C at the end.

Figure 54. Validation Experiment Set-up

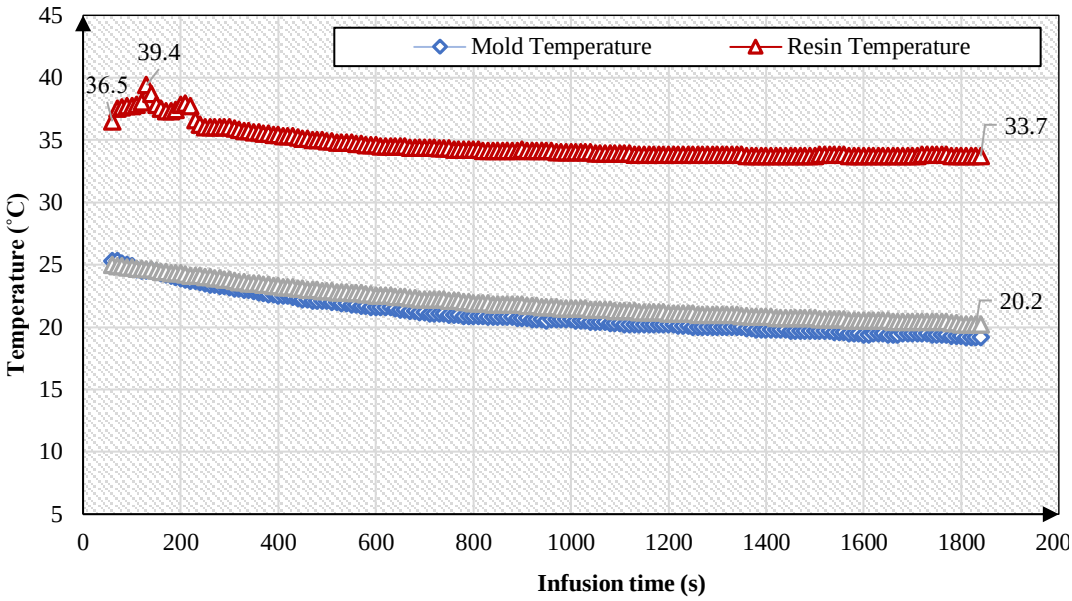

Figure 55. Experiment Temperature History

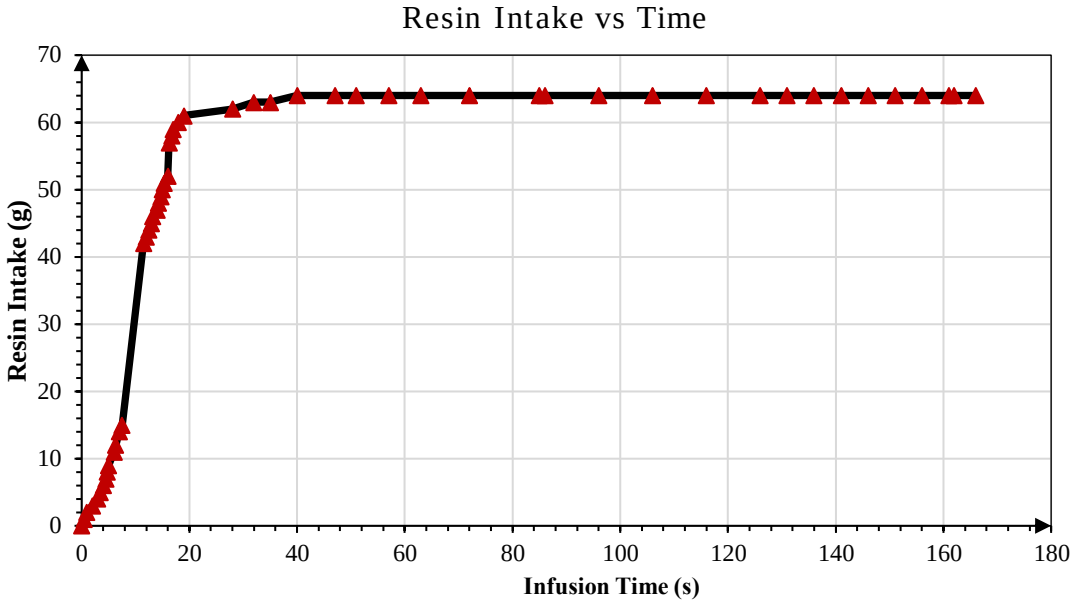

Figure 56. Resin intake to part during the experiment

Additionally, resin pot was placed on the scale and the resin intake into the sample was continuously recorded by video camera. The scale was calibrated and had an accuracy of ±2 grams. Figure 56 presents the resin intake record during the process. It is shown that totally 64 grams of resin were taken in the process.

4.4. STRUCTURE OF RTM-WORX SIMULATION MODELS

RTM-Worx simulations are basically split into two categories based on the temperature consideration: isothermal and non-isothermal models. Non-isothermal models, furthermore, are divided into two branches based on the consideration of resin reaction effect: Non-isothermal Non-reactive (NINR) and Non-isothermal Reactive (NIR). Three different viscosity models, Arrhenius, Castro – Macosko and Lee – Han, are used in NIR models. The whole structure of RTM-Worx simulations is presented in Figure 57.

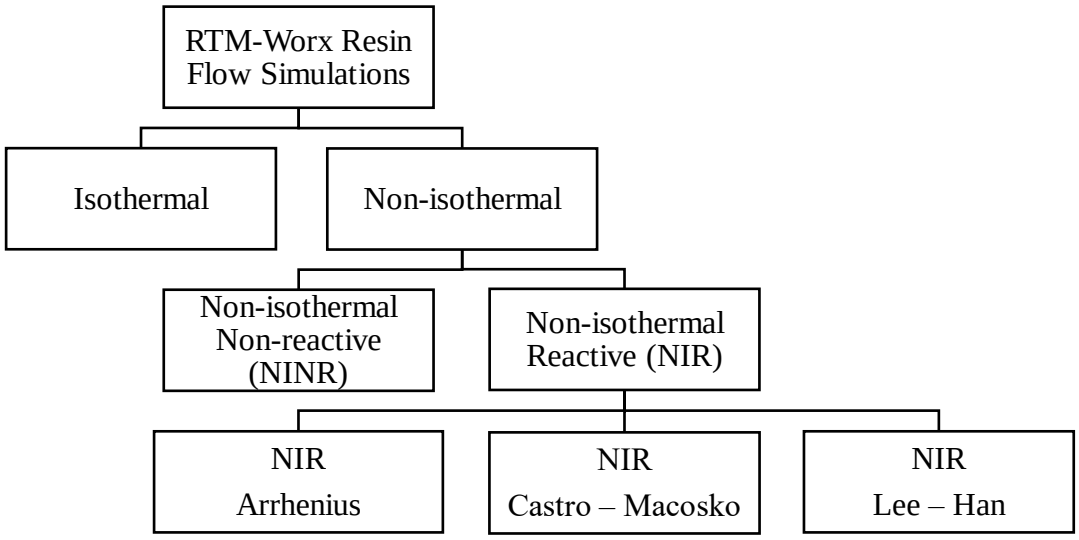

Figure 57. Structure of RTM-Worx simulation models

4.5. ISOTHERMAL MODEL

In the isothermal model, temperature changes during the infusion are neglected. In other words, preform and mold temperatures have the same temperature at the beginning of the process. The change in resin viscosity due to temperature change is also neglected and resin viscosity is assumed to be constant throughout the simulation. The average of beginning and final temperatures, i.e. 35 ˚C, is taken and the viscosity is evaluated for the related temperature. Additionally, curing effect on resin viscosity is not taken into account in this type of simulation. The parameters of isothermal simulations are stated in Table 11.

Table 11. Isothermal simulation parameters

Resin Inlet Temperature	35 ˚C
Resin Viscosity (at 35 ˚C)	0.34 Pa.s
Pressure Difference	97325 Pa

4.6. NON-ISOTHERMAL MODELS

As resin enters the mold, it contacts with preform and mold, which typically have lower temperatures. As a result of this temperature change and consequently resin viscosity changes throughout the process. Another source of temperature variation is the polymerization reaction of the resin system. Polymerization is an exothermic reaction and generates heat to the system. On the other hand, cross-linking takes place during the polymerization reaction, which immobilizes resin molecules thereby decreasing the viscosity. The non-isothermal model takes into account the temperature change effect on viscosity. Non-isothermal models are referred as non-isothermal non-reactive (NINR) model or non-isothermal reactive model (NIR) based on the consideration of resin polymerization effect.

Resin density is evaluated by using the rule of mixture. The densities of neat resin and hardener are taken from the manufacturer's datasheet [25] and the resin density is calculated as 1100 kg/m^3 at the room temperature. The density of resin as a function of temperature was established by Mijovic and Wang [45].

$$\rho(T) = -1x10^{-4}T + 1.1298 \quad (122)$$

Here temperature is in K and density in g/cm^3. The density at 35˚C, which is the average resin temperature in the infusion, is then calculated as 1098.9 kg/m^3.

The specific heat of resin was reported as 1.37 kJ/kg ˚C at 35˚C from Evseeva and Tanaeva [46]. Since temperature difference is considerably low to make a significant difference in the heat capacity, heat capacity value of resin is assumed to be constant.

The conductivity of epoxy resin was reported as 0.2 W/m.˚C from Yoshihiro et al. [47] and highly close value at average resin temperature 35˚C was recorded by Garrett and Rosenberg [48]. Therefore, the conductivity of epoxy resin is selected as 0.2 W/m.˚C and is assumed to be constant based on the fact that relatively small temperature difference occurs during the process. Thermal properties of the resin are stated in Table 12.

Plain weave carbon fiber cloth employed in this study is weaved by Spinteks (Turkey). The company weaves 3K-A38 carbon fibers supplied from DowAksa (Turkey). So, the density of carbon fiber is retrieved from manufacturer's datasheet [49]. However, the specific heat value of carbon fiber is not published by DowAksa and it is taken from similar material cited by Cytec [50].

Carbon fiber has inherently anisotropic nature in the sense of thermal conductivity. But this anisotropy is relatively balanced for a plain weave cloth. Yoshihiro et al. researched on the effective in-plane thermal conductivity of six layers balanced twill-woven carbon fiber stack and reported the value of 1.4 W/m.˚C at 0.40 fiber volume fraction. This value is preferred to use in this study. Another reason to select this value is the author retrieved the result under a vacuum environment, which is the case in our study. Table 13 presents the thermal properties of the preform. Thermal boundary conditions of validation simulations are given in Appendix B.

Table 12. Resin thermal properties

Property	Value	Reference
Resin density (at 23˚C)	1100 kg/m^3	[25]
Resin density (at 35˚C)	1098.9 kg/m^3	[45]
Resin specific heat (at 35˚C)	1370 J/kg.˚C	[46]
Resin conductivity (at 35˚C)	0.2 W/m.˚C	[47] and [48]

Table 13. Preform thermal properties

Property	Value	Reference
Preform density	1780 kg/m^3	[49]
Preform specific heat	710 J/kg.˚C	[50]
Preform effective in-plane thermal conductivity (at RT, V_f=0.40)	1.4 W/m.˚C	[51]

4.6.1. Non-isothermal Non-reactive (NINR) Model

NINR model does not take into account the resin reaction effect. Except the resin reaction, all other parameters are identical to NIR model and as a consequence, higher fill time results are expected from NINR model compared to NIR model. The simulation properties of NINR model are stated in Table 14.

Table 14. Non-isothermal non-reactive (NINR) simulation properties

Viscosity non-isothermal model (Arrhenius Model)	$\mu = 7.431x10^{-8}e^{4731.8\left(\frac{1}{T}\right)}$
Resin Inlet Temperature	36.5 ˚C
Mold Temperature	25 ˚C
Pressure Difference	97325 Pa

4.6.2. Non-isothermal Reactive (NIR) Model

In NIR simulations polymerization takes into account and thus additional heat source is generated in the system. As a consequence of that, more accurate results compared to NINR simulations are expected to achieve.

In NIR simulations, three different viscosity models that have established in Section 2.2.3 and Section 2.2.4 were employed. Among them, Castro-Macosko and Lee-Han models consider the cure dependence. Table 15 shows the properties used in NIR simulations.

Kamal-Sourour reaction model is used by RTM-Worx, i.e. given below [52].

$$\frac{d\alpha}{dt} = (k_{10}e^{-E_1/RT} + k_{20}e^{-E_2/RT}\alpha^{m_{kamal}})(1-\alpha)^{n_{kamal}} \quad (123)$$

The kinematic parameters of a thermoset resin can be obtained by a dynamic differential scanning calorimetry (DSC). Kim and Kim reported the kinematic parameters of epoxy and these values are used in simulations. Table 16 presents the kinetics properties of the resin.

Table 15. Non-isothermal reactive (NIR) simulation properties

Viscosity non-isothermal model (Arrhenius Model)	$\mu = 7.431x10^{-8}e^{4731.8\left(\frac{1}{T}\right)}$
Viscosity non-isothermal cure-dependent model (Castro-Macosko Model)	$\mu = 7.431x10^{-8}e^{4731.8\left(\frac{1}{T}\right)}\left(\frac{\alpha_{gel}}{\alpha_{gel}-\alpha}\right)^{-11.133+83.648\alpha}$
Viscosity non-isothermal cure-dependent model (Lee-Han Model)	$\mu = 7.431x10^{-8}e^{4731.8\left(\frac{1}{T}\right)}e^{(-0.479+\frac{1.432}{T})\alpha}$
Resin Inlet Temperature	36.5 ˚C
Mold Temperature	25 ˚C
Pressure Difference	97325 Pa

Table 16. Resin cure kinetics properties

Property	Value	Reference
Heat of reaction	217 J/g	[27]
Rate constant for non-catalysed reaction, k_{10}	$1x10^{11}$ (1/min)	[27]
Arrhenius constant, E_1	$7.795x10^{4}$ (J/mol)	[27]
Rate constant for auto-catalysed reaction, k_{20}	0 (1/min)	[27]
Arrhenius constant, E_2	0 (J/mol)	[27]
Model coefficient, m_{kamal}	0	[27]
Model coefficient, n_{kamal}	1.64	[27]
Critical conversion at gelation, α_{gel}	0.894	[27]

4.7. SIMULATION RESULTS

The flow front location was plotted against time to compare the experimental results with simulations. Simulations are divided as isothermal and non-isothermal based on thermal consideration. Non-isothermal models are also divided into two groups: Non-reactive model and reactive model. Three different resin models, which are Arrhenius, Castro-Macosko, and Lee & Han, were additionally used in NIR simulations. Therefore, totally five different simulation models were performed and compared in this study.

Figure 58 presents the flow front location against time. Darcy's Law was also plotted for comparison reasons. It is seen that the isothermal model yields highly close results with Darcy's Law and fits very well with experimental results up to 0.07m. Above that point, the isothermal model remarkably overpredicts the flow front.

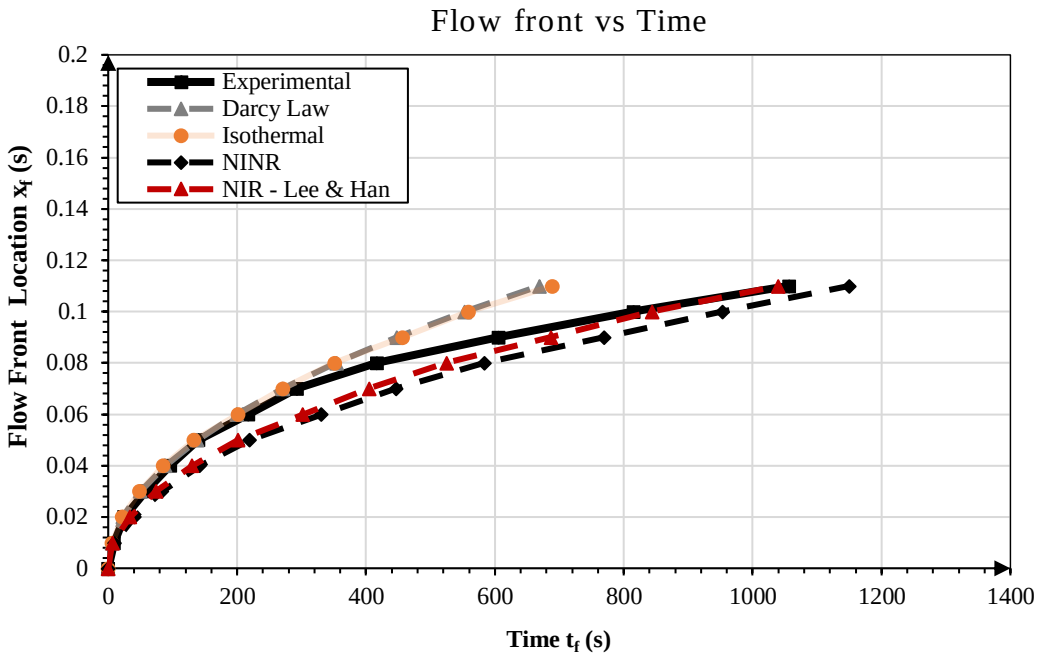

Figure 58. Validation Test Results

Non-isothermal models under predict flow front in the early stages, however, yield highly accurate results in further positions. From Figure 58, it can be seen that non-isothermal models especially NIR models give more accurate results compared to the isothermal model. Moreover, non-isothermal models better estimate fill time values than the isothermal model.

To better compare the models, root mean square errors were evaluated and plotted in Figure 59. Fill time error percentage was also included in the graph. It is seen that Darcy's Law and Isothermal are the least accurate models and deviate from the experimental results with RMSE values of 144 and 138 respectively. The fill time results of these models are highly far from the actual value of 1056s.

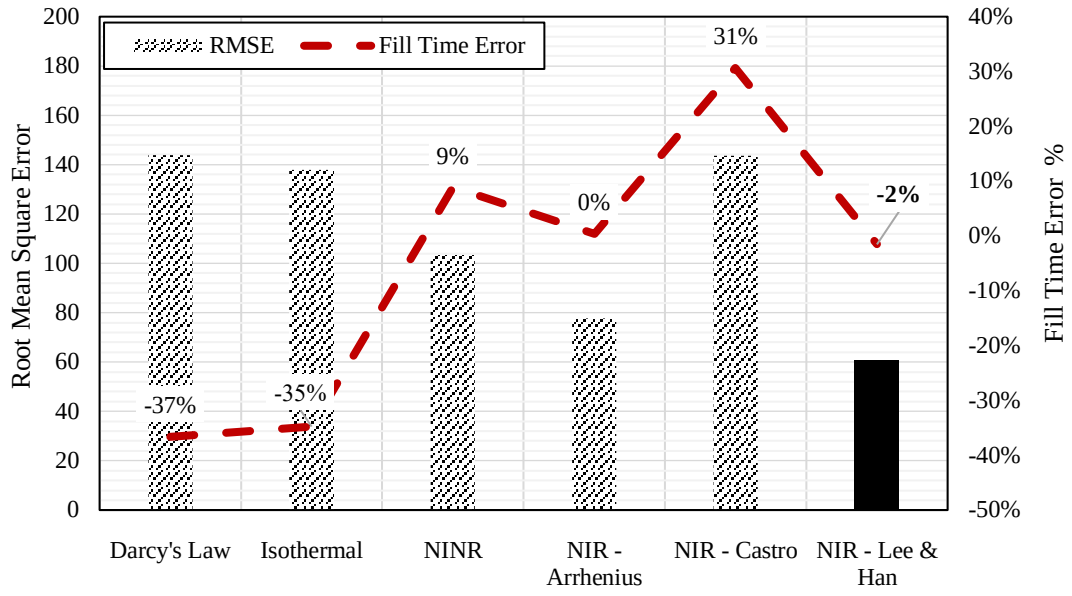

Figure 59. Comparison of simulation models

Non-isothermal models, except NIR-Castro, have lower RMS-errors than the Darcy's Law and the isothermal model. One can see from Figure 59 that even though NIR-Castro overestimates the exact results, yields very close percentage error to the isothermal model, which actually under predicts the results. NIR – Lee & Han reaches the minimum RMSE value of 61 and deviates from the exact fill time with just 2%. In the light of this analysis, it can be concluded that NIR – Lee & Han is the most accurate one among the five simulation models.

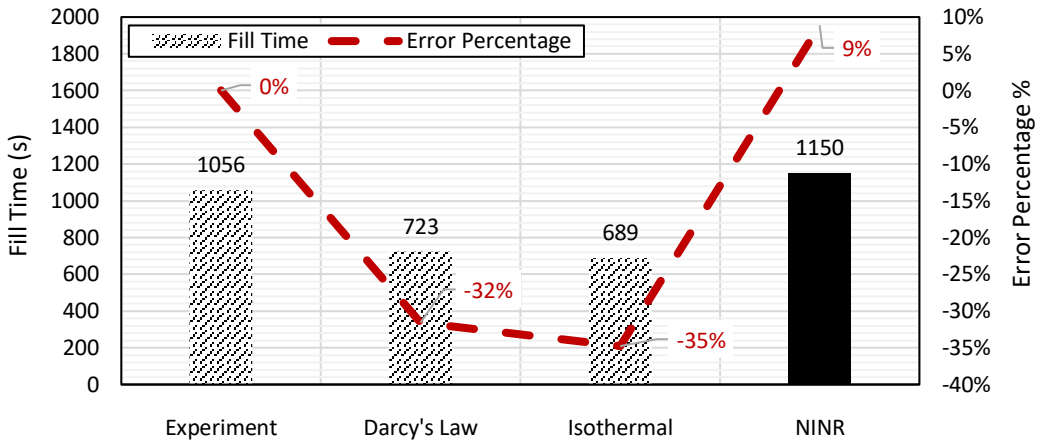

Figure 60. Comparison between NIR – Lee & Han (RTM-Worx) and coupled fill-time results

The coupled fill-time solutions, which account the varying thickness and pressure profile in VARTM process, are compared with RTM-Worx Simulations. It can be seen from Figure 60 that RTM-Worx, NIR – Lee & Han model, yields significantly more accurate results compared to the coupled fill-time results. As previously discussed in Chapter 3, this is due to the fact that selecting the proper resin viscosity model is the dominant factor in the accuracy of resin impregnation simulations.

CHAPTER 5

EXPERIMENTAL INVESTIGATION OF THE CO-CURING PROCESS

In this chapter the experimental investigation of the co-curing process is presented. In the co-curing using VARTM process, foam material, foam strength, curing operation and foam coating are considered to be the critical process parameters. The co-curing process is improved by selecting the optimum process parameters. The manufacture procedure of the co-curing and secondary bonding processes for the three-cell composite box beam are given in detail.

5.1. MANUFACTURING OF CO-CURED MULTI-CELL BOX BEAM

Co-cured manufacturing starts with the preparation of the polystyrene foams that have the shape of the cells of the box beam. The hard-polystyrene foams are selected so that they are soluble and can be removed subsequently by using chemical solvent. A perfect mold should withstand the vacuum pressure during infusion. Hence, the foams are hardened with epoxy to enhance surface hardness and improve surface smoothness. Figure 61 shows the foam molds coated with epoxy. Distribution media, which is also called as distribution mesh or flow mesh, is a highly permeable surface layer that accelerates the resin flow during resin infusion. In contrast to RTM, a distribution media is necessary to expedite the resin impregnation, since the resin pressure gradient is comparatively low. Distribution media basically increases the overall permeability of the preform – fabric and distribution media assembly. In this study, distribution media is wrapped around the foams and is attached by using fiberglass fabric tape. Figure 34 presents the epoxy coated molds wrapped with distribution media.

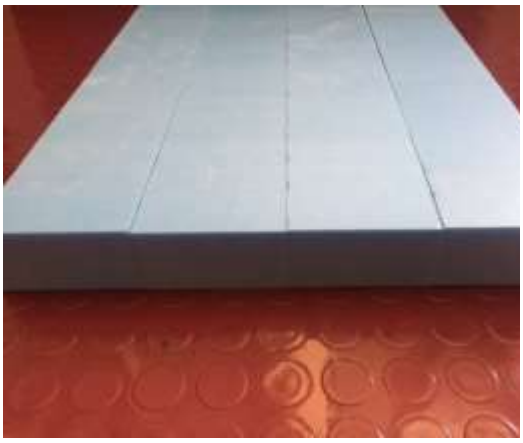

Figure 61. Foam molds coated with epoxy resin

Figure 62. Epoxy coated molds wrapped with distribution media

The next step is to wrap peel ply over the distribution media. Peel ply, also called as release fabric, is a disposable cloth that eases the removal of the cured part. There are several other purposes of using peel ply in the VARTM process. It basically acts as a release film so that prevents foreign materials from becoming integrated into the finished product. Furthermore, peel ply has a porous surface to texture the part surface, which is needed for a subsequent bonding operation. Peel ply also provides the vacuum continuity between preforms and vacuum channels. Peel ply is either nylon or polyester woven fabrics and can be supplied coated with a release agent or uncoated. The aim of the release agent in peel ply is to aid the ease of removal of complex shapes or aggressive resin systems. Uncoated peel ply fabric is employed in the current practice. A peel ply layer is covered around with the help of a spray adhesive, i.e. shown in Figure 63.

Having wrapped a layer of peel ply, carbon fiber plain woven layers are rolled around the peel ply and the mold is covered with the specified number of layers depending on the thickness requirement. In this practice, five layers of carbon fiber woven layers are wrapped in order to provide the designed thickness of 3mm. Figure 64 presents the prepared molds covered with carbon fiber fabrics.

Figure 63. Molds wrapped with peel ply

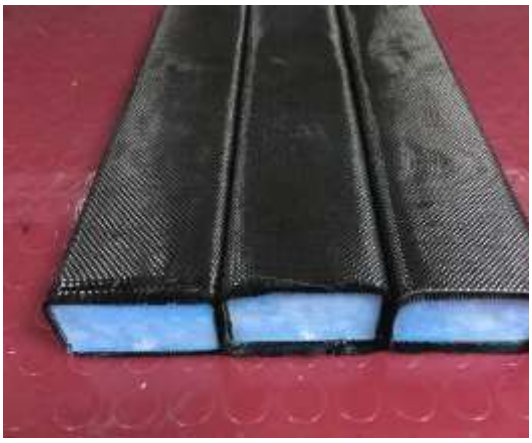

Figure 64. Carbon fiber fabrics are wrapped around the peel ply

Having prepared the three molds, a flat mold surface is coated with mold release agent, which will be the lower surface of the part. A flat glass mold, also called as tool plate, is preferred for this study because of its availability and affordability. Application of mold release agent is shown in Figure 65.

Following the tool plate preparation, a layer of distribution media is draped on the flat surface. Typically, distribution media locates between the peel ply and vacuum bag, however, in this application, it is also laid at the bottom to ease the wetting of the lower surface of the preform. A peel ply is placed on the distribution media to enable to separate the distribution media from the part. After that, layers of carbon fiber fabrics are draped on the peel ply, as shown in Figure 66. Subsequently, three foam molds are placed on the carbon fiber preform and then additional layers, which will form the top skin, are placed on the molds. The part at this stage is shown in Figure 67. Similar to the lower surface, a layer of peel and distribution media are placed on the top surface.

Figure 65. Application of mold release agent

Figure 66. Placement of distribution media, peel ply and carbon fiber fabrics

Having positioned the molds and fabric preform, resin and vacuum connections need to be placed. One resin feed line is enough to wet the whole part based on the numerical analysis did in Chapter 4. Since one of the purposes of this study is to check the validity of the numerical analysis, same resin flow strategy is applied in the experiment. Therefore, a resin feed line is placed 30mm away from the edge, whereas the suction line is placed along the opposite edge. Feed and suction lines are secured by using fiberglass fabric tape. Figure 68 shows the resin strategy of the process.

Next step is to seal the workpiece with sealant tape. For the sake of success in VARTM process, sealing is highly critical and special care needs to be taken. The sealant tape is first placed all around the workpiece to subsequently seal vacuum bag. Then, small pieces of sealant tape are cut and wrapped around each connection. As the connections are possible leak sources, sealing of connections are extremely important. Having placed sealant tape, the workpiece is covered with a vacuum bag. It is important to work with vacuum bag properly, since it is highly fragile to be punctured. While securing the vacuum bag, the cover of sealant tears slowly. Once the whole workpiece is fully sealed, a small pressure is exerted on the sealant tape to make sure it is fully closed.

Before the application of vacuum, a leak test is desirable to ensure the vacuum continuity. The feed line is closed by using clamps and suction line is connected to the resin pot that is in the closed position. Then, the vacuum pump is connected to the resin pot and switched on to get ready for leak testing. A leak test is applied typically for 30 minutes to make sure the workpiece is airtight prior to infusion.

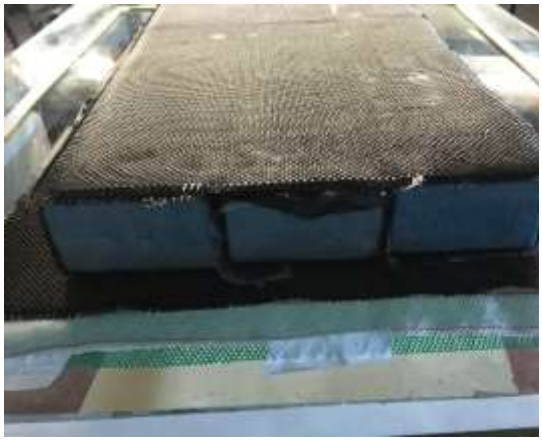

Figure 67. Placement of three mold pieces over the mold surface

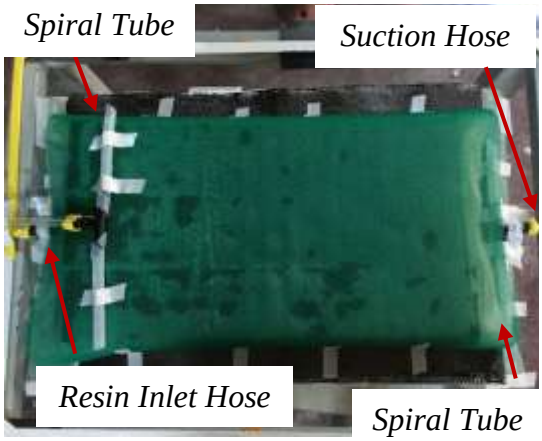

Figure 68. Positioning of resin inlet, air suction hoses and spiral tubes over the part

Figure 69 presents the part under vacuum. Straight lines for the purpose of calculating resin flow time are sketched and the video camera is placed prior to infusion. Once the leak test is completed successfully, resin feed line is immersed in the resin bucked and released. After the release of clamps, resin starts to impregnate fabric preform and travels along the workpiece. As the suction line in the bottom and the feed line is on the top surface, the resin is forced to travel against the molds and lead-lag between the top and bottom surfaces occurs. Therefore, when bottom surface is fully wetted, some dry regions remain on the top surface. Figure 70 presents the infusion process.

Having completed the resin impregnation, the part is cured under the predetermined curing profile. Finally, the foams are dissolved by using acetone to achieve the final part. The part before foam removal is shown in Figure 71.

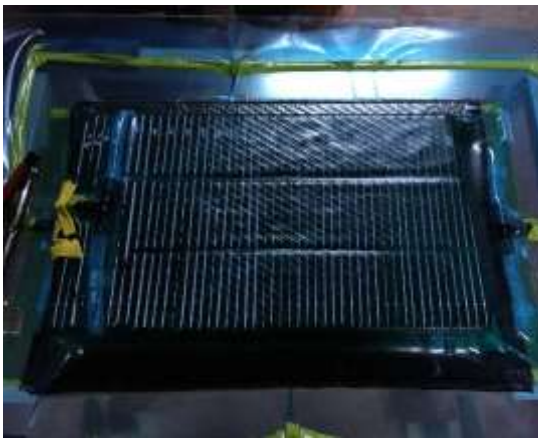

Figure 69. Photograph of the set-up covered with vacuum bag

Figure 70. Photograph of vacuum bagged assembly during infusion

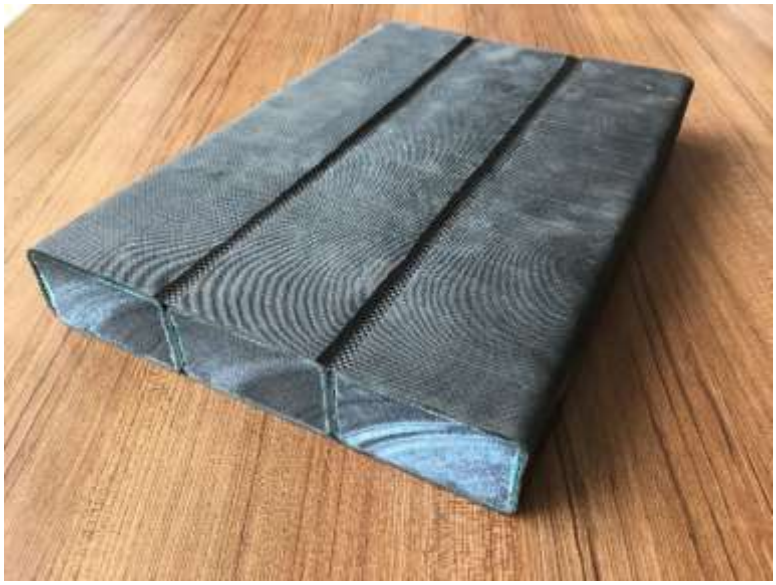

Figure 71. Photograph of co-cured composite box beam before foam removal

5.2. PROCESS IMPROVEMENT FOR CO-CURING OF BOX BEAM COMPOSITES

The manufacturing procedure of the co-curing process of three-cell composite box beam is given in the previous section. In this section, the process improvement study for the same application is presented. Foam material, foam strength, curing operation and foam coating are considered to be the critical process parameters and a series of experiments is conducted to obtain the best process parameters.

5.2.1. Foam Material Selection

Foams are used as a removable mandrel in this study. Fabric preforms are wrapped around foams to form the geometry during the infusion stage and after the curing operation foams are extracted from the part. A good removable mandrel should have the following properties:

- Sufficient compressive strength under vacuum pressure.
- Impermeable to low viscosity resin.
- Easily removable from the part.

As mentioned in Section 1.1.6, Polystyrene (PS) foams are solvent soluble and are in two kinds as Expanded Polystyrene (EPS) and Extruded Polystyrene (XPS). Extruded Polystyrene (XPS) has higher stiffness, better surface finish, and better solubility. Since high compressive strength and better solubility are desirable in this study, Extruded Polystyrene (XPS) is preferred.

Two types of polystyrene foams were employed in experiments. Both foams were manufactured by the same company and the only difference was their compressive strength. The first type of foam has 100 kPa compressive strength at 10% deflection according to Standard Test Method for Compressive Strengths of Rigid Cellular Plastics ASTM D1621 [53], whereas the second type withstands 300 kPa compressive strength under the equal condition [54].

5.2.2. Curing Process

Having completed the resin infusion, the part is placed into an oven for the curing process. The curing, also knowns as the polymerization reaction, is a process in which exothermic polymerization reaction takes place and phase of polymeric resin changes. During curing process, polymer chains link with each other and generate three-dimensional network structure, i.e. called as cross-linking. Cross-links in resin form three-dimensional network structure so that immobilizes the molecules and hardens the resin thereby providing strength.

The curing process is activated by heating, chemical additives or electron beams. The resin used in this study starts curing when the catalyst is added and the reaction is accelerated by applying heating. Thus, the resin is initially in viscous state at room temperature, but when the resin is mixed with the catalyst, it starts to harden and eventually becomes solid.

In the experiments, Huntsman XB 3585 Epoxy Resin and Huntsman Hardener XB 3486 [25] were used and the curing cycles were determined by Manufacturer's recommend cure cycle. On the other hand, the technique preferred in this study involves polystyrene foam molds that are susceptible to excessive heating. Hence, the optimization of curing temperature and time had two goals: (1) Desirable glass transition temperature (T_g) needs to be achieved (2) Polystyrene foams should be stable during the curing process.

Curing cycle profiles were selected from the Manufacturer's recommend cure cycle [25]. In the first experiment, the first type of foam molds [53] was employed and highest curing temperature from the technical data sheet, which is 100˚C at 5 hours, was preferred. After curing operation, foams were partly melted and were highly degenerated as seen in Figure 72.

Figure 72. Photograph of Experiment No.1 before foam removal (Type 1, uncoated, 100˚C-5h)

Having experienced the issue of excessive heating of the mold, different curing profiles were tried and the profiles are stated in Figure 75. In the Experiment No.2 curing was conducted at 80˚C for 8 hours and no foam melting was observed, as shown in Figure 76. Nevertheless, foams could not preserve their structural stability under vacuum pressure and caused fiber buckling, see Figure 74. Note that again the first type molds were used in Experiment 2.

Figure 73. Photograph of Experiment No.2 before foam removal (Type 1, coated, 80˚C-8h)

Figure 74. Fiber buckling caused by structurally unstable polystyrene foams

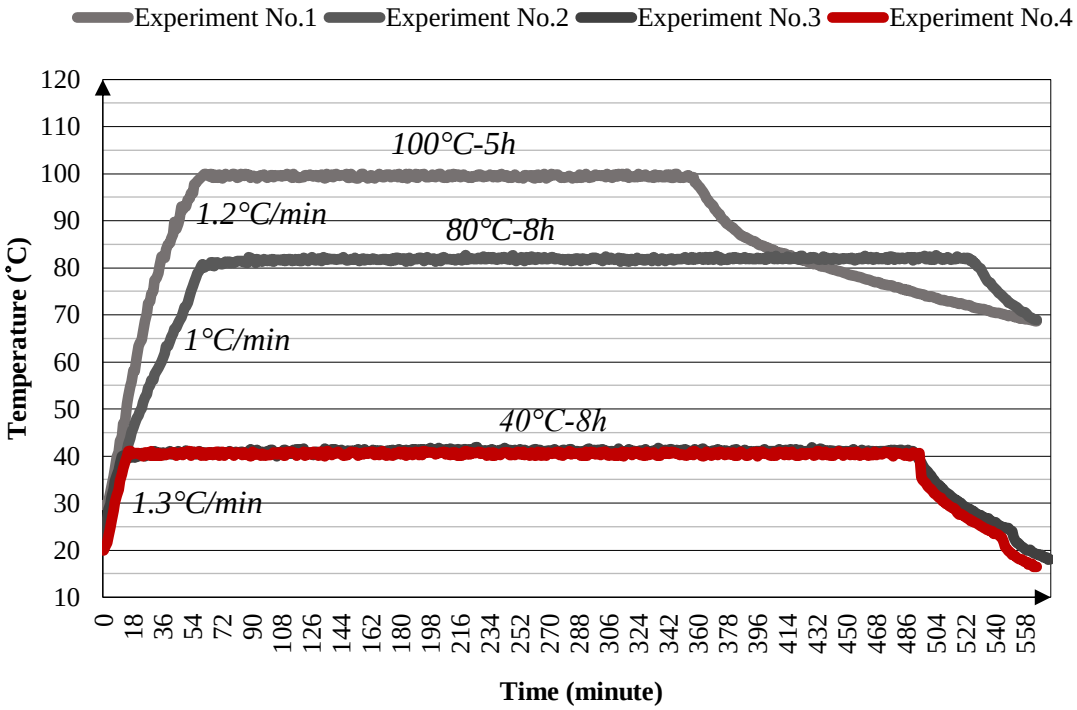

Figure 75. Temperature vs Time graph of Experiments

5.2.3. Foam Compressive Strength

As Mentioned in Section 5.2.1, two types of polystyrene foams from the same manufacturer were employed in experiments. The sole difference between foams is their compressive strengths that are 100 kPa and 300kPa at 10% deflection under the test condition stated in ASTM D162.

The second type of foams [54] was used in the Experiment No.3. In contrast to Experiment No.1 and Experiment No2., foams remained structurally stable after the process, which resulted in better part quality. Figure 76 shows the part manufactured in Experiment No.3 before the foam removal process.

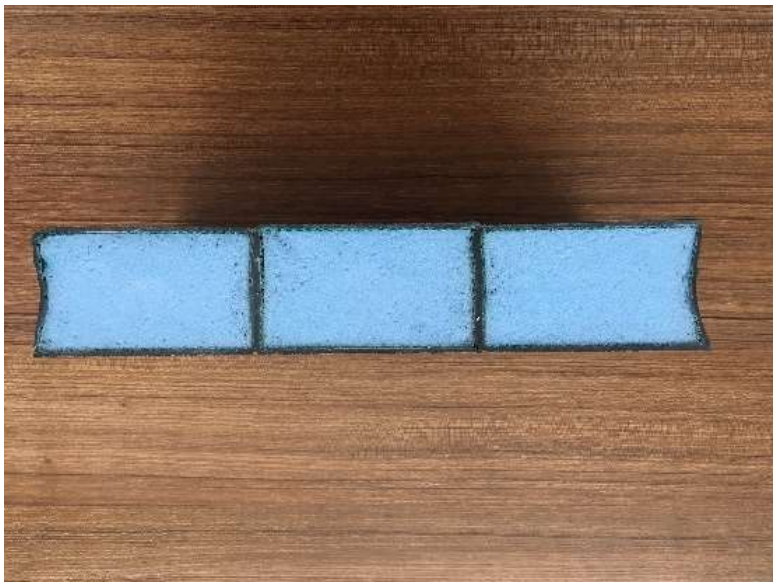

Figure 76. Photograph of Experiment No.3 before foam removal (Type 2, coated, 40˚C-8h)

5.2.4. Foam Coating

Polystyrene foams were hardened with the same epoxy prior to the process. There are three reasons to apply this treatment. First, epoxy hardening enhances the surface hardness of foams that gives additional resistance against the collapse pressure. Second, this treatment improves the surface smoothness, which provides better surface quality of the finished product and furthermore eases the removal process. Third, coating with epoxy ameliorates the impermeability of polystyrene foams to low viscosity resin. This is highly important to predict the fill time of infusion process.

As stated in Table 17 foams were coated two times before the process in Experiment No.4. Figure 77 presents the difference between uncoated and coated foams. Coated foams become slightly darker when they are coated.

Figure 77. Photograph of Uncoated Foam (Left) and Coated Foam (Right)

The result of Experiment No.4 was highly desirable. Foams stayed stable during the process and no fiber buckling was observed, which was the case in Experiment No.2. Compared with Experiment No.3, the better surface finish was achieved at this trial. The co-cured composite box beam produced in Experiment No.4 is shown in Figure 78.

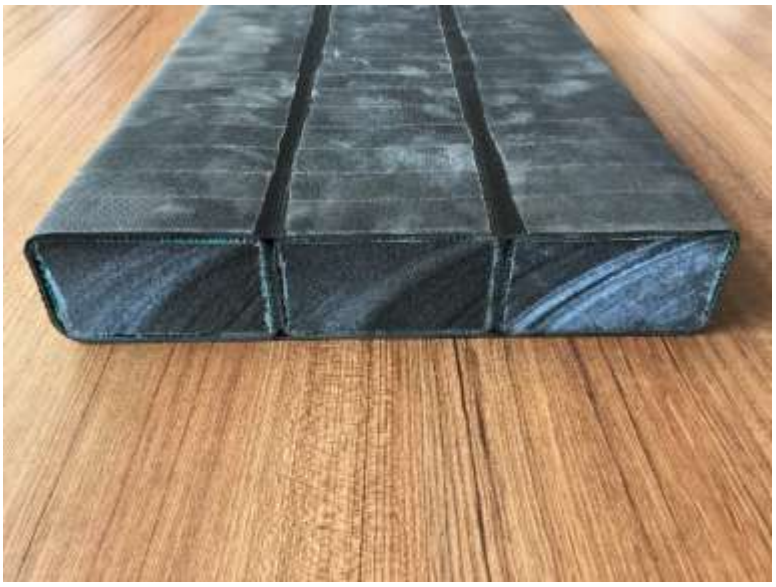

Figure 78. Photograph of Experiment No.4 before foam removal

(Type 2, double coated, 40˚C-8h)

5.2.5. Summary of Experiments

In the experimental study, foam material, foam strength, curing operation and foam coating were considered to process parameters and the co-curing process have been improved by optimizing these parameters. A foam was used as a removable mandrel and was removed after the curing process. PS foam was selected due to its sufficient compressive strength, solubility in the solvent and good surface finish. Specifically, XPS foam was preferred over EPS, since XPS has higher stiffness, better surface finish, and better solubility.

It concluded from the experimental study that the second foam type [54] satisfies the stability condition under vacuum pressure. Among the curing profiles, the optimum result was achieved at 40 ˚C at 8 hours.

Another conclusion is that foam coating is a crucial treatment so that it makes a foam impermeable against low viscosity resin. Furthermore, it improves the surface hardness of foam along with surface smoothness. Double coating is decided to yield better results compared to single coating application. Table 17 shows the summary of the experimental study. It is seen that parameters in the fourth experiment yielded the best final part quality and the part is seen in Figure 79.

Table 17. Manufacturing Summary

Experiment No	Foam Type	Foam Compressive Strength	Epoxy Hardening	Curing Temperature	Curing Time
1	1	100 kPa	Uncoated	100˚C	5h
2	1	100 kPa	Single Coated	80˚C	8h
3	2	300 kPa	Uncoated	40˚C	8h
4	2	300 kPa	Double coated	40˚C	8h

Figure 79. Photograph of co-cured three-cell composite box beam (Type 2, double coated, 40˚C-8h)

5.3. SECONDARY BONDED MULTI-CELL BOX BEAM

The same structure is produced by following the conventional secondary bonding manufacturing procedure in order to make a comparison with the co-cured manufacturing technique. As discussed in Section 1.4.2, sub structures of aircraft structures are conventionally fabricated separately and integrated either via adhesive bonding or mechanical fastening. Mechanical fastening has several drawbacks so that this type of joining might cause weight penalty in the structure and galvanic corrosion problem. In the adhesive bonding, structural adhesives that have high density are used, which yields structures with a weight penalty. For the sake of comparison, the same resin system is preferred to integrate sub-parts in this study.

Secondary bonding manufacturing procedure starts with producing the top skin of the multi-cell box beam. The technique is identical to that of applied in the co-cured manufacturing. The peel ply is first place on the mold plate. The is because a porous surface is desirable for the subsequent secondary bonding operation. Next, seven layers of carbon fiber preform are laid over the peel ply. The final layer of peel ply is draped over the carbon fiber preform and finally, distribution media is placed at the top as seen in Figure 80. Connectors and spiral tubes are positioned and then the set-up is covered by vacuum bag. Finally, the whole set-up is sealed off by using sealant tape, i.e. seen in Figure 81.

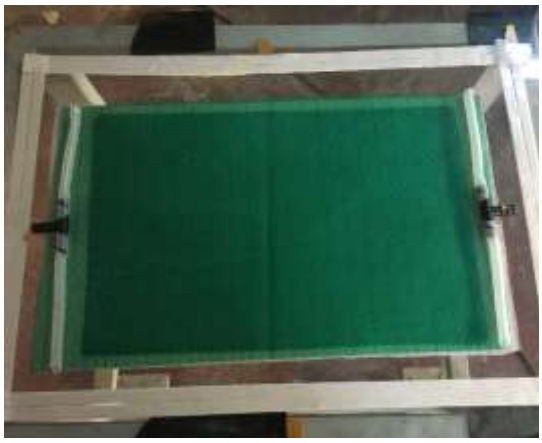

Figure 80. Placement of distribution media, peel ply and carbon fiber fabrics

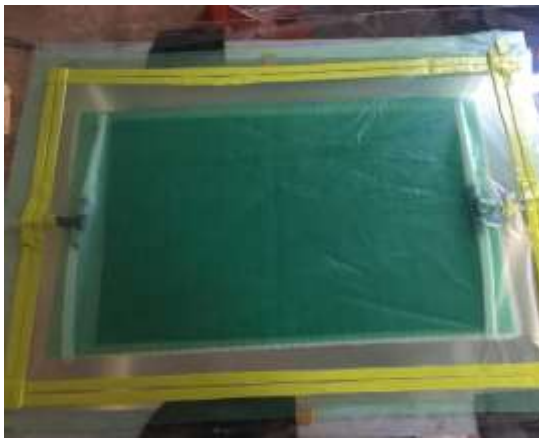

Figure 81. Sealing of whole assembly

Having sealed off the set-up, mark lines are drawn in order to track the flow front. The process is recorded by video camera, which is seen Figure 82. Figure 83 shows the flow front during the infusion process.

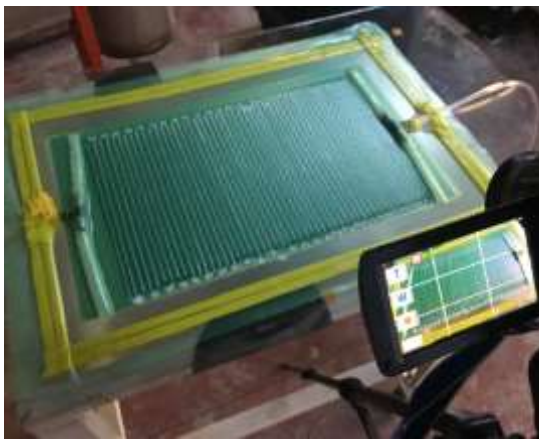

Figure 82. Photograph of vacuum bag assembly during infusion of the top skin

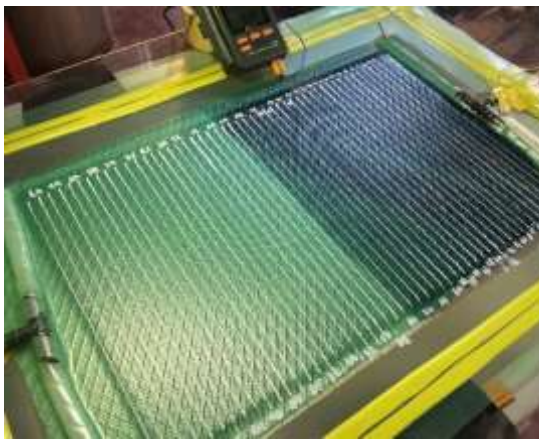

Figure 83. Photograph of resin flow front during infusion of the top skin

Three different stacking sequences are present in the three-cell composite box beam: (1) 5 plies (side webs), (2) 7 plies (top and bottom skins), (3) 10 plies (webs). Thus, sub-parts of three-cell composite box beam are manufactured in four shots.

Figure 84. Photograph of the separately manufactured skins and webs

Figure 85. Photograph of shaped carbon fiber composite sub-parts

Figure 84 presents the separately manufactured sub-parts of the box beam. Next, the sub-parts are cut into shapes using a diamond saw. Figure 85 shows the shaped sub-parts.

Secondary bonding in this study is a three-shot operation and first webs are integrated into the bottom skin. A special care needs to be taken in order to make a desirable bonding and parts should be positioned precisely prior to the operation. Wood curing tools are prepared to accurately create the spacing between webs. It is important to note that wood tools are wrapped with non-porous Teflon film so that tools can be extracted readily after the curing operation, i.e. seen in Figure 86. Figure 87 shows the bonding set-up of skin-web assembly.

Figure 86. Curing tool for skin-web assembly

Figure 87. Pre-bonding set-up for the skin- web assembly

The same resin system is used to integrate the sub-parts. The reason behind selecting the same resin system is to better compare the co-cured manufactured and the secondary-bonded parts. Once the resin is smeared, wood curing tool is positioned and then clamps are attached to exert pressure during the bonding operation. Figure 88 presents the bonding operation of the skin-web assembly. Curing cycle is identical to that of used in the co-curing production and curing is performed within the convective oven, i.e. seen in Figure 89.

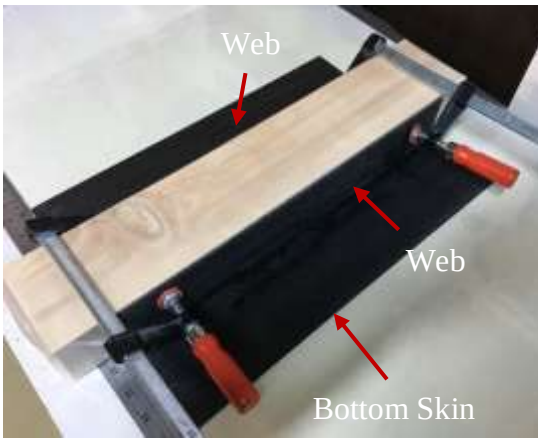

Figure 88. Bonding of the skin-web assembly

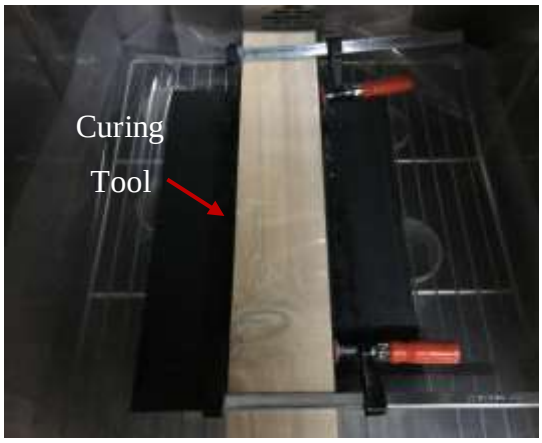

Figure 89. Curing of the secondary-bonding operation

Having integrated the webs, the side webs are next bonded to the bottom skin. Clamps are again used to apply pressure along the circumferences of the side webs. Shims are also employed to accurately position the side webs. Bonding of the side webs is shown in Figure 90 and Figure 91.

Figure 90. Bonding of the side webs

Figure 91. Bonding of the side webs

Bonded skin-web assembly is shown in Figure 92. The last step is to integrate the top skin to the bottom skin-web assembly. Again, the same procedure is followed. Figure 93 presents the secondary bonded three-cell composite box beam.

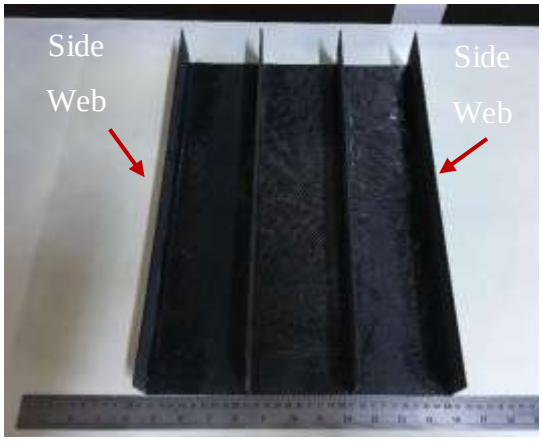

Figure 92. Bonded Bottom Skin-web Assembly

Figure 93. Bonded Three-cell Composite Box Beam

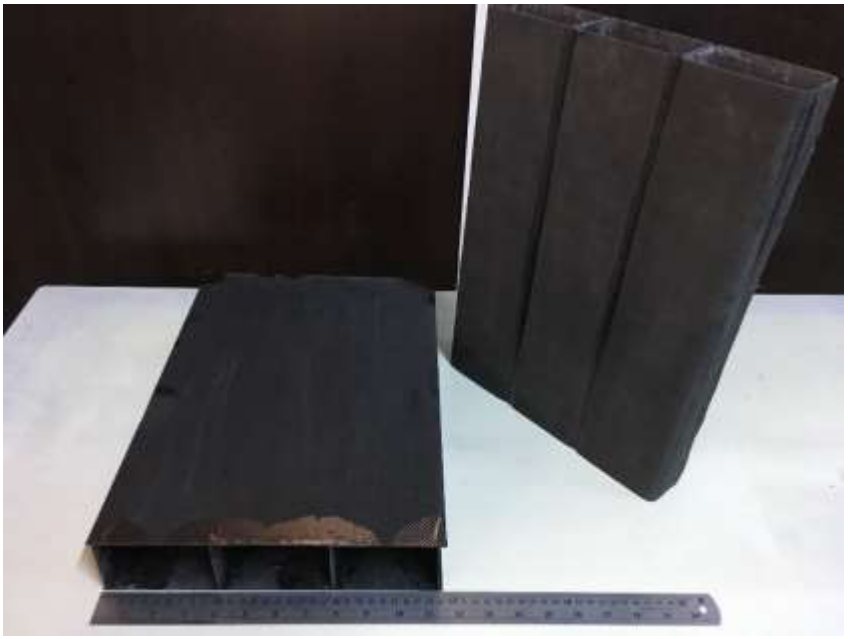

Figure 94. Co-cured and secondary-bonded three-cell composite box beams

CHAPTER 6

RESULTS AND DISCUSSIONS

Chapter 6 presents the comparison study between co-curing and secondary bonding techniques along with the RTM-Worx simulations for three-cell box beam. In the first section of this chapter, RTM-Worx resin impregnation simulations are performed for co-cured three-cell box beam and the simulation results are compared with the experimental results. Second section presents the four-point bending tests that aim to compare the mechanical performance of co-cured and secondary bonded three-cell box beams. Failure mechanisms, maximum and failure load results are discussed. In the third section, a comparison of energy consumption and labor time between the co-curing and conventional techniques is made for the three-cell box beam application.

6.1. COMPARISON OF SIMULATION AND EXPERIMENTAL RESULTS

6.1.1. Constructing the Model

The size of box beam is selected to be consistent with [17] so that the webs are 60mm high and 90mm wide. The assembly is 288.3mm wide and 500mm long.

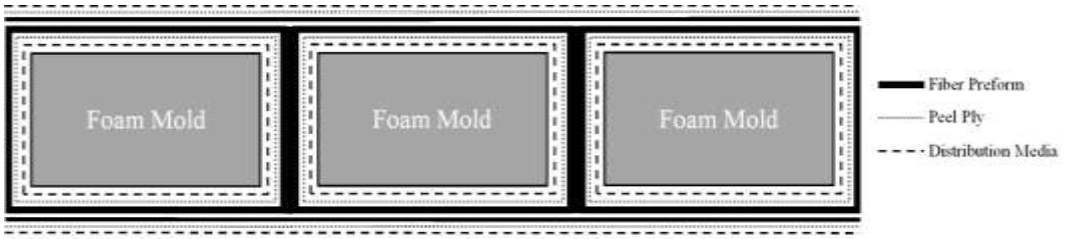

Figure 95. Schematic diagram of the stacking sequences of the box beam

In practice, space needs to secure the injection line thereby the feed line is placed 30mm away from the edge, while the suction line is positioned along the opposite edge. Table 18 presents the composite section properties.

Table 18. Three-cell box beam composite section properties

Skin Thickness	2.1mm
Skin Stacking Sequence	0˚/90˚/0˚/90˚/0˚/90˚/0˚/90˚/0˚/90˚/0˚/90˚/0˚/90˚
Web Thickness	3.0mm
Web Stacking Sequence	0˚/90˚/0˚/90˚/0˚/90˚/0˚/90˚/0˚/90˚/0˚/90˚/0˚/90˚/ 0˚/90˚/0˚/90˚/0˚/90˚
Side Web Thickness	1.5mm
Side Web Stacking Sequence	0˚/90˚/0˚/90˚/0˚/90˚/0˚/90˚/0˚/90˚
Injection Line Diameter	12mm
Suction Line Diameter	12mm

6.1.2. Calculating Spiral Tubes Properties

The spiral tubes in RTM-Worx can be modeled as either isothermal runner or RTM runner. In the former one, only the diameter of the tube is specified and the tube has no permeability. On the other hand, in the latter, the spiral tube is modeled as a circular channel having unidirectional reinforcement material. All spiral tubes are modeled as RTM runner in this study and the permeability of them are calculated from the Hagen-Poiseuille Equation.

$$K_{11} = \frac{r^2}{8} = \frac{(12x10^{-3}m)^2}{8} = 4.5x10^{-6}\, m^2 \tag{124}$$

It is assumed that very small amount of resin is "lost" along with a spiral tube. Since the porosity cannot be zero, otherwise a material would be impermeable, the fiber volume fraction of spiral tube is specified as 0.99.

6.1.3. Calculating the Preform Properties

Preform permeability is evaluated using permeability averaging technique. The technique is simply based on the rule of mixture and is given in Equation (125). The average porosity is similarly calculated using the rule of mixture, i.e. shown in Equation (126). Preform properties employed in this study is stated in Table 19.

$$\bar{K}_{uv} = \frac{1}{H}\sum_{j=1}^{n} h^{(j)} K_{uv}^{(j)} \tag{125}$$

$$\bar{\emptyset} = \frac{1}{H}\sum_{j=1}^{n} h^{(j)} \emptyset^{(j)} \tag{126}$$

Table 19. Preform properties

	Reinforcement Principal Properties					Preform Global Properties		
	Flow Mesh	Peel Ply	CF Preform			Side Web	Skin	Web
Thickness (mm)	1.35	0.2	0.3			3.05	5.2	6.1
Fiber Volume Fraction, v_f	0.15	0.65	0.46 (1)	0.52 (2)	0.55 (3)	0.34	0.40	0.38
Porosity, $\emptyset$	0.85	0.35	0.54 (1)	0.48 (2)	0.45 (3)	0.66	0.60	0.62
Rotation angle, θ°	0	0	0			0	0	0
Permeability, K_{11} (m^2)	3.70E-09	2.16E-12	1.58E-11			1.65E-09	1.31E-09	1.65E-09
Permeability, K_{12} (m^2)	0	0	0			0	0	0
Permeability, K_{22} (m^2)	3.70E-09	2.16E-12	1.58E-11			1.65E-09	1.31E-09	1.65E-09

Note that porosity values change with respect to stacking sequence as discussed in Chapter 2. As the number of preform count differs throughout part sections, this effect is taken into consideration by using associated porosity values.

6.1.4. Discretizing Model

The geometry of the box beam is created using Solidworks and imported to RTM-Worx in stl format. The model is discretized using linear tetrahedron elements, as mentioned in Section 4.2. Figure 96 shows the discretized model of the three-cell box beam.

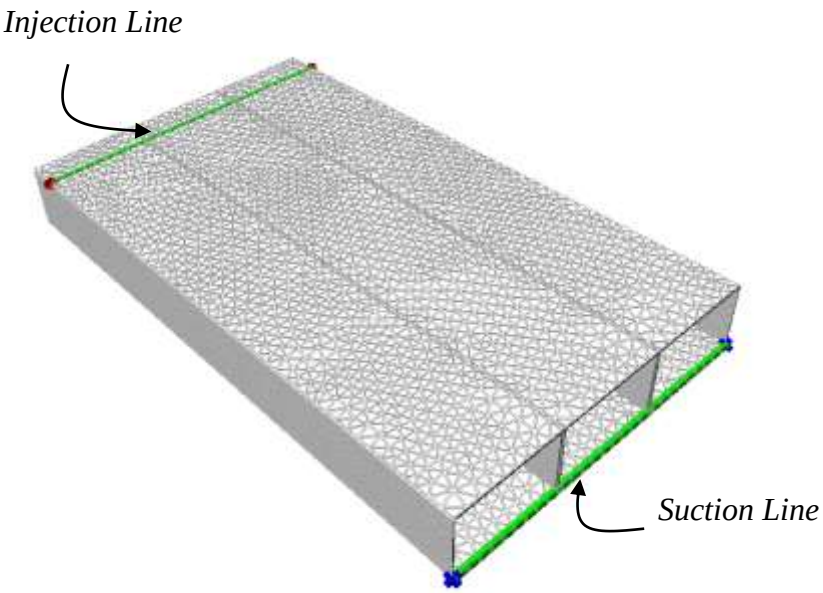

Figure 96. FEM model of the three-cell box beam

6.1.5. Simulation Properties

As illustrated in Figure 54, five different simulation models are constructed in RTM-Worx simulations. Note that NINR model uses Arrhenius viscosity model, whereas three different viscosity models including Arrhenius, Castro – Macosko, and Lee – Han are employed in NIR model simulations.

The properties of simulations are tabulated in Table 20. Preform thermal and resin cure kinetics are identical to those used in Chapter 4 and are given in Table 13 and Table 16 respectively. Resin thermal properties, on the other hand, need to be changed for the process temperature, 40 ˚C. Table 21 presents the resin thermal properties that are used in RTM-Worx simulations.

Table 20. RTM-Worx Simulation Properties

Resin Inlet Temperature	40 ˚C
Mold Temperature	12 ˚C
Pressure Difference	97325 Pa
Resin Viscosity in the isothermal model (at 40˚C)	0.24 Pa.s
Viscosity non-isothermal model (Arrhenius Model)	$\mu = 7.431x10^{-8}e^{4731.8\left(\frac{1}{T}\right)}$
Viscosity non-isothermal cure-dependent model (Castro-Macosko Model)	$\mu = 7.431x10^{-8}e^{4731.8\left(\frac{1}{T}\right)}\left(\frac{\alpha_{gel}}{\alpha_{gel}-\alpha}\right)^{-11.133+83.648\alpha}$
Viscosity non-isothermal cure-dependent model (Lee-Han Model)	$\mu = 7.431x10^{-8}e^{4731.8\left(\frac{1}{T}\right)}e^{(-0.479+\frac{1.432}{T})\alpha}$

Table 21. Resin thermal properties

Property	Value	Reference
Resin density (at 23˚C)	1100 kg/m^3	[25]
Resin density (at 40˚C)	1098.5 kg/m^3	[45]
Resin specific heat (at 40˚C)	1400 J/kg.˚C	[46]
Resin conductivity (at 40˚C)	0.2 W/m.˚C	[47] and [48]

6.1.6. Thermal Boundary Conditions of Non-Isothermal Simulations

The following assumptions are made for thermal boundary conditions.

- The temperature of surrounding air was measured as 12˚C and not a significant change was sensed during the process. Hence, the temperature of surrounding air is assumed to be constant in non-isothermal simulations.
- Mold surface temperature is set equal to the temperature of surrounding air.
- The temperatures of injection gates are set equal to the resin temperature and are assumed to be constant throughout the process.
- Radiative heat transfer is omitted.
- Air is assumed to be an ideal gas.
- Air is considered as incompressible with constant properties.

- Convection heat transfer coefficient differs throughout the body. Considering the geometry shown in Figure 97 as a hot plate, airflow can be assumed as buoyancy-driven flow in a horizontal plate. In this case, buoyancy is generated by the density gradient within in the air. The density gradient of air is caused by the temperature change around the body and therefore buoyancy-driven flows are generated as presented in Figure 98.

  Surface heat loss occurs by free convection from the vertical side and horizontal top and bottom surfaces. Nusselt number defines the ratio of convective and conductive heat transfer across the boundary and has the following relation.

$$\overline{Nu_L} = \frac{\bar{h}L}{\lambda} \tag{127}$$

  For a laminar free convection, empirical formulations of Nusselt numbers are derived for various geometries in the reference [55]. Side webs can be considered as vertical plates and for a laminar free convection on a hot vertical surface, the empirical Nusselt number is as follows.

$$\overline{Nu_{L_{side}}} = 0.68 + \frac{0.670\ {R_{a_L}}^{1/4}}{[1 + (0.492/Pr)^{9/16}]^{4/9}} \quad (R_{a_L} \leq 10^9) \tag{128}$$

  Horizontal top and bottom surfaces have different conditions as shown in Figure 98. For the top surface of a hot plate, the empirical Nusselt number is as such.

$$\overline{Nu_{L_{top}}} = 0.15\ {R_{a_L}}^{1/3} \quad (10^7 \lesssim R_{a_L} \leqq 10^{11}) \tag{129}$$

For the bottom surface of a hot plate, the Nusselt number is below.

$$\overline{Nu_{L_{bottom}}} = 0.52\, {R_{a_L}}^{1/5} \quad (\, 10^4 \lesssim R_{a_L} \leqq 10^9, Pr \gtrsim 0.7\,) \tag{130}$$

Rayleigh number is a dimensionless number that designates the form of heat transfer, either conduction or convection, in the buoyancy-driven flow. Rayleigh number of air along the characteristic length is evaluated from the below equation. Average surface temperature is assumed as 30 ˚C by considering the fact that preheated resin cools down as contact with the preform.

$$R_{a_L} = \frac{\rho g \beta (T_s - T_{air}) L^3}{\mu \kappa} \tag{131}$$

Average convection heat transfer coefficient has the following relation and can be evaluated using thermophysical properties of air at 12˚C ($\rho_{air,12^\circ C} = 1.2314\ kg/m^3$, $\mu_{air,12^\circ C} = 177.1\ x10^{-7}\ N.s/m^2$, $\kappa_{air,12^\circ C} = 20.52\ x10^{-6}\ m^2/s$, $Pr_{air,12^\circ C} = 0.7109$, $\beta_{air,12^\circ C} = 0.0033\ K^{-1}$, $\lambda_{air,12^\circ C} = 0.0251$).

$$\begin{aligned} \bar{h}_{side} &= \frac{\lambda_{air}}{H}\,\overline{Nu_{L_{side}}} = 5.54\ W/m^2K \\ \bar{h}_{top} &= \frac{\lambda_{air}}{L}\,\overline{Nu_{L_{top}}} = 4.44\ W/m^2K \\ \bar{h}_{bottom} &= \frac{\lambda_{air}}{L}\,\overline{Nu_{L_{bottom}}} = 1.20\ W/m^2K \end{aligned} \tag{132}$$

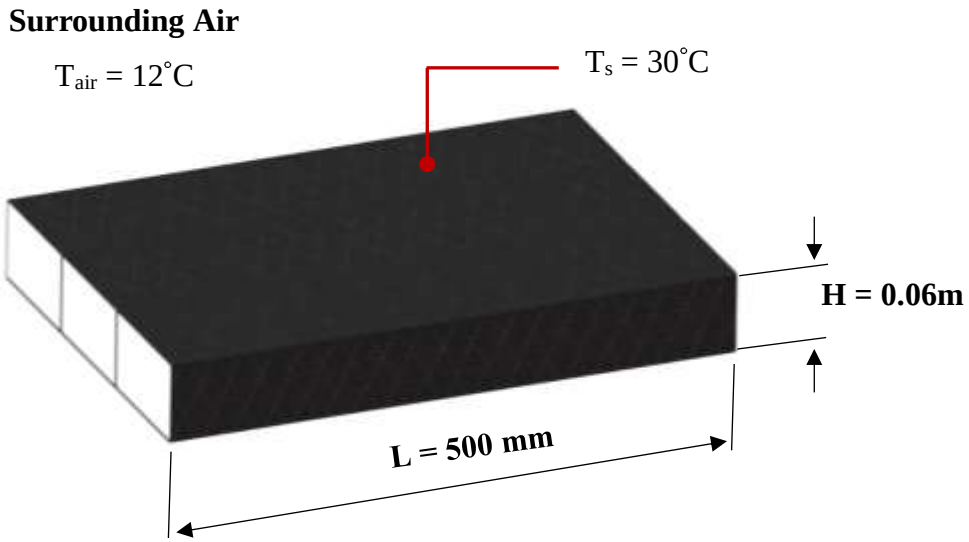

Figure 97. Schematic diagram of the part

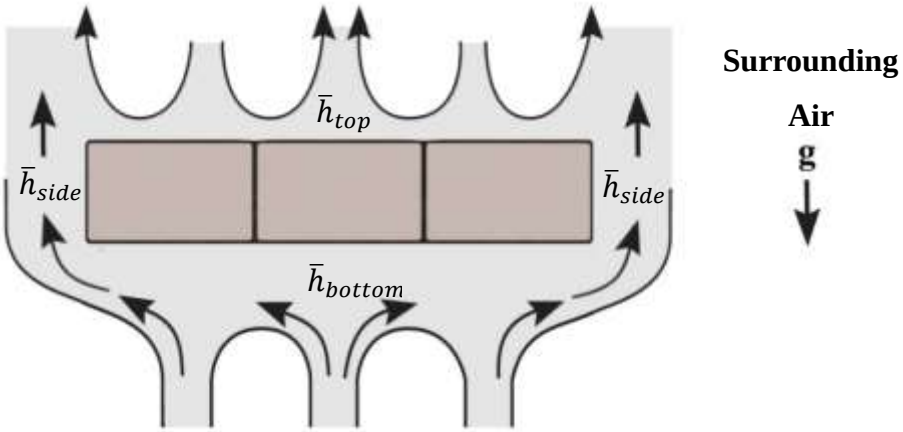

Figure 98. Schematic diagram of buoyancy-driven flows on the part

6.1.7. Simulation Results

Figure 99 presents the fill time estimations of RTM-Worx simulations. The isothermal model underestimates the exact fill-time. This is due to the fact that resin viscosity decreases as the resin flow propagates. Since the isothermal model cannot account this temperature drop, it is prone to yield lower fill-time results. It can be understood from Figure 99 that all non-isothermal models predict more accurate results compared to isotheral model. As expected, NIR – Lee & Han gives the most accurate among all. Another observation from Figure 99 is that all models are tend to approach to the exact fill-time result, as the number of elements raises.

Fil time percentage error is shown in Figure 100 and it is seen that the isothermal model has a 38% error and underestimates the exact fill time value significantly. One can also see that other four models have very close solutions. However, NIR – Lee & Han model yields the fill time result with just 5% of error.

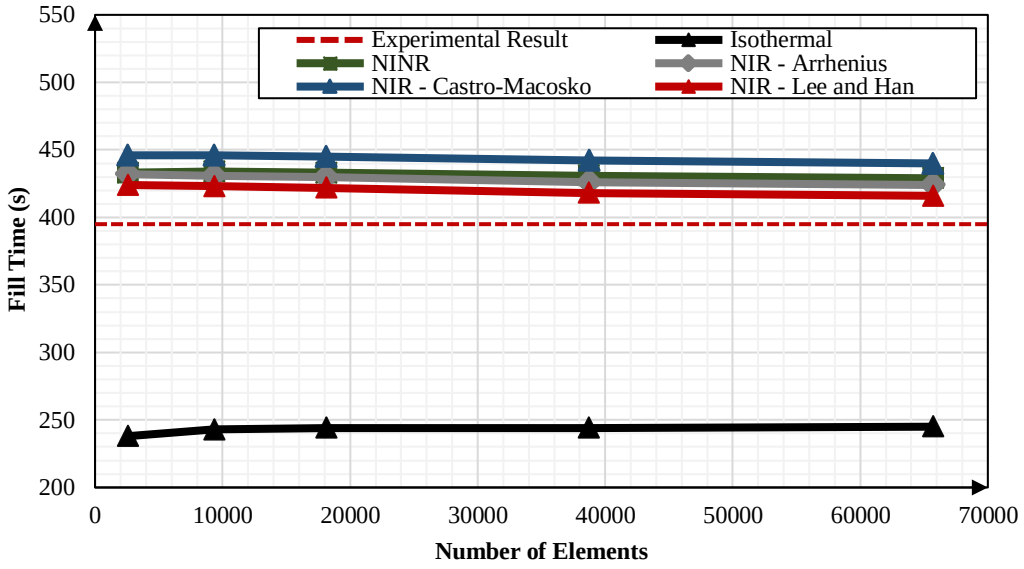

Figure 99. Fill-time results of RTM-Worx simulations

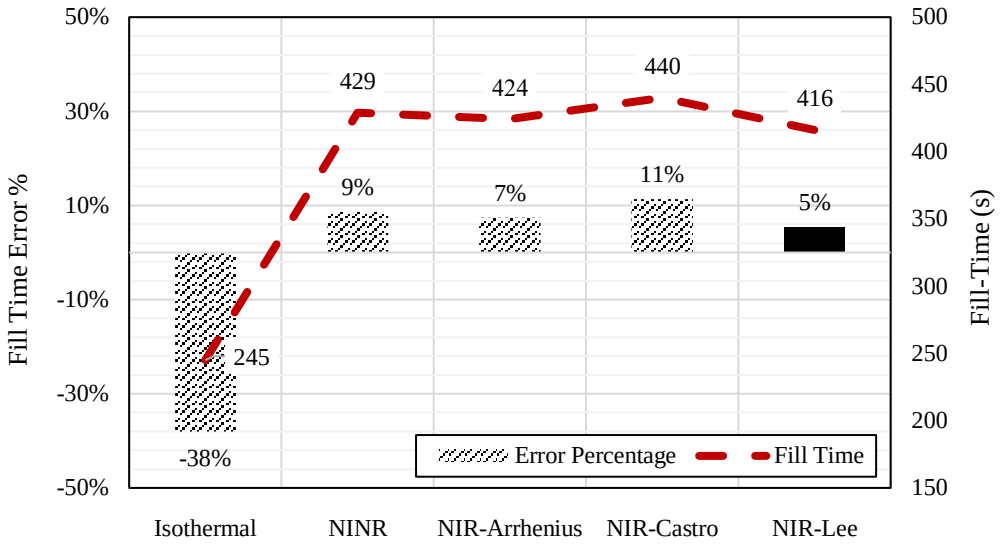

Figure 100. Fill time percentage error of different RTM-Worx Simulations

6.1.8. Simulation vs Experimental Results

Figure 101 shows the predicted and actual flow front locations. It can be seen that simulated flow front locations are in good agreement with the experimental results.

The total fill time calculated by NIR – Lee & Han model is 416 s and is just 5% off from the actual fill time. In addition to that, no dry spot is estimated by simulation and as expected, a dry spot is not observed in the experiment.

Slight lead-lag between the top and bottom skins is observed. Considering the injection strategy, there can be two possible reasons for that: (1) Suction is applied from the lower surface. (2) Since the resin feed line is positioned on the top skin, the resin is forced to travel around the three molds, which are wrapped with preform.

Time	VARTM (Total Fill-Time : 395s)	RTM-Worx (Total Fill-Time : 416s)
10s	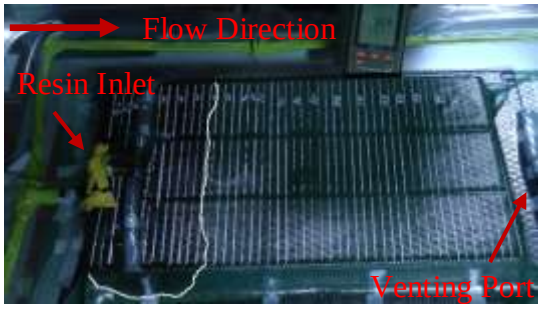	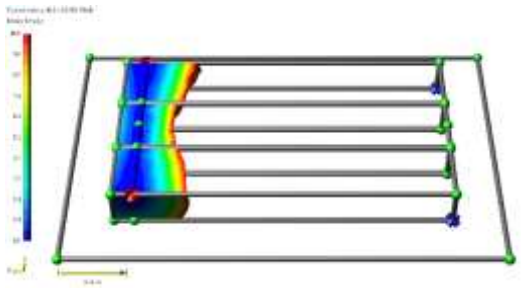
30s	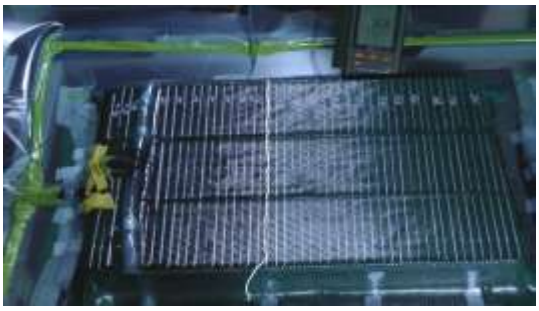	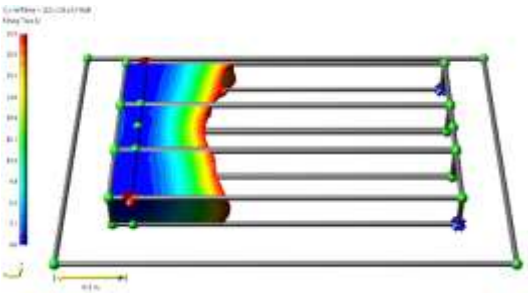
120s	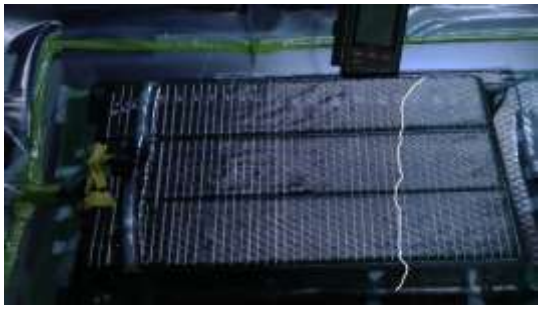	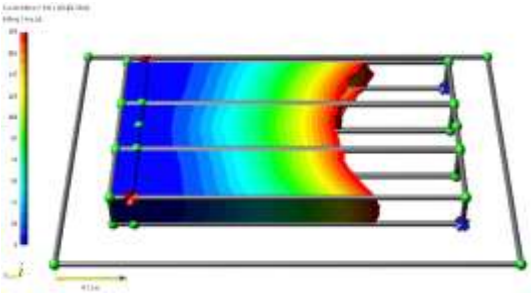

Figure 101. Experimental and simulation flow front during the process

Time	Infusion	RTM-Worx
180s		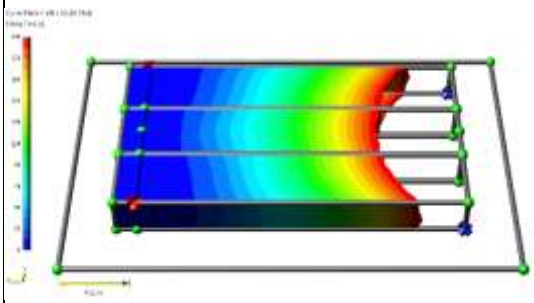
300s	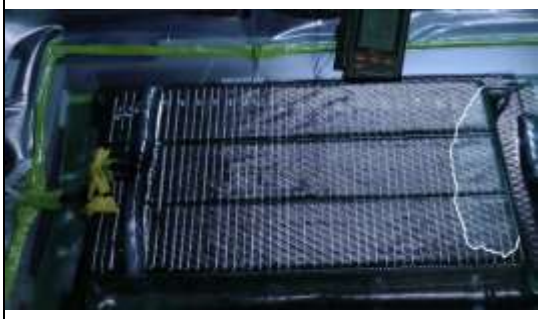	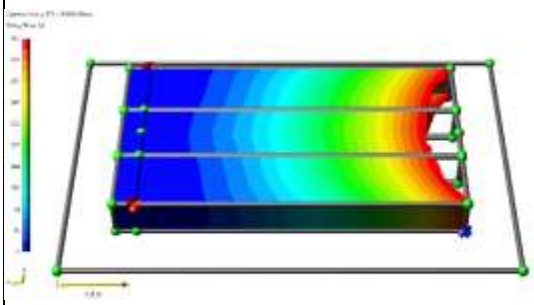
375s		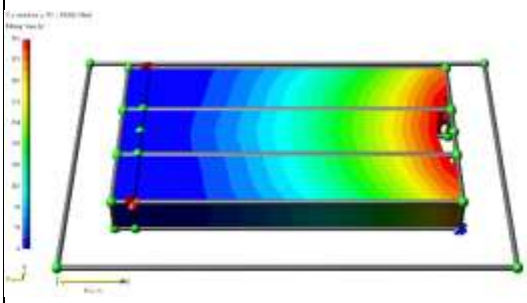

Figure 101 (cont'd). Experimental and simulation flow front during the process

6.2. COMPARISON OF MECHANICAL PROPERTIES

6.2.1. Four-Point Bending Test

Having completed the manufacturing of co-cured and secondary bonded parts, the comparison of mechanical behavior is intended. Bending test is highly preferable for an element level structural test of stiffened aeronautical structures because the part is both subjected to compressive and tensile stress, which represents fracture in a wider spectrum.

For a box beam structure, especially secondary bonded, debonding is highly critical in skin-web integrations and might cause premature failure. There are two standardized version of bending tests for fiber-reinforced composites: (1) three-point bending (2) four-point bending. Four-point bending has several advantages over three-point bending:

- In the four-point bending, the volume under stress is higher than that of three-point bending. Statistically, this allows finding a crack or flaw in part with higher probability.
- The peak stress in the four-point bending is extended along the span, whereas the peak stress produced in the three-point bending is a concentrated point-contact. From the statistical point of view, exposing the peak stress at more extended area might increase the chance to detect flaws.
- Fiber-reinforced composites are prone to premature failure owing to their brittle characteristic. Four-point bend test prevents the material from premature failure since the peak stress is distributed over the span. Hence, four-point bending is desirable for fiber-reinforced composites, while three-point bending is preferable for plastics.

Additionally, various authors have preferred to subject four-point bending test for similar applications. Kruger et al. investigated the debonding in composite skin/stringer and concluded that four-point bending is proved to study the debonding for that kind of applications [56]. Bertolini et al. researched on the composite co-cured and bonded stiffened parts and preferred to perform four-point bending [57].

ISO 14125 is a standard to specify test methods to determine the flexural properties of fiber-reinforced composites. Even though this standard is intended to determine properties for a lamina or laminate, there is no standardized method for structural bending tests and the same procedure is followed in this study [58].

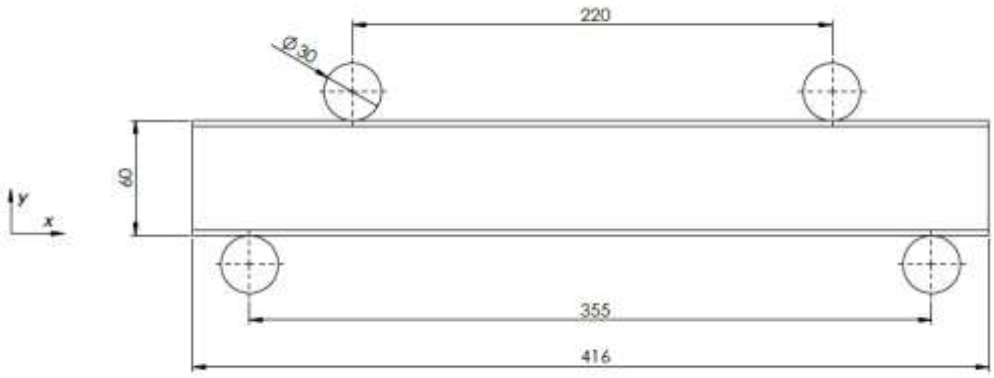

Figure 102. Schematic of four-point bending test

The schematic of bending test is shown in Figure 102. The inner span of the set-up is 220mm, the outer span is 355mm and the roller diameter is 30mm, as shown in the figure. The speed of testing is determined based on ISO 14125, using the following formula. The principle in selecting the test speed is to make strain rate 0.01 as close as possible.

$$N_{test} = \frac{\varepsilon' L^2}{4{,}7h} \tag{133}$$

6.2.2. Secondary Bonded Part Test

Secondary bonded part is first tested and the test set-up is shown in Figure 103. The test is recorded by video camera during the test in order to better observe the failure modes. Two strain gauges are mounted on the side webs. Strain gauges are positioned so that they are parallel to the center axis of mobile rollers. Figure 104 and Figure 105 presents the location of strain gauges S1 and S2. The test speed is evaluated by using Equation (133). Strain rate is selected as 0.01, while thickness and span lengths are 60mm and 355mm respectively. The test speed is eventually found as 4.5 mm/min.

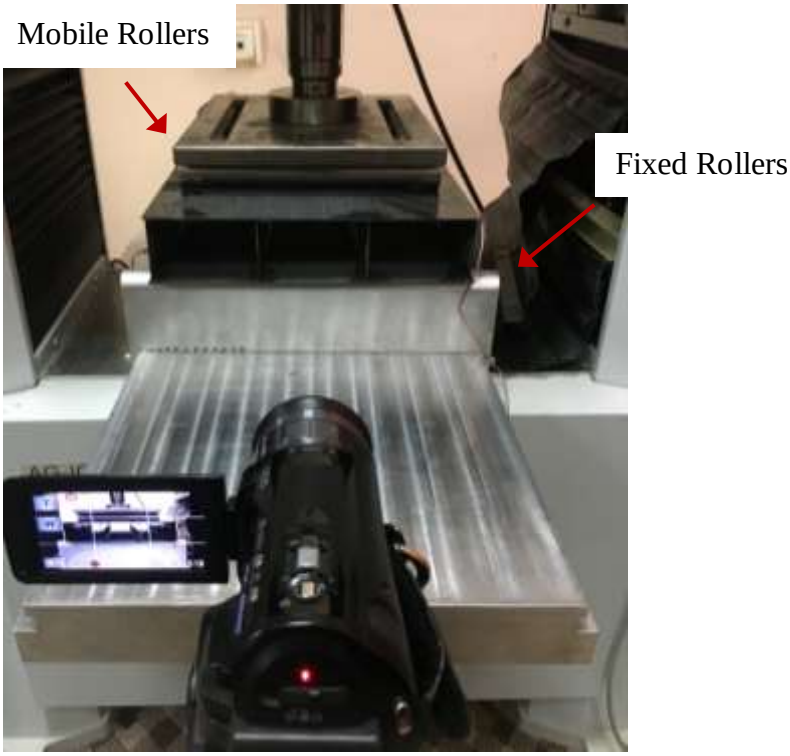

Figure 103. Secondary bonded part bending test set-up

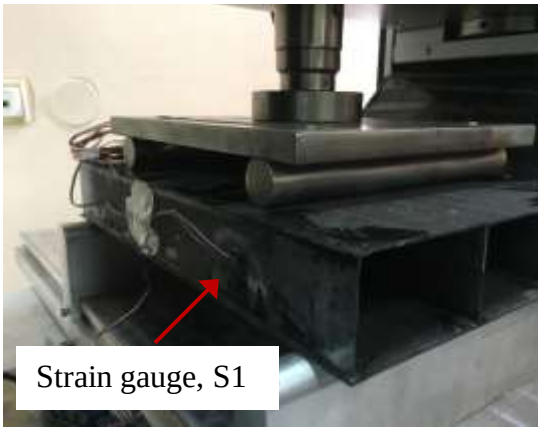

Figure 104. Strain gauge (S1) location

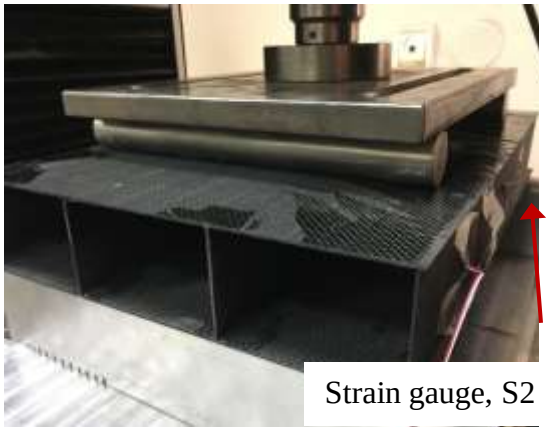

Figure 105. Strain gauge (S2) location

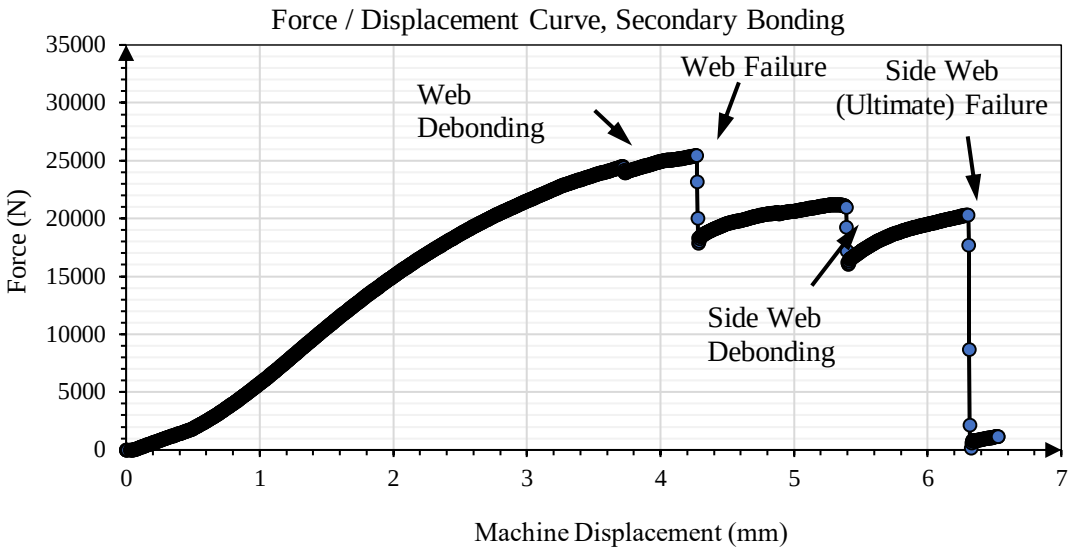

Figure 106. Force / Displacement Curve, Secondary Bonding

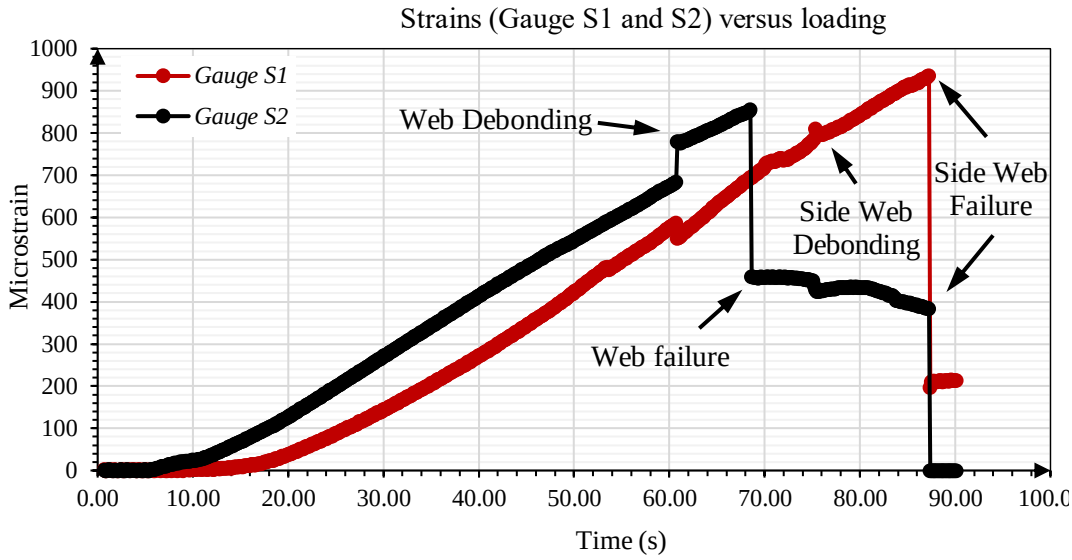

Figure 107. Strain history during the test

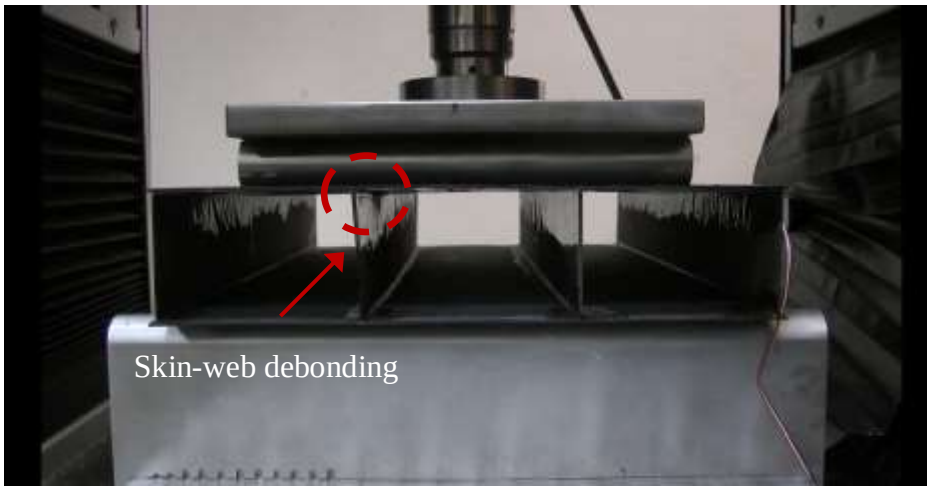

Figure 108. Skin-web debonding

The force versus roller deflection curve is shown in Figure 106. The first phase corresponds to the quasi-linear behavior of the test part. The first phase is ended up with web debonding, i.e. presented in Figure 108. Skin-web debonding appeared at 24.5 kN loading. Subsequently, the web is failed at 25.5 kN and it is presented in Figure 109.

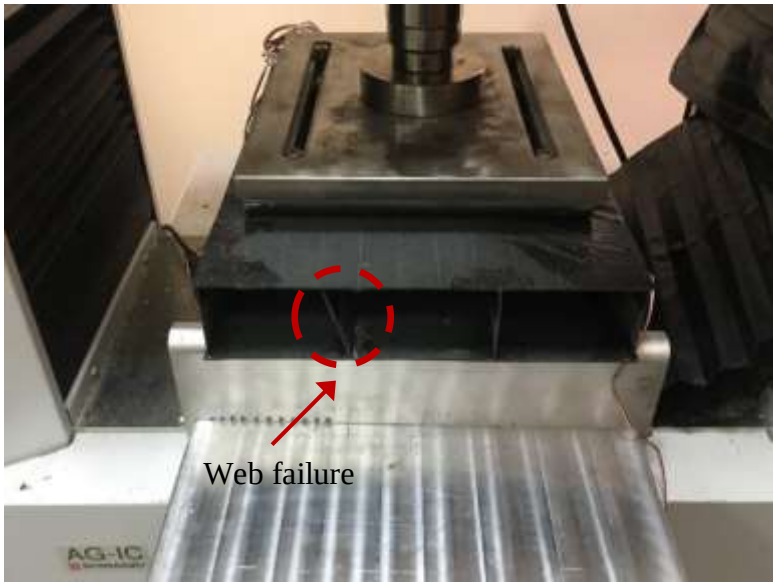

Figure 109. Web failure

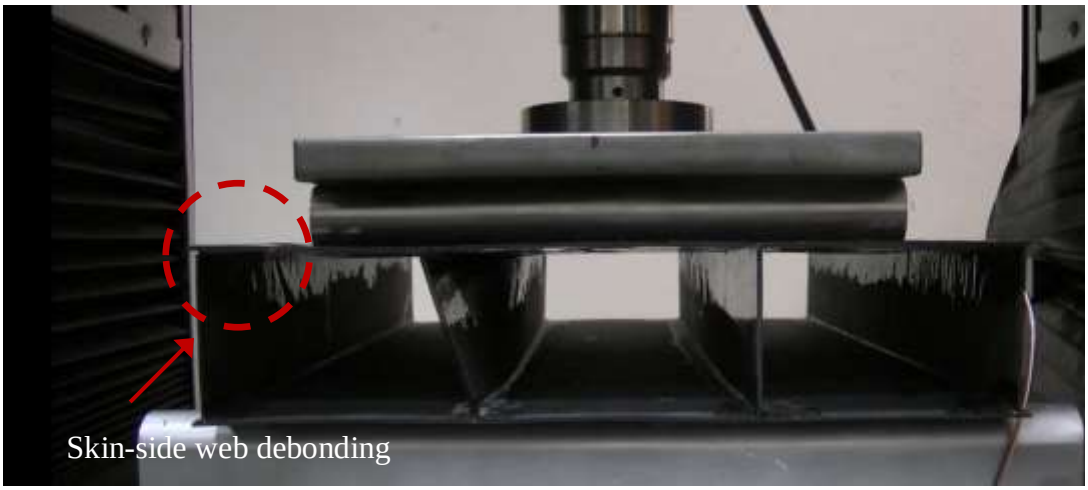

Figure 110. Skin-side web debonding

After web failure, the load is continued to go up until the point 21.1 kN, where debonding between skin and side web is observed. Figure 110 presents the onset of skin-side web debonding. The part is eventually failed at 20.3 kN loading and the ultimate failure is caused by side web breakage. The ultimate failure is shown in Figure 111.

Figure 111. Side web (Ultimate) failure

6.2.3. Co-cured Part Test

Co-cured part is next tested and the test set-up is seen in Figure 112. Again, the test is recorded by a video camera in order to observe the failure modes. Two strain gauges are mounted on the side web. It was indented to mount the strain gauges in the same configuration as in the previous test, however, strain gauges did not respond very well because of excessive background noise. Therefore, they had to mount on the left side web.

In the gauge mounting operation, the target surface is required to be ground first. P150 sandpaper is used to do. A strain gauge has adhesive band on its surface and it can easily adhere on rough surfaces. For a complete cure of the gauge adhesive, 6 hours is required. Having adhered a gauge, next step is to braze the electrical wires. A special care has to be taken in this operation because improper brazing operation comes with additional background noise in the test. Strain gauge brazing operation is seen in Figure 115 and the location of gauges are presented in Figure 116.

The test speed is again calculated using Equation (133). Thickness and span length are selected as 60mm and 355mm respectively. The test speed is found as 4.5 mm/min to make strain rate 0.01.

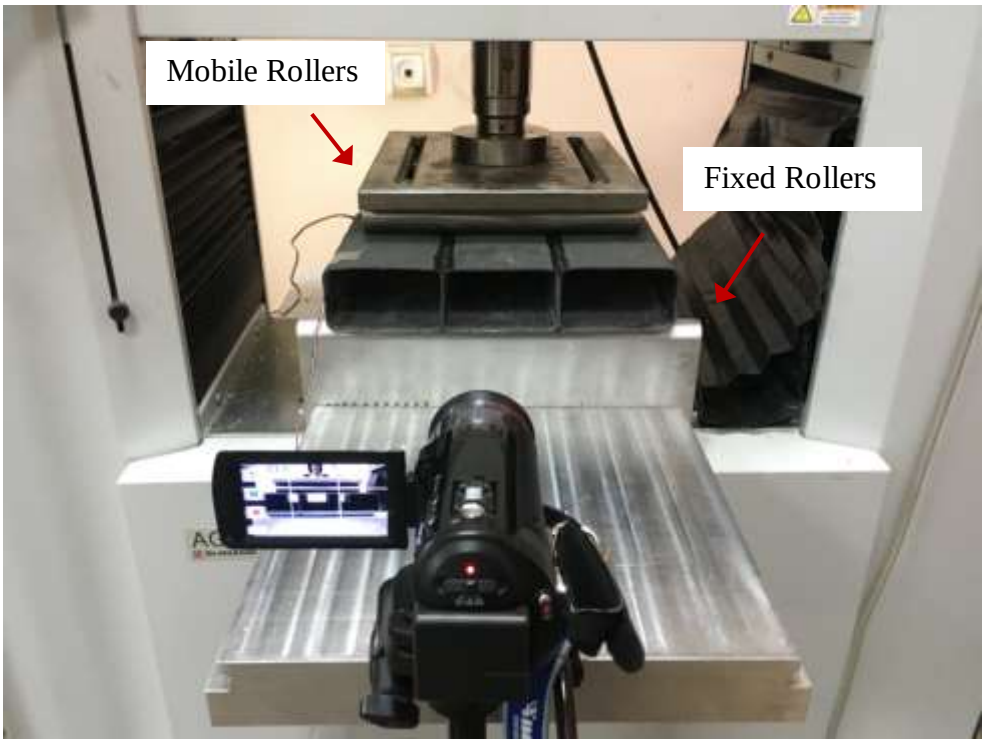

Figure 112. Co-cured part bending test set-up

The force versus roller deflection is shown in Figure 113. Force/displacement has a quite large area of non-linear behavior. The following reasons might cause such non-linear behavior:

- The length of mobile rollers is smaller than the width of the part, which causes compressive loading in the vicinity of roller tips. Thus, a crack might be initiated from those regions, which may lead a complicated failure.
- Large deformations might be occurred due to the nature of geometry.
- Microcracks are generated within the material, which cannot be sensed. Basically, those cracks could change the stiffness of material throughout the test and therefore cause a non-linear deformation response.

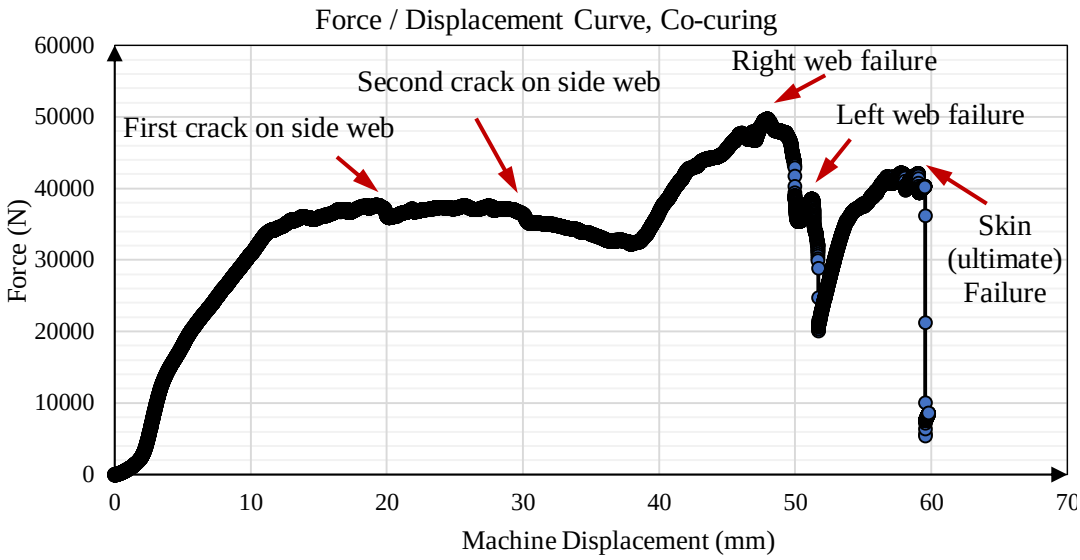

Figure 113. Force / Displacement Curve, Co-curing

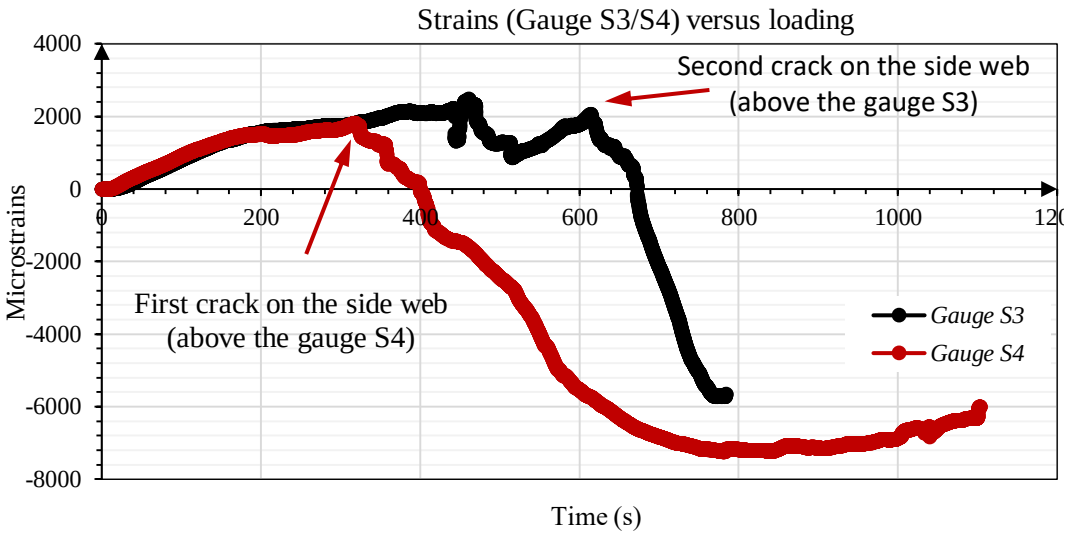

Figure 114. Strain history during the test

Figure 115. Strain gauge mounting

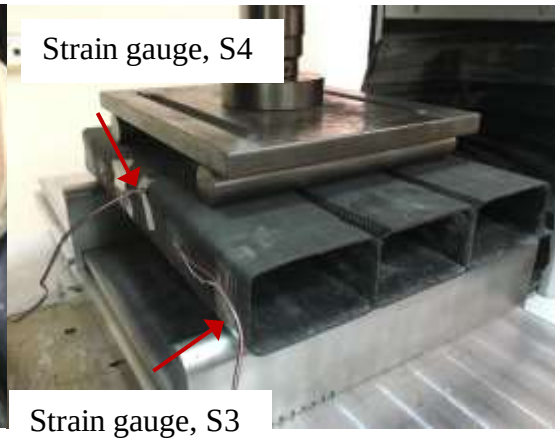

Figure 116. Strain gauges (S3 and S4) locations

The first crack is initiated on the left-side web, i.e. seen in Figure 117, while the small decrease in the slope of the force/displacement curve is observed. At this point, the force is measured as 37.4 kN. Then a second crack is initiated on the right-side web and the sensed force is 36.7 kN. Figure 118 presents the crack initiation on the right-side web. Increasing the load propagates theses cracks.

Figure 117. First crack in left-side web

Figure 118. First crack in right-side web

Figure 119. Right web failure

Figure 120. left web failure

The maximum load is observed at the onset of right web failure, which is 49.7 kN. The right web failure is shown in Figure 119. The left web failure is noticed where the load is 38.5 kN, which is shown in Figure 120. The load is started to increase at this point. The ultimate failure is caused by the bottom skin breakage, which is subjected to tensile loading. The ultimate failure is occurred at 40.3 kN and is seen in Figure 121 and Figure 122. Figure 123 presents the failed co-cured part.

Figure 121. Ultimate skin failure

Figure 122. Ultimate skin failure

Figure 123. Failed part

6.2.4. Comparison of Experimental Results

Table 22 presents the comparison of bending test results. The first test took quite shorter than the second and the deformation observed in secondary bonded part was lower. This is due to the fact that the integrations in secondary bonded part are weaker than that of co-cured. This finding also explains the debonding failure occurred in secondary bonded part. As a result of stronger integration, the maximum load observed in co-cured part was 49.7 kN, which was 25.5 kN for the secondary bonded part. Co-cured part, in other words, withstood 95% higher load than the secondary bonded part. Similarly, the failure load was 40.3 kN for the co-cured part, whereas it was 20.3 kN for the secondary-bonded part. In the light of this analysis, it is clear that the co-cured part exhibited increased mechanical performance than the secondary bonded part.

Table 22. Comparison of four-point bending test results

-	Secondary Bonded Part	Co-cured Part	Increase %
Maximum Load (kN)	25.5	49.7	95%
Failure Load (kN)	20.3	40.3	99%

6.3. COMPARISON OF ENERGY CONSUMPTION

Energy intensities of manufacturing techniques are described in Section 1.2. In this section, energy consumptions of two techniques used in the study are examined and compared. The energy consumption during the process is assumed to be in the form of electrical energy and thus only electrical energy consumptions are taken into consideration. There are three sources of energy consumption: (1) convection oven, (2) vacuum pump, (2) diamond saw. Processes have different sub-operations and the time and energy consumption among them are mostly different.

The energy consumed by the vacuum pump is directly proportional to its usage, as no shut-off controller is present. Therefore, the total consumption is calculated by simply multiplying the power of pump and usage. The same method is also applicable to the diamond saw consumption.

In the convection oven, on the other hand, the controller actively shuts-on or -off the device according to the measured and target temperature values. To count the consumed electrical energy accurately, Köhler three-phase electrical meter was connected to the oven and the consumed electrical energy before and after the curing process was measured.

Figure 124 shows the electrical meter before the oven was turned on and the starting value was measured as 0.25 kW.h. After 8 hours curing operation, electrical consumption was sensed as 7.26 kWh, i.e. seen in Figure 125. Hence the electrical consumption was calculated as 7.01 kW.h for 8 hours operation and then the electrical intensity of oven was evaluated as 3155 kJ/h.

Figure 124. Photograph of electrical meter before oven was turned on

Figure 125. Photograph of electrical meter after the curing process

Figure 126 presents the energy consumptions in co-curing process. It is shown that highest amount of energy was consumed in the foam mold preparation operation. Curing operation consumed the second most energy in the process. The reason for this is that convection oven has the highest energy intensity and causes the major portion of consumption in the process.

Energy consumption of secondary-bonding process is shown in Figure 127. The significant amount energy was consumed in curing operations of the secondary-bonding process. Similar to the co-curing process, this is because convection oven has the largest energy consumer in the process.

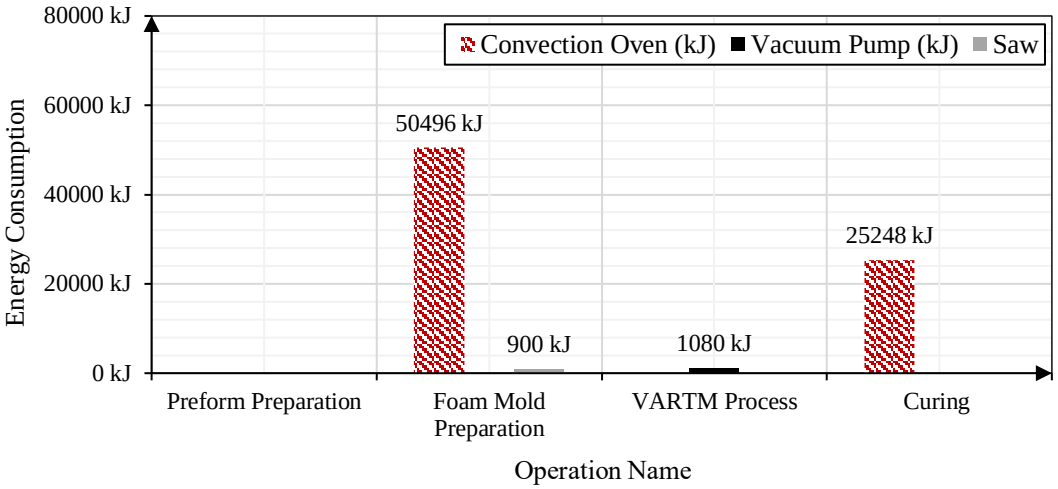

Figure 126. Energy Consumption of Co-curing Manufacturing

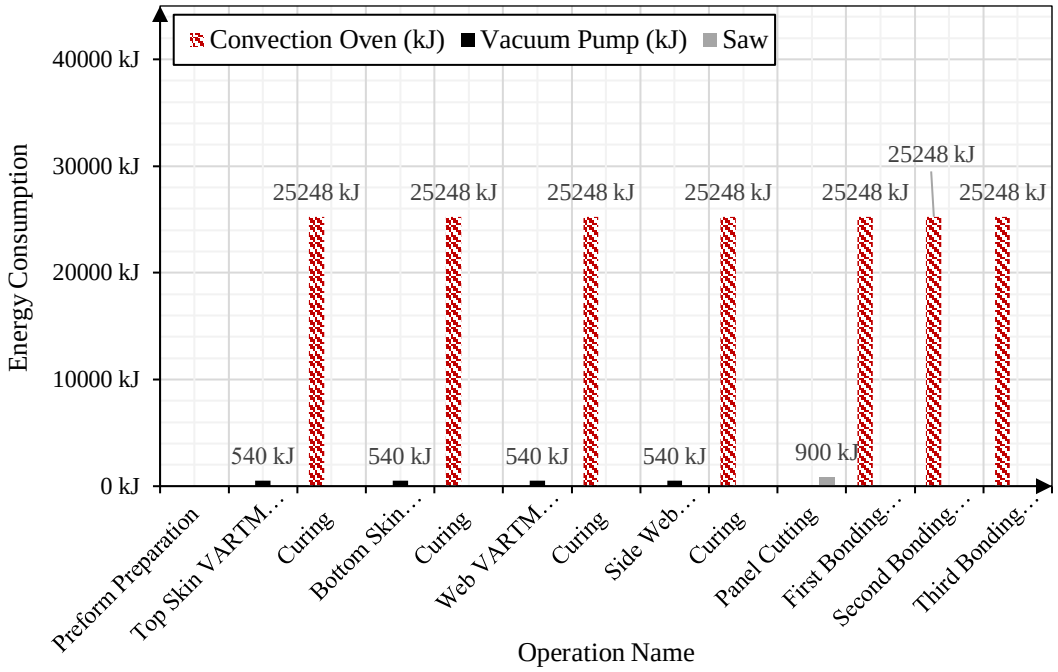

Figure 127. Energy Consumption of Secondary-bonding Manufacturing

The labor time of the co-curing and secondary bonding processes is given in Appendix D. The labor time represents the working time of two people. Totally 4.5 h was consumed in the process and the predominant amount of time was spent in the infusion operation. In contrast, 6 hours was spent in the process and again the significant portion of time was spent in infusion operations. Comparing two processes, it can be seen that co-curing demands less labor time. This is mainly because of the additional bonding operations in the secondary-bonding.

As summarized in Figure 128, energy spent in the co-curing process was 78 MJ, whereas 180MJ was consumed in the secondary bonding process. In other words, 57% of energy could be saved for manufacturing three-cell box beam by using the co-curing process. Additionally, total labor time spent in the co-curing process was 4.5h, while it was 6h in the conventional method. Hence, it can be concluded that co-curing process can save 25% labor time compared to the conventional technique.

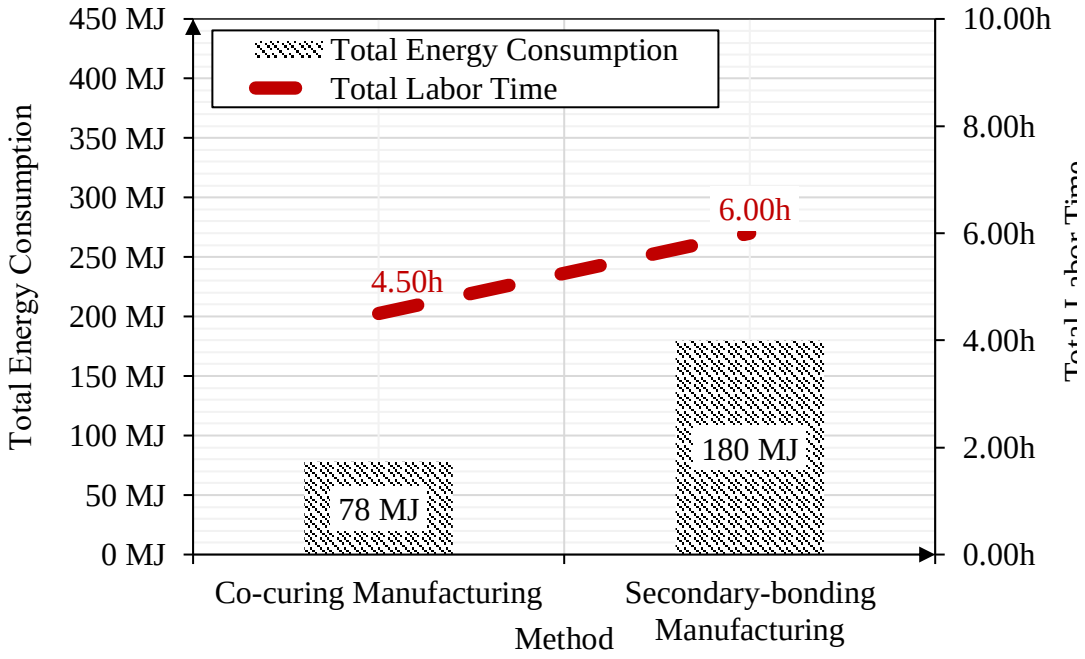

Figure 128. Comparison of Co-curing and Secondary-bonding manufacturing methods

CHAPTER 7

SUMMARY AND CONCLUSIONS

In this study, a low-cost co-cured manufacturing technique has been developed for stiffened shells of aircraft structures, particularly multi-cell box beams. Resin impregnation simulations have been performed to better understand the process and predict the fill-time. The process has been enhanced by studying the critical process parameters, foam material, foam strength, curing operation and foam coating. Beyond the objective of developing a co-cured manufacturing technique, the study is aimed a wider goal to provide extensive data for composite manufacturing simulation tools. Hence, the three-fold approach is followed in this study.

1. First, extensive characterization of preform and resin are made to use in the resin impregnation simulations. The accuracy of simulation results is strongly dependent on the accuracy of material characterization results.

2. Second, resin impregnation simulations using RTM-Worx are performed by using the material data acquired in the first part. Various simulation models including isothermal, non-isothermal non-reactive, non-isothermal reactive, are generated to accurately estimate the fill-time in the process.

3. Third, proposed low-cost manufacturing technique is used to produce the co-cured part. To better analyze the co-cured part, conventional secondary-bonded part is manufactured. The co-curing technique is compared with the conventional method from both manufacturing and final part mechanical properties perspectives.

In the first part of the study, the following conclusions have been drawn.

- Effect of shear rate on resin viscosity was investigated and flow sweep test was carried out. The viscosity of neat resin remained unchanged under shear rate up to 200 1/s and exhibited Newtonian fluid characteristics, as reported in literature [22].

- The temperature effect on neat resin viscosity was analyzed by conducting temperature sweep test using rheometer. The viscosity of the neat resin is strongly dependent on temperature and even 5°C increase in temperature yielded a 40% decrease in the resin viscosity, which is presented in Figure 23. This leads the conclusion that one needs to be cautious to make constant viscosity assumption in resin impregnation simulations.

- The curing effect was thoroughly analyzed in Section 2.2.4. Temperature sweep test was carried out for resin with catalyst. Viscosities of neat resin and resin-catalyst mixture were compared and presented in Figure 26. It was shown that resin-catalyst mixture has lower viscosity than neat resin.

- Since the temperature dependence of viscosity is coupled with degree of cure, chemorhelogy models were created for the resin-catalyst mixture. Castro-Macosko and Lee & Han non-isothermal cure-dependent models were constructed and were presented in Table 6.

- Porosity tests of VARTM process consumables - distribution media and peel ply - and carbon fiber preform were carried out. Porosity tests were repeated under different vacuum levels. The porosity values with respect to vacuum level were measured and were presented in Figure 37. It was concluded that porosity decreases up to 15% from 13000 Pa vacuum to 93325 Pa vacuum.

- Effect of stacking the preform on carbon fiber porosity was analyzed and porosity of two, five, seven and ten layers carbon fiber reinforcement stacks were measured. A tendency to decrease in porosity was observed as the fabric count increases. A curve-fit equation was derived for the stacking effect and was presented in Figure 35. 17% drop in porosity was measured from 2-layer stacking to 10-layer stacking.

The following conclusions have reached in the second part of the study.

- 1D resin impregnation model of VARTM process was constructed and the effects of varying thickness and pressure profile in VARTM on fill-time were investigated. The so-called coupled formulations, which consider the change in thickness and pressure profile, and uncoupled formulations were solved numerically. The-fill time results were compared with the experimental results. The analysis leads the conclusion that uncoupled formulations does not make substantial fill-time error by assuming non-varying thickness and uniform pressure distribution in VARTM process.

- In the light of analysis carried out in Chapter 3, it was concluded that selecting the proper resin viscosity model is more effective on the accuracy of fill-time solution than implementing a coupled formulation. Hence, special care needs to be taken to find the suitable resin viscosity model in resin impregnation simulations.

- Five different simulation models were constructed in RTM-Worx simulations and the model structure was given in Figure 54. To choose the appropriate resin viscosity model and verify the accuracy of RTM-Worx flow model for use in VARTM, a validation experiment was conducted. The validation analysis leads to the following conclusions:

    - The isothermal Model found flow-front results close agreement with the Darcy's Law. However, the model largely overpredicted the flow front. This is due to the fact that the isothermal model does not take into account the temperature and resin reaction effects.

    - All non-isothermal models predicted better results compared to the isothermal model and non-isothermal modes were seem to be more accurate than the isothermal model.

    - Among all models, NIR-Lee & Han yielded the solution close agreement with the experimental results and the predicted fill-time was just 2% off the actual result.

    - The coupled fill-time solutions, which consider the varying thickness and pressure profile in VARTM process, were compared with RTM-Worx Simulations. It was observed that RTM-Worx, NIR – Lee & Han model, yields significantly more accurate results compared to the coupled fill-time results.

Following conclusions have been reached in the third part of the study.

- Foam material, foam strength, curing operation and foam coating are considered to be critical process parameters and the co-curing process have been improved by optimizing these parameters.

- Foams were used as a removable mandrel in the process. PS foam was selected owing to its sufficient compressive strength, solubility in a solvent and good surface finish. XPS was preferred over EPS, since XPS has higher stiffness, better surface finish, and better solubility.

- In the first curing cycle that was 100˚C at 5 hours, foams highly degenerated during the process. Foams were not melted in second curing cycle, i.e. 80 ˚C at 8 hours, but the optimum result was achieved at 40 ˚C at 8 hours.

- Two version of foams [53], [54] were used in experiments. The first foam type that has 100 kPa compressive strength could not preserve its stability under vacuum pressure and caused fiber buckling in part, i.e. seen in Figure 74. On the other hand, it was observed that second type foam that has 300 kPa was remained structurally stable and was desirable to use for the co-curing process.

- It was seen that coating foam with epoxy resin ameliorated the impermeability of PS foams low viscosity resin. Foam coating furthermore enhanced the surface hardness of foams and gave additional resistance against the collapse pressure. Additionally, this treatment improved the surface smoothness.

- An optimum result was achieved by using Wallboard XPS 2500X [54] with double coating and subjecting to 80 ˚C at 8 hours curing cycle.

- RTM-Worx resin impregnation simulations for co-cured three-cell box beam were compared with the experiment results. As concluded in the validation analysis in Chapter 4, the isothermal model found the least accurate result with the error percentage of 38%. On the contrary, non-isothermal models yielded the fill-time results having up to 11% of error. This finding confirms that non-isothermal models are more accurate than the isothermal model.

- Among the RTM-Worx simulation models, NIR-Lee-Han model achieved the best fill-time result with just 5% of error. The total fill time of experiment was 395s, whereas NIR-Lee-Han model predicted as 416s. This result confirms the results obtained in Chapter 4.

- RTM-Worx simulations for co-cured three-cell box beam yielded flow front results close agreement with the experiment. The flow front at different time steps is presented in Figure 101.

- In the co-cured three-cell box beam experiment, slight lead-lag between the top and bottom skins was observed. This is attributed to two reasons: (1) Vacuum was applied from the bottom surface (2) Since the resin feed line was positioned on the top surface, the resin was forced travel around the three molds, which were wrapped with preform.

- To better assess the co-cured three-cell box beam, a part having the same geometry was produced by using conventional method, secondary bonding. Four-point bending testing was performed both for co-cured and secondary parts to compare their mechanical properties. Test results showed that the co-cured part withstood 95% higher load than the secondary-bonded part and the failure load of the co-cured part was 99% higher than that of the secondary-bonded part. In the light of these results, it was concluded that increased mechanical performance can be achieved for three-cell box beam by using the co-cured process.

- The energy consumption of co-curing process was also compared with the conventional technique. It was seen that almost 57% energy saving can be achieved by using the co-curing process.

- In addition to the energy consumption, labor time was also compared between co-curing and secondary bonding processes. For the three-cell box beam application, 25% labor time saving can be obtained by using the proposed co-cured manufacturing technique.

REFERENCES

[1] R. M. Jones, Mechanics of Composite Materials, Philadelphia: Taylor & Francis, 1999.

[2] I. M. Daniel and O. Ishai, Engineering Mechanics of Composite Materials, New York: Oxford University Press, 1994.

[3] D. Gay, S. V. Hoa and S. W. Tsai, Composite Materials - Design and Applications, New York: CRC Press, 2003.

[4] V. Ogale ve R. Alagirusamy, «Textile Preforms for Advanced Composites,» *Indian Journal of Fibre & Textile Research*, pp. 366-375, 2004.

[5] W. Jiang, J. Dong, L. Lou, M. Liu ve Z. Hu, «Preparation and Properties of a Novel Water,» *Journal of Materials Science and Technology*, pp. 270-275, 2010.

[6] Z. Xiao, L. T. Harper, A. R. Kennedy and N. A. Warrior, "A water-soluble core material for manufacturing hollow composite sections," *Composite Structures*, pp. 380-390, 2017.

[7] S. K. Mazumdar, Composites Manufacturing, Boca Raton: CRC Press, 2002.

[8] S. G. Advani and M. E. Sozer, Process Modeling in Composites Manufacturing, New York: Marcel Dekker, 2003.

[9] S. V. Hoa, Principles of the Manufacturing of Composite Materials, Pennsylvania: Destech Publications, 2009.

[10] Y. S. Song, J. R. Youn and T. G. Gutowski, "Life cycle energy analysis of fiber-reinforced composites," *Composites: Part A*, pp. 1257-1265, 2009.

[11] L. F. Vosteen, "Composites Aircraft Structures," in *Fibrous Composites in Structural Design*, Boston, Springer, 1980, pp. 7-24.

[12] J. C. Watson, "Preliminary Design Development AV-8B Forward Fuselage Composite Structure," in *Fibrous Composites in Structural Design*, Boston, Springer, 1980, pp. 41-61.

[13] M. Kageyama and S. Yoshida, "Development of XF-2 Fighter Composite Structures(cocured composite wings)," in *Proceedings of the 41st structures, structual dynamics, and materials conference and exhibit*, 2000.

[14] G. A. Allen and D. J. Belisario, "Co-cured Composite Structures And Method Of Making Them". US Patent 6,743,504 B1, 1 Jun. 2004.

[15] C. B. Simpson, M. G. Allman, S. T. Tuttle and L. J. Ashton, "Single Piece Co-cure Composite Wing". US Patent 6,889,937 B2, 10 May 2005.

[16] D. L. Engwall and C. J. Morrow, "Co-cured Stringers And Associated Mandrel And Fabrication Method". US Patent 7,293,737 B2, 13 Nov. 2007.

[17] H. Mahruz, P. Majumdar, M. Saha, F. Shamery and S. Jeelanı, "Integral Manufacturing of Composite Skin-Stringer Assembly and Their Stability Analysis," *Applied Composite Materials,* no. 11, pp. 155-171, 2004.

[18] Y. Nagao, Y. Iwahori, Y. Hirano and Y. Aoki, "Low Cost Composite Wing Structure Manufacutring Technology Development Program in JAXA," in *16th Interntational Conference On Composite Materials*.

[19] S. Tatum, "VARTM cuts costs," *Reinforced Plastics,* vol. 45, no. 5, p. 22, 2001.

[20] B. R. Bird, W. E. Stewart ve E. N. Lightfoot, Transport Phonemena, New York: Wiley, 1960.

[21] C. D. Rudd, A. C. Long, K. N. Kendall ve C. Mangin, Liquid Molding Technologies, cilt 31, Woodhead Publishling, 1997, pp. 87-97.

[22] S. M. Koefoed, "Modeling and Simulation of the VARTM Process for Wind Turbine Blades," 2003.

[23] J. R. Weitzenböck, Flow Characterization in Resin Transfer Molding, University of Southampton, 1996.

[24] J. C. Dominguez, M. Oliet, M. V. Alonso, F. Rodriguez and B. Madsen, "An exponential chemorheological model for viscosity dependence on degree-of-cure of a polyfurfuryl alcohol resin during the post-gel curing state," in *37th Risø International Symposium on Materials Science*, 2016.

[25] C. 27 12 2017. [Online]. Available: http://www.lindberg-lund.fi/files/Tekniske%20datablad/VAN-XB3486-H-TD.pdf.

[26] J. M. Castro and C. W. Macosko, "Kinetics and Rhelogy of Typical Polyurethane Reaction Molding Systems," *Society of Plastics Engineers (Technical Papers)*, p. 26:434, 1982.

[27] D. H. Kim and S. C. Kim, "Engineering Analysis of Reaction Injection Molding Process of Epoxy Resin," *Polymer Composites,* vol. 8, no. 3, pp. 208-217, 1987.

[28] D.-S. Lee and C. D. Han, "A chemorheological Model for the Cure of Unsaturared Polyester Resin," *Polymer Engineering and Science,* vol. 34, pp. 955-963, 1987.

[29] R. A. Saunders, C. Lekakou ve M. G. Bader, «Compression in the processing of polymer composites 1.A Mechanical and Microstructural study for different glass fabrics and resin,» *Composites Science and Technology,* cilt 59, pp. 983-993, 1999.

[30] International Organization for Standardization, "Uncertainty of measurement — Guide to the expression of uncertainty in measurement (GUM:1995)," 2008. [Online]. Available: https://www.iso.org/standard/50461.html.

[31] B. Chen ve T. W. Chou, «Compaction of woven-fabric preforms in liquid composite molding,» *Composites Science and Technology,* no. 59, pp. 1519-1526, 1999.

[32] B. Chen and T. W. Chou, "Compaction of woven-fabric preforms: nesting and multi-layer," *Composites Science and Technology,* no. 60, pp. 2223-2231, 2000.

[33] T. G. Gutowski, J. Kingery and S. J. Wineman, "Resin Flow/Fiber Deformation Experiments," *Sampe Q,* no. 21, pp. 54-8, 1986.

[34] T. G. Gutowski, T. Morigaki and Z. Cai, "The Consodolidation of Laminate Composites," *J Composites Mater,* no. 21, pp. 650-669, 1987.

[35] F. Robitaille and R. Gauvin, "Compaction of Textile Reinforcements for Composite Manufacturing I-Review of Experimental Results," *Polym Compos,* vol. 5, no. 19, pp. 543-57, 1998.

[36] F. Robitaille and R. Gauvin, "Compation of Textile Reinforcements for Composites Manufacturing. II-Compaction and Relaxation of Dry and H20 Saturated Woven Reinforcements," *Polym Compos,* vol. 5, no. 19, pp. 543-57, 1198.

[37] F. Robitaille and R. Gaurin, "Compaction of Textile Reinforcements for Composite Manufacturing III-Reorganization of the Fibre Network in Woven," *Polym Compos,* vol. 5, no. 19, pp. 543-57, 1998.

[38] F. A. L. Dullien, Porous Media - Fluid Transport and Pore Structure, New York: Academic Press, 1979.

[39] B. R. Gebart, «Permeability of Unidirectional Reinforcements for RTM,» *Journal of Composite Materials* , pp. 1100-1133, 1992.

[40] A. Hammami and B. R. Gebart, "Analysis of the Vacuum Infusion Molding Process," *Polymer Composites,* vol. 21, no. 1, pp. 28-40, 2000.

[41] N. C. Correia, F. Robitaille, A. C. Long, C. D. Rudd, P. Simacek and S. G. Advani, "Analysis of the Vacuum Infusion Moulding Process. I. Analytical Formulation," *Composites Part A: Applied Science and Manufacturing,* no. 36, pp. 1645-1656, 2005.

[42] D. Modi, M. Johnson, A. Long and C. Rudd, "Analysis of pressure profile and flow progression in the vacuum infusion process," *Composites Science and Technology,* vol. 69, pp. 1458-1464, 2009.

[43] A. Koorevaar, "RTM-Worx," 23 December 2017. [Online]. Available: http://www.polyworx.com/.

[44] V. W. Wang, C. A. Hieber and K. K. Wang, "Dynamic Simulation and Graphics for the Injection Molding of Three-Dimensional Thin Parts," *Journal of Polymer Engineering,* pp. 21-47, 1986.

[45] J. Mijovic and H. T. Wang, "Modeling of Processing of Composites. Part II - Temperature Distribution During Cure," *SAMPE Journal,* vol. 24, pp. 42-55, 1988.

[46] L. E. Evseeva and S. A. Tanaeva, "Thermophysical properties of epoxy composite materials at low temperatures," *Cyrogenics*, vol. 35, pp. 277-279, 1995.

[47] Y. Yoshihiro, Y. Hiroaki and M. Hajime, "Effective Thermal Conductivity of Plain Weave Fabric and its Composite Material Made from High Strength Fibers," *Journal of Textile Engineering*, vol. 54, pp. 111-119, 2008.

[48] K. W. Garrett and H. M. Rosenberg, "The Thermal Conductivity of Epoxy-resin/Powder Composite Materials," *Journal of Physics D: Applied Physics*, vol. 7, pp. 1247-1258, 1974.

[49] DowAksa, "3K A-48 Technical Data Sheet," 27 02 2018. [Online]. Available: http://www.dowaksa.com/wp-content/uploads/2017/04/3K-A-38.pdf.

[50] Cytec Engineered Materials, "Thornel VCB-20 Carbon Fibre Cloth Data Sheet," 27 02 2018. [Online]. Available: http://www.matweb.com/search/datasheet.aspx?matguid=f0231febe90f4b45857f543bb3300f27.

[51] Y. El-Hage, S. Hind and F. Robitaille, "Thermal conductivity of textile reinforcements for composites," *Journal of textiles and fibrous materials*, vol. 1, pp. 1-12, 2018.

[52] M. R. Kamal and S. Sourour, "Kinetics and Thermal Characterization of Thermoset Cure," *Polymer Engineering & Science*, vol. 13, pp. 59-64, 1973.

[53] W. I. P. "XPS Tip 1500 TDS," 27 December 2017. [Online]. Available: http://www.wallboard.com.tr/uploads/13/XPS-Tip-1500-Teknik-Ozellikler-.pdf.

[54] W. I. P. "XPS Tip 2500X TDS," 27 December 2017. [Online]. Available: http://www.wallboard.com.tr/uploads/13/XPS-Tip-2500-X-Teknik-Ozellikler-_1.pdf.

[55] F. P. Incropera, D. P. Dewitt, T. L. Bergman and A. S. Lavine, Fundamentals of Heat and Mass Transfer, 7 ed., New York: John Wiley & Sons, 2002.

[56] R. Krueger, M. K. Cvitkovitch, T. K. O'Brien and P. J. Minguet, "Testing and Analysis of Composite Skin/Stringer Debonding Under Multi-axial Loading," *Journal of Composite Materials,* vol. 34, pp. 1263-1300, 2000.

[57] J. Bertolini, B. Castanié, J.-J. Barrau and J.-P. Navarro, "Multi-level Experimental and Numerical Analysis of Composite Stiffener Debonding. Part 1: Non-specific specimen level," *Composite Structures,* vol. 90, pp. 381-391, 2009.

[58] International Organization for Standardization, "Fibre-reinforced plastic composites -- Determination of flexural properties (ISO Standard No. 14125)," 1998.

APPENDIX A – GNU OCTAVE CODE FOR 1D COUPLED AND UNCOUPLED FLOW SIMULATIONS

```
%============================PART I=======================%
%==================UNCOUPLED FORMULATION=============%
%=========================================================%
%Step 1. Set boundary conditions
%=========================================================%
clear;
clc;
Pamb=97325; Pi=Pamb; Pv=0; Lt=0.11;
%=========================================================%
%Step 2. Set resin and preform parameters
%============================Preform======================%
rho_sup=0.2; n=2; rho=1780;
tf=0.0003; Af=0.12; m=24e-3;
vf0=0.2718; B=0.0467;
K=1.58e-11;
dkdp=0;
%============================Resin========================%
%Resin Viscosity
nu0=0.315; Bv=0.00034;
%=========================================================%
%Step 3. Evaluate constant properties
%=========================================================%
visci=nu0*exp(0*Bv);
vfii=vf0*(Pamb-Pv)^B;
phii=1-vfii;
%=========================================================%
%Step 4. Evaluate fill-time
%=========================================================%t
_UC=Lt^2*phii*visci/(2*K*(Pi-Pv)); %nu:constant,
t_UCV=(1/Bv)*log(1/(1+nu0*Bv*(Lt^2*phii/(2*K*(Pv-Pi)))));%nu(t):Iso          time
dependt
%========================PART II========================%
%==================COUPLED FORMULATION=================%
%=========================================================%
%Step 1. Set mesh properties:
%=========================================================%
nnodes=1000; da=1/nnodes; imax=100; tol=1e-6;
%=========================================================%
%Step 2. Set initial and guess values:
```

```
%=========================================================%
%Apply secant method to optimize dPdai to make P=0 at the last node.========%
%For the first node of dP/da, 2 initial guesses, IA & IB, are made.============%
IA=-2; IB=-1;
%======================Start iteration=======================%
for k=1:imax,
%=========================================================%
%Step 3a. Solve dPda for IA:
%=========================================================%
for i=1:nnodes,
  if i==1,
  P=Pi;
  Pc=Pamb-P;
  dPda=IA;
  vf=m/(tf*Af*rho);
  phi=1-vf;
  h=rho_sup*n/(rho*vf);
  dhdp=0;
  else,
  P=P+dPda*da;
  Pc=Pamb-P;
  vf=vf0*Pc^B;
  phi=1-vf;
  h=rho_sup*n/(rho*vf);
  dhdp=-rho_sup*B*Pc^(-B-1)/(rho*vf0);
  dPda=dPda-(da*((dkdp/K)+(((phi+(alph^2))/(h*phi))*dhdp))*dPda^2);
  end
  alph=(i-1)/nnodes;
  end
%=========================================================%
%Step 4a. Compute P_IA
%=========================================================%
P_IA=P+dPda*da;
%=========================================================%
%Step 3b. Solve dPda for IB:
%=========================================================%
for i=1:nnodes,
  if i==1,
  P=Pi;
  Pc=Pamb-P;
  dPda=IB;
  vf=m/(tf*Af*rho);
  phi=1-vf;
  h=rho_sup*n/(rho*vf);
```

```
  dhdp=0;
  else,
  P=P+dPda*da;
  Pc=Pamb-P;
  vf=vf0*Pc^B;
  phi=1-vf;
  h=rho_sup*n/(rho*vf);
  dhdp=-rho_sup*B*Pc^(-B-1)/(rho*vf0);
  dPda=dPda-(da*((dkdp/K)+(((phi+(alph^2))/(h*phi))*dhdp))*dPda^2);
  end
  alph=(i-1)/nnodes;
  end
%=========================================================%
%Step 4b. Compute P_IB
%=========================================================%
P_IB=P+dPda*da;
%=========================================================%
%Step 5. Check the convergence criterion
%=========================================================%I
I=IB-P_IB*(IB-IA)/(P_IB-P_IA);
if abs((II-IB)/IB)<tol,
xS=II;,
break,
end,
%=========================================================%
%Step 6. If convergence is not satisfied, repeat Steps 2-5
%=========================================================%
IA=IB;
IB=II;,
end,
if k==imax, 'did not converge!!!!',
end
%=========================================================%
%Step 7. Evaluate fill-time
%=========================================================%
%The above iteration gives phi and dPda at the last node.
%=========================================================%t
_C=Lt^2*phi*visci/(2*K*(-dPda));
t_CV=(1/Bv)*log(1/(1+nu0*Bv*(Lt^2*phi/(2*K*(dPda)))));
%=========================================================%
%==========================END============================%
```

```
printf('**********FILL-TIME RESULTS**********\n')
printf('************************************************************\n')
printf('No     Type          Additional Infotmation             Fill-time(s)\n')
printf('1      t_UC         Uncoupled,Constant Viscosity         %9.0f\n',t_UC)
printf('2      t_UCV        Uncoupled,Time Dependt Viscosity      %9.0f\n',t_UCV)
printf('3      t_C          Coupled, Constant Viscosity          %9.0f\n',t_C)
printf('4      t_CV         Coupled, Time Dependant Viscosity     %9.0f\n',t_CV)
printf('************************************************************\n')
printf('************************************************************\n')
```

APPENDIX B – THERMAL BOUNDARY CONDITIONS OF VALIDATION SIMULATIONS

In the validation simulations, air temperature is measured as 17˚C and the average surface temperature is assumed as 35 ˚C. Properties of air at 12˚C as below.

Table 23.Air thermophysical properties of air at 17˚C

Property (at 17˚C)	Value	Reference
Density	$1.208\ kg/m^3$	[55]
Viscosity	$179.6\ x10^{-7}\ N.s/m^2$	[55]
Thermal conductivity	$0.025\ W/mK$	[55]
Thermal Expansion	$21.8\ x10^{-6}\ m^2/s$	[55]
Volumetric Thermal Expansion	$0.0033\ K^{-1}$	[55]
Prandtl Number	0.7096	[55]

Nusselt number associated with the geometry described in Figure 97 is as below.

$$\overline{Nu_{L}}_{bottom} = 0.52\ {R_{a_L}}^{1/5} \quad (\ 10^4 \lesssim R_{a_L} \leqq 10^9, Pr \gtrsim 0.7\ ) \tag{130}$$

Need to check the validity of Equation (130) by calculating the Rayleigh Number.

$$R_{a_L} = \frac{\rho g \beta (T_s - T_{air}) L^3}{\mu \kappa} = 2.44\ x\ 10^6 \text{ (Assumption is valid)} \tag{134}$$

The associated average convective heat transfer coefficient is evaluated as follows.

$$\bar{h}_{bottom} = \frac{\lambda_{air}}{L}\ \overline{Nu_{L}}_{bottom} = 2.28\ W/m^2K \tag{135}$$

APPENDIX C – ENERGY CONSUMPTION DATA OF PROCESSES

Table 24 .Energy Consumption Data of Co-curing Manufacturing

Co-curing Manufacturing	Energy Consumption									
	Convection Oven			Vacuum Pump			Vacuum Pump			Total
Operation	E. Intensity	Hour	Consumption	E. Intensity	Hour	Consumption	E. Intensity	Hour	Consumption	
Preform Preparation	3156 kJ/h	0.0h	0 kJ	300W	0.0h	0 kJ	1000 W	0.0h	0 kJ	0 kJ
Foam Mold Preparation	3156 kJ/h	16.0h	50496 kJ	300W	0.0h	0 kJ	1000 W	0.25h	900 kJ	51396 kJ
VARTM Process	3156 kJ/h	0.0h	0 kJ	300W	1.0h	1080 kJ	1000 W	0.0h	0 kJ	1080 kJ
Curing	3156 kJ/h	8.0h	25248 kJ	300W	0.0h	0 kJ	1000 W	0.0h	0 kJ	25248 kJ
								Total Energy Consumption		**77724 kJ**

Table 25.Energy Consumption Data of Secondary-Bonded Manufacturing

Co-curing Manufacturing	Energy Consumption									
	Convection Oven			Vacuum Pump			Vacuum Pump			Total
Operation	E. Intensity	Hour	Consumption	E. Intensity	Hour	Consumption	E. Intensity	Hour	Consumption	
Preform Preparation	3156 kJ/h	0.0h	0 kJ	300W	0.0h	0 kJ	1000 W	0.0h	0 kJ	0 kJ
Top Skin VARTM Process	3156 kJ/h	0.0h	0 kJ	300W	0.5h	540 kJ	1000 W	0.0h	0 kJ	540 kJ
Curing	3156 kJ/h	8.0h	25248 kJ	300W	0.0h	0 kJ	1000 W	0.0h	0 kJ	25248 kJ
Bottom Skin VARTM Process	3156 kJ/h	0.0h	0 kJ	300W	0.5h	540 kJ	1000 W	0.0h	0 kJ	540 kJ

Table 25 (cont'd). Energy Consumption Data of Secondary-Bonded Manufacturing

Co-curing Manufacturing	Energy Consumption									
	Convection Oven			Vacuum Pump			Vacuum Pump			Total
Operation	E. Intensity	Hour	Consumption	E. Intensity	Hour	Consumption	E. Intensity	Hour	Consumption	
Curing	3156 kJ/h	8.0h	25248 kJ	300W	0.0h	0 kJ	1000 W	0.0h	0 kJ	25248 kJ
Web VARTM Process	3156 kJ/h	0.0h	0 kJ	300W	0.5h	540 kJ	1000 W	0.0h	0 kJ	540 kJ
Curing	3156 kJ/h	8.0h	25248 kJ	300W	0.0h	0 kJ	1000 W	0.0h	0 kJ	25248 kJ
Side Web VARTM Process	3156 kJ/h	0.0h	0 kJ	300W	0.5h	540 kJ	1000 W	0.0h	0 kJ	540 kJ
Curing	3156 kJ/h	8.0h	25248 kJ	300W	0.0h	0 kJ	1000 W	0.0h	0 kJ	25248 kJ

Table 25 (cont'd). Energy Consumption Data of Secondary-Bonded Manufacturing

Co-curing Manufacturing	Energy Consumption									
	Convection Oven			Vacuum Pump			Vacuum Pump			Total
Operation	E. Intensity	Hour	Consumption	E. Intensity	Hour	Consumption	E. Intensity	Hour	Consumption	
Panel Cutting	3156 kJ/h	0.0h	0 kJ	300W	0.0h	0 kJ	1000 W	0.25h	900 kJ	900 kJ
First Bonding Operation	3156 kJ/h	8.0h	25248 kJ	300W	0.0h	0 kJ	1000 W	0.0h	0 kJ	25248 kJ
Second Bonding Operation	3156 kJ/h	8.0h	25248 kJ	300W	0.0h	0 kJ	1000 W	0.0h	0 kJ	25248 kJ
Third Bonding Operation	3156 kJ/h	8.0h	25248 kJ	300W	0.0h	0 kJ	1000 W	0.0h	0 kJ	25248 kJ
								Total Energy Consumption		**179796 kJ**

APPENDIX D – LABOR TIME OF PROCESSES

Table 26. Total Labor Time of Co-curing Manufacturing

Co-curing Manufacturing	
Operation	Labor Time
Preform Preparation	1.00h
Foam Mold Preparation	1.00h
VARTM Process	2.50h
Curing	0.00h
Total Labor Time	**4.50h**

Table 27. Total Labor Time of Secondary-bonding Manufacturing

Secondary-bonding Manufacturing	
Operation	Labor Time
Preform Preparation	1.00h
Top Skin VARTM Process	1.00h
Curing	0.00h
Bottom Skin VARTM Process	1.00h
Curing	0.00h
Web VARTM Process	1.00h
Curing	0.00h
Side Web VARTM Process	1.00h
Curing	0.00h
Panel Cutting	0.25h
First Bonding Operation	0.25h
Second Bonding Operation	0.25h
Third Bonding Operation	0.25h
Total Labor Time	**6.00h**